

Emil Krokan

Loess granulometry assesement of a Scandinavian blockfield

Master's thesis in Geography

Supervisor: Irina Rogozhina

December 2020

NTNU
Norwegian University of Science and Technology
Faculty of Social and Educational Sciences
Department of Geography



Emil Krokan

Loess granulometry assesement of a Scandinavian blockfield



Master's thesis in Geography
Supervisor: Irina Rogozhina
December 2020

Norwegian University of Science and Technology
Faculty of Social and Educational Sciences
Department of Geography



Norwegian University of
Science and Technology

Abstract

Blockfields in southern Norway are a highly debated topic concerning if they were glaciated or protruded as nunataks during the last glaciation. Loess deposits may provide valuable information concerning paleoclimatic conditions, and the extent and timing of glaciations.

The autochthonous blockfield situated on the summit of Tron gabbro massif, south-east central Norway makes the case for this study. Two excavated pits resulted in eight sampled horizons of columns reaching 1m depth. The loess-sized fractions (2-63 μm) were analyzed with the Scanning Electron Microscope (SEM) based Automated Mineralogy System (AMS). The two analysis modes *Spot Centroid* and *mineral mapping* were utilized in a comparable approach and mutual validation of the results. The granulometry and mineralogy were examined in order to investigate if this approach is sufficient to distinguish loess from in-situ weathered silt. The mineralogy implies that considerably amounts of quartz silt are present in the sediment composition, and the particle morphology is majorly bulky and angular to subangular. Both the mineralogy and grain morphology have similar features as the loess particles on the Loess Plateau in China, but the method is not substantial enough to separate aeolian from in-situ weathered silt.

Sammendrag

Blokkmarka i Sør-Norge er et omdiskutert tema i den grad de var under isdekket eller var plassert på nunataker i løpet av den siste istid. Løss-avsetninger kan tilby verdifull informasjon angående paleoklimatiske forhold, samt utbredelsen og tidspunkt for istider.

Den autoktone blokkmarka lokalisert på plataet av gabbrofjellet Tron, sør-øst sentrale Norge utgjør grunnlaget for denne studien. To utgravde groper resulterte i åtte innsamlede horisonter av kolonner som strekker seg ned til en dybde på 1m. Løss-fraksjonene (2-63 μm) ble analysert med det sveipeelektronmikroskop (SEM) baserte automatisk mineralogi system (AMS). Analysemodusene *Spot Centroid* og *mineral mapping* ble benyttet som en sammenlignbar tilnærming og gjensidig validering av resultatene. Granulometrien og mineralogien ble eksaminert for å undersøke om denne tilnærmingen er tilstrekkelig til å skille løss fra ikke-løss. Mineralogien impliserer at det er betydelige mengder av kvarts silt tilstede i sedimentene, og at kornformene i hovedsak er klumpete og kantete til mindre kantete. Både mineralogien og kornmorfologien har likhetstrekk med løss-partikler på Loess Plateau i Kina, men metoden er ikke tilstrekkelig i seg selv til å skille vindblåst silt fra in situ-forvitret silt.

Preface

Tusen hjertelig takk til min veileder Irina Rogozhina og delveileder Maria Peter for enestående oppfølging og tålmodighet.

En stor og ydmyk takk til Ola Fredin og NGU for finansieringen av analysene. Ben Snook skal også ha en stor takk for utførelsen av analysene, og for å være tilgjengelig for mine spørsmål vedrørende det tekniske. Det samme gjelder Kurt Aasly.

Marte og Quyen-Dao fortjener stor honnør for å stille opp som feltassistenter. Ellers må også Jacob og Martin rettes oppmerksomhet for utmerket selskap under skrivingen pre-Covid, og Anders for sin tilstedeværelse også etter at universitetet åpnet opp igjen. Ellers må samtlige andre som har vært tilstede på GEOLF-Kontoret takkes for heidundrende runder med kortspill og diverse sjakk-parti.

Table of contents

Abstract.....	II
Sammendrag.....	III
Preface.....	IV
Table of contents	V
List of figures.....	VIII
List of tables.....	IX
Abbreviations.....	X
1 Introduction	1
1.1 Motivation.....	1
1.2 Research questions.....	3
1.3 Research objectives.....	3
1.4 Study site: Tron.....	3
1.4.1 Geomorphology	4
1.4.2 Bedrock geology	5
1.4.3 Deglaciation	7
1.4.4 Climate.....	7
1.4.5 Ground thermal regime	9
2 Theory.....	11
2.1 Ground thermal regime	11
2.1.1 Permafrost	11
2.1.2 Controlling factors	12
2.1.3 Subsurface thermal regime.....	13
2.2 Cryoturbation.....	14
2.2.1 Frost sorting processes.....	14
2.3 Weathering characteristics	15
2.3.1 Chemical weathering.....	15
2.3.2 Mechanical weathering	16
2.3.3 Biotic weathering.....	18
2.3.4 Controlling factors on weathering.....	18
2.3.5 Clay mineralogy.....	19
2.4 Blockfields	20
2.5 Origin and development.....	20
2.5.1 The Neogene hypothesis	21
2.5.2 The periglacial hypothesis	21

2.6	Tors and surface lowering.....	22
2.7	Grain size and morphology	23
2.8	Loess	24
2.8.1	Quaternary dust transport.....	25
3	Methods.....	27
3.1	Sediment sampling of pits.....	27
3.2	Laboratory techniques.....	29
3.2.1	Grain-size analysis of coarse fractions.....	29
3.2.2	Grain morphology and mineralogy characterization of coarse fraction.....	29
3.3	Automated mineralogy analysis.....	30
3.3.1	Overview.....	30
3.3.2	Procedure	32
4	Results.....	34
4.1	General description of the pits	35
4.1.1	TrP1.....	35
4.1.2	TrP2.....	36
4.2	Classification and description of grain morphologies of the coarse fraction.....	37
4.3	Grain size distribution coarse fractions.....	39
4.4	Grain size distribution and mineralogy of fine fractions	40
4.4.1	Comparison of mineral distribution in TrP1 by Spot Centroid and mineral mapping ..	46
4.5	Grain morphology of fine fractions	47
4.5.1	Comparison of compactness measurements between both analyses within TrP1.....	49
4.5.2	Comparison of Spot Centroid compactness measurements between TrP1 and TrP2 ...	49
4.5.3	Grain morphology of quartz and plagioclase	50
4.5.4	Comparison of quartz and plagioclase compactness.....	52
4.5.5	SEM	52
5	Discussion.....	54
5.1	Grain morphology and size of the loess-sized particles.....	54
5.2	Mineralogy of the loess-sized particles.....	57
5.2.1	Potential time of deposition	58
5.2.2	Comparison of Spot Centroid and mineral mapping-analyses.....	59
5.2.3	Potential error sources through SEM method/preparations	59
5.3	Origin of clasts and the loess-sized fractions.....	59
5.4	Further research	61
6	Conclusion.....	62
7	List of references.....	64

8 Appendix 76

List of figures

Figure 1.1 Location of Tron marked in red	4
Figure 1.2 Superficial deposits on Tron (NGU, 2019).....	4
Figure 1.3 BEDROCK GEOLOGY SUMMARIZING TRON MASSIF (RAMSEY AND SIEDLECKA, 2001).....	6
Figure 1.4 a) Yearly precipitation, and (B) Yearly temperature, southern Norway 1957-2020. Location of Tron marked in red (SeNorge.no, 2020).....	8
Figure 1.5 Ground surface temperatures Tro-BH1 (B. Etzelmüller, personal communication, 28. January 2020).....	9
Figure 1.6 Uppermost six temperature loggers in Tro-Bh1 (B. Etzelmüller, personal communication, 28. January 2020).....	11
Figure 2.1 Simulated dust deposition ($\text{g m}^{-2} \text{yr}^{-1}$) during Last Glacier Maximum (Mahowald et al., 1999).	26
Figure 2.2 DIFFERENT MODES OF AEOLIAN TRANSPORT (PYE, 2015).	26
Figure 3.1 Surface cover of TrP1.	28
Figure 3.2 Surface cover of TrP2 pre-excavation. Plot marked by digging bar.....	28
Figure 3.3 ILLUSTRATION OF PARTICLE SHAPE CLASSIFICATION (POWERS, 1953).....	29
Figure 3.4 Visualization of long(L), intermediate (I), and short(S)-axis (Blott and Pye, 2008).....	30
Figure 3.5 Overview of the technology (Zeiss, 2020).....	31
Figure 3.6 VISUALIZATION OF THE STEPWISE PROCEDURE (ROLLINSON, 2019).....	32
Figure 4.1 Visualization of TrP1 (S1-S4) and TrP2 (S5-S8) columns with depth labels attached.	35
Figure 4.2 Distribution (%) of the sediment composition in TrP1	36
Figure 4.3 Distribution (%) of sediment composition in pit2.....	37
Figure 4.4 Visual survey of gravel extracted from TrP1.....	38
Figure 4.5 Visual survey of gravel and very small boulders in TrP2.....	38
Figure 4.6 TrP1 grain-size distribution of coarse fractions.	39
Figure 4.7 TRP2 GRAIN-SIZE DISTRIBUTION OF COARSE FRACTIONS	40
Figure 4.8 Average grain size (μm) comparison of measurements by Spot Centroid (SC) and mineral mapping (MM) in TrP1.	43
Figure 4.9 Mineral distribution by Spot Centroid in TrP1.	45
Figure 4.10 Mineral distribution by mineral mapping in TrP1.....	46
Figure 4.11 Distribution of the total particle compactness obtained from both analyses in TrP1 and from the SC-analysis for TrP2.....	48
Figure 4.12 Distribution of quartz compactness in TrP1 obtained from Spot Centroid (SC) and mineral mapping (MM).	50
Figure 4.13 Distribution of plagioclase compactness obtained from both analyses.....	51
Figure 4.14 False-color image and backscattered electron image (BSE) at 20-30 cm depth (S1) in TrP1. The squares encapsulate examples of blocky quartz, and the circles show muscovite. Full images of each depth can be found in the appendix.	52
Figure 4.15 False-color image and backscattered electron image (BSE) at 80-90 cm depth (S4) in TrP1. The squares encapsulate examples of blocky quartz, and the circles show muscovite.	53
Figure 5.1 Sem micrograph of loess in China (Liu et al., 2016).....	54
Figure 5.2 Magnified backscattered-electron image (BSE) of squares containing quartz (Q) in fig. 4.14 and fig. 4.15. S1 (20-30cm) and S4 (80-90 cm)	55
Figure 5.3 Magnified backscattered-electron image (BSE) of the muscovite presented in Fig. 4.13 and 4.14. S1 (20-30 cm) and S4 (80-90 cm).	56

List of tables

Table 3.1 Analytical conditions for mineral mapping and Spot Centroid-analysis	33
Table 4.1 Classification of gravel sizes and shape (%)	37
Table 4.2 Compilation of Bulk data in TrP1 obtained by mineral mapping.	41
Table 4.3 Compilation of bulk data in TrP1 by Spot Centroid.....	42
Table 4.4 Grain-size distribution based on feret max diameter obtained from mineral mapping- analysis in TrP1 and Spot Centroid in TrP1 and TrP2.....	44
Table 4.5 Grain-size distribution of quartz based on feret max diameter obtained from both analyses in TrP1.	44
Table 4.6 Compactness (%) measurements obtained from mineral mapping-analysis in TrP1 and Spot Centroid in TrP1 and TrP2.....	47
Table 4.7 Compactness (%) of quartz in TrP1 obtained from both analyses.....	50
Table 4.8 Compactness (%) of plagioclase in TrP1 obtained from both analyses.	51

Abbreviations

SEM-EDS-AM – Scanning electron microscopy – Energy dispersive spectrometry – automated mineralogy

^{10}Be – Cosmogenic nuclide dating

TCN – Terrestrial cosmogenic nuclide

$\delta^{18}\text{O}$ – Measure of stable isotope oxygen-18 ratios

SEM – Scanning electron microscope

AMS – Automated mineralogy system

1 Introduction

1.1 Motivation

Blockfields have during history acquired various names, such as felsenmeer, blockmeer, boulder fields, stone fields and mountain top-detritus, and are a widespread landform occurring on every continent (Rea et al., 1996; Dredge, 2000). In Scandinavia blockfields commonly occur on plateaus (Ballantyne, 2010). The age and origin of blockfields have been the subject to a lot of controversy resulting in a diversity of scientific research. The most profound hypotheses represented in the literature comprises of origin in either Pre-Pleistocene (Roaldset, 1982; Follestad, 1990; Rea et al., 1996; Whalley et al., 1997; Whalley et al., 2004; Fjellanger et al., 2006; Linge et al., 2006; Paasche et al., 2006; Phillips et al., 2006; Strømsøe and Paasche, 2011) or during Quaternary (Goodfellow et al., 2008; Goodfellow et al., 2014; Hopkinson and Ballantyne, 2014). The hypotheses are in large concerned by the weathering mechanisms involved in the formation (Ballantyne, 2017), and if the landform was preserved beneath cold-based glaciers (Nesje et al., 1988; Follestad, 1990; Nesje and Dahl, 1990; Rea et al., 1997; Dredge, 2000; Hättestrand and Stroeven, 2002; Fjellanger et al., 2006; Linge et al., 2006; Darmody et al., 2008; Goehring et al., 2008; Fabel et al., 2012; Marr et al., 2018), or were located on nunataks (Nesje et al., 1988; Follestad 1990; (Marr and Löffler, 2017; Marr et al., 2018).

If loess is to be distinguished from in-situ weathered silt it could provide information about the Tron summit being ice-free for longer periods during the last glacial. Investigation into aeolian silt deposits may provide valuable information of climate change during Quaternary and timing of glaciations (Pye, 1995; Frechen et al., 2003). In Pleistocene periglacial environments, wind action was a major contributor in modification of the high northern latitudes (French, 2007). Aeolian transport and deposition of silt in Europe became enhanced due to less rainfall, low abundance of vegetation, strong winds, frost shattering and glacial abrasion during glacial episodes (Bertran et al., 2016). Deposits of Aeolian silt with cold-climate origin have been reported Alaska, central Siberia and Tibet. Holocene aeolian silt deposits are found on upland surfaces in Arctic North America (French, 2007). In Europe, loess stems from the Quaternary glacial period and has a widespread distribution across Central Europe (Haase et al., 2007; Muhs, 2013), but is yet to be reported in Scandinavia (Muhs, 2013).

Weathering, erosion and transport processes leave distinct signatures on sedimentary particles, providing the opportunity to reconstruct their origin (Benn, 2007).

The Tron massif has been the focus of research in regard to its summit blockfield cover in a number of studies. Strømsøe and Paasche (2011) investigated weathering patterns by bulk composition analysis of regolith and bedrock. Nesje et al. (1994) measured rock surface weathering by Schmidt hammer and profile gauge. Geophysical methods by Engelién (1994). Halleraker (2011) investigated the physical properties of weathered rock by application of X-ray diffraction (XRD), X-ray fluorescence (XRF), scanning electron microscope (SEM) and grain-size distribution (GSD). Halleraker found (i) chemical weathering to be the dominant process, while frost weathering is limited at present, (ii) prolonged weathering, (iii) preservation of the blockfield cover by cold-based ice.

The study area for this thesis is the isolated gabbro massif Tron, located in Alvdal municipality, Innlandet (formerly known as Hedmark). With a week apart, two full days of field work were carried out in late September 2019, resulting in two excavated pits and subsequently 4 horizontal transects were sampled from each pit, respectively. The samples were prepared in correlation to standard practices (graphite mixed into samples to produce polished blocks) and analyzed by the Scanning electron microscope (SEM) based automated mineralogy system (AMS). Two analysis modes were applied in order to correlate the results against each other as a form of validation. The aim shaping the thesis were based on obtaining grain-size distribution of each transect in order to compare the amount of fractions in the column and between both columns. The granulometry of the silt fractions are examined to explore if the blockfield summit has been subjected to aeolian silt transport. In order to contribute to the understanding of the processes operating in the subsurface of the Tron massif blockfield, this thesis will introduce an automated mineralogy-analysis as a new approach to extract information in this regard. The capabilities of the Automated Mineralogy System provide accurate identification and quantification of mineral types, mineral abundance, grain-size and morphology. Establishing the distribution of coarse and fine fractions in the uppermost 90 cm could give insight into the vertical mixing of sediments have occurred during time due to processes related to frost heave. Available mineralogic research completed on the Tron massif provides the opportunity to make comparisons with findings during this work.

1.2 Research questions

- Can aeolian silt be identified and distinguished from non-aeolian silt in the blockfield column on Tron summit?
- Does the content of aeolian silt vary over depth in the summit blockfield of Tron mountain?

1.3 Research objectives

In order to achieve knowledge that enables the possibility to provide answers to the research questions, the aim is to gain insights into the mechanisms responsible for forming the morphology of the silt-sized fractions. Identification of the minerals occurring in the pits could tell if they correlate with the lithology or have foreign origin.

- Investigate how the sediment composition and distribution have been modified by frost sorting processes.
- Quantification and identification of the mineralogy and particle morphology, in order to investigate if the blockfield sediments are composed of aeolian input.
- Compare the outcome of two Automated Mineralogy system analysis modes on the samples in order to isolate the most precise method.
- Obtain the grain size distribution for the fine fraction through the scanning electron microscope (SEM).
- Set up and compare the results against former research on the summit.
- Investigation of silt-sized fractions in order to identify formation exclusively in-situ or if Pleistocene aeolian sediment transport have contributed to the sediment composition.

1.4 Study site: Tron

The subject for this study is the Tron summit blockfield (62°10' N 10°41' E). Tron is located in Alvdal municipality between the valleys Østerdalen and Tyllaldalen. The mountain consists of the two peaks Tron (1665 m.a.s.l) and Tylldalstoppen (1650 m.a.s.l). The plateau forms a depression between the two mountain peaks, which are covered with a bouldery surface.



FIGURE 1.1 LOCATION OF TRON MARKED IN RED

1.4.1 Geomorphology

The dominant superficial deposits at the summit consists mainly of weathered material (blockfields) and bedrock, while the lower altitudes are characterized by discontinuous moraines on the southern slopes, ablation till on the northern parts and sporadic avalanche deposits (Thoresen and Follestad, 1999).

A detailed mapping of glacial and periglacial landforms on the massif was done by Halleraker (2011), which includes:

Lateral meltwater channels were observed between 900-1400 m.a.s.l, with a slight inclination towards west.

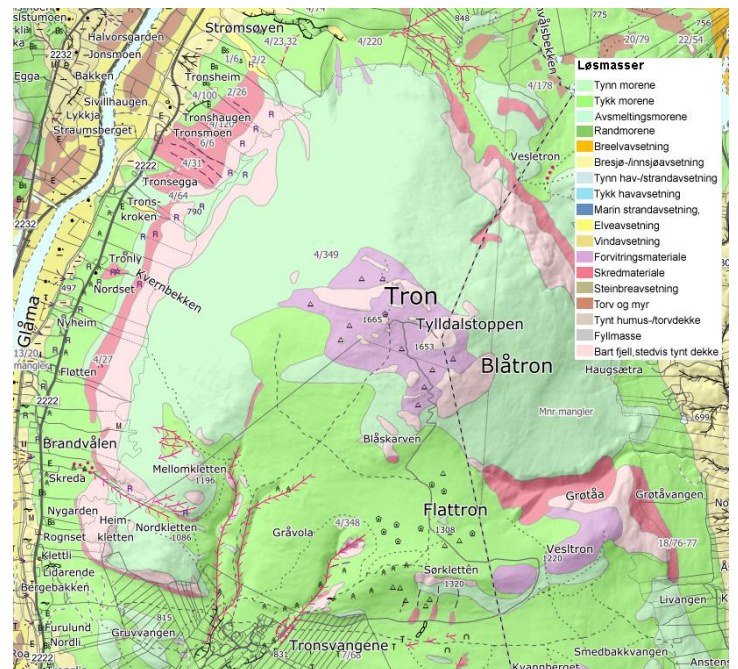


FIGURE 1.2 SUPERFICIAL DEPOSITS ON TRON (NGU, 2019).

Gills are eroded into the green schist and amphibolite on the south section, and the remaining gills are found in the gabbro and amphibolite on the upper part, and metasandstone and slate on the lowermost areas.

Erratics were identified due to the different mineralogy, and occur in various sizes all over the plateau. According to Hult (In Halleraker, 2011), diorite and tillite were identified and among them, with a suggested origin from Jutulhogget (a 2.4 km long canyon south-east from Tron).

Sorted stripes are mostly found on the northwestern and northeastern parts, with a more sporadic spread on the southside. Both *sorted circles* and *unsorted circles* occur on top of the plateau.

Solifluction lobes occur widely around the massif, with highest occurrence on the northern slope.

1.4.2 Bedrock geology

The formation of the bedrock constituting Tron is of a Mesoproterozoic to Early Palaeozoic age (1600-450 Ma), and consists of metamorphosed sedimentary and volcanic rocks intruded by plutonic rocks. The Caledonian mountain chain stretching through entire Norway lengthwise, from northeast to southwest, includes Tron massif. The rocks origin belongs to a location a fair distance away, resulting from sheets thrust on top of each other during Palaeozoic. The massif consists mainly of coarse-grained olivine gabbro, with the originally magmatic layers preserved in the central zone. The lower parts (<1200 m.a.s.l) on the W—NW, consist of altered gabbro. The southern part consists of greenschist, greenstone, sulfide and tuffs. The lowest parts surrounding the massif are a mixture of quartzite, graphitic schist, garnet schist, calcite-chlorite-mica schist and garbenschist (Ramsey and Siedlecka, 2001).

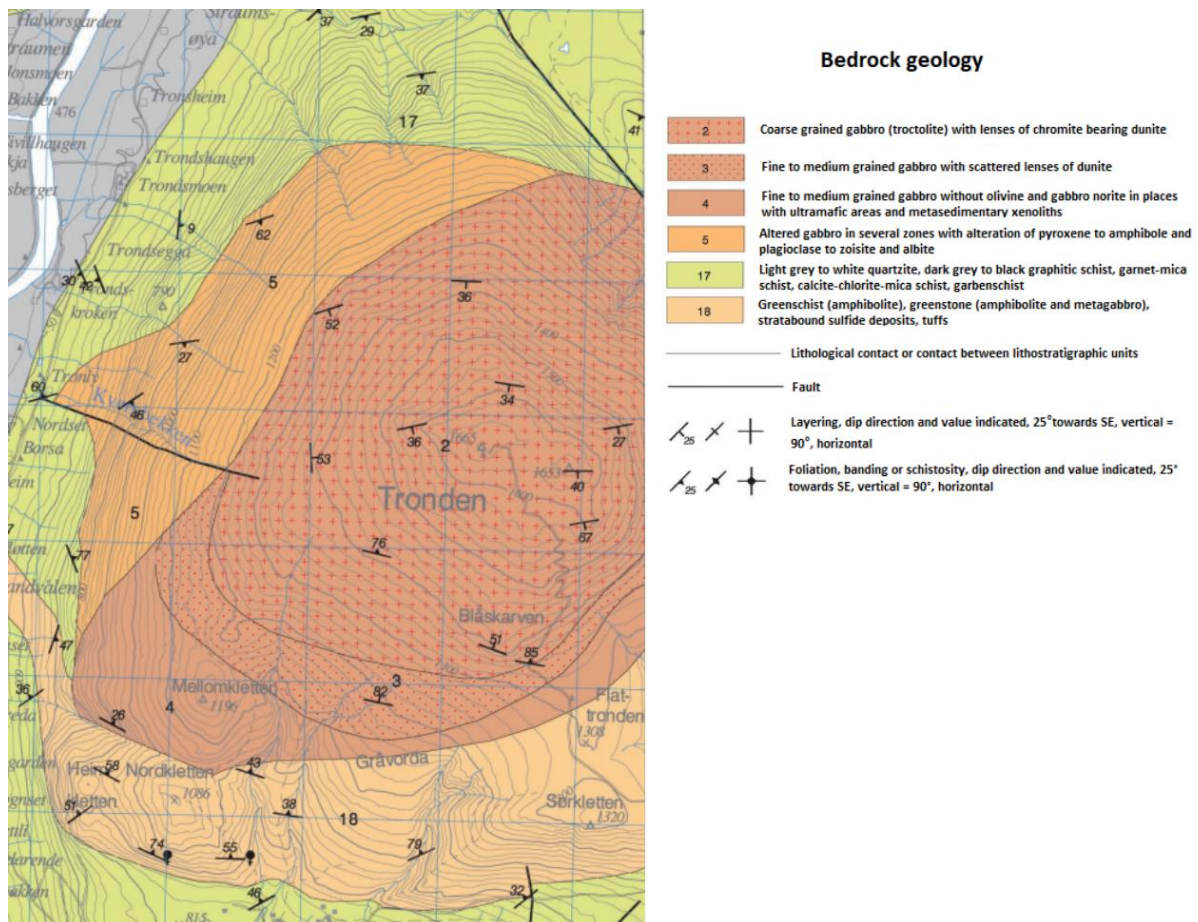


FIGURE 1.3 BEDROCK GEOLOGY SUMMARIZING TRON MASSIF (RAMSEY AND SIEDLECKA, 2001).

Wellings (1996) mapped the geology of the massif by collecting samples from 36 locations. Four of the locations are on the summit, close to the sampling sites in this thesis, and are presented her. Gabbro containing plagioclase, orthopyroxene, clinopyroxene and olivine were reported west on the summit. To the north-east of the summit, gabbro containing amphibole and plagioclase, and dunite/serpentine containing olivine, serpentine, white mica and amphibole were found. Altered gabbro containing clinopyroxene, amphibole and plagioclase were identified south-east on the summit.

1.4.3 Deglaciation

In the last interglacial, Eemian (130 000-115 000 ka), the climate was in general warmer than the present interglacial (Holocene) (Olsen et al., 2013). In early Weichselian (117-74 ka), Tron was ice-free during the Brørup interstadial (105-93 ka) and Odderade interstadial (85-74 ka), while being glaciated during Middle Weichselian and the Late Weichselian, before deglaciation during the end of Younger Dryas (Mangerud, 2004).

Biostratigraphy dating from Flåfattjønn (1110 m.a.s.l), Tynset, just north-east of Tron, show characteristics indicating deglaciation of the lake around 16 000 ka BP, meaning that the ice-sheet did not exceed 1110 m.a.s.l during Younger Dryas (Paus et al., 2006). During the last deglaciation remnants of the ice-sheet caused the ice-dammed lake Nedre Glåmsjø. Research into the related landforms (ex. De Geer moraines, beach ridges and shorelines) originating from Nedre Glåmsjø, has shown a southward retreat of the ice sheet rather than a mainly vertical melting. The rate of the retreat is estimated to be 600-200 meter per year in a period of 60-180 years. Radiocarbon dating of organic materials from the basin of the flooded areas suggests the outburst of the ice-dammed lake happened no later than 10-10,4 ka BP, indicating that the area became deglaciated around 11-10 ka BP (Berthling and Sollid, 1999; Høgaas and Longva, 2018). Reconstructions of the extent and retreat of the Scandinavian ice-sheet suggest that Tron became ice-free around 10,5-11 ka BP (Hughes et al., 2016; Olsen et al., 2013). Calculations of ^{10}Be concentrations in erratics implies that the vertical extent of the ice sheet reached 1460 m.a.s.l at Elgåhogna (71 km east of Tron) during LGM, and minimum 1620 m.a.s.l at Blåhø (80 km W-SW of Tron). The exposure ages indicate a gradually thinning of the ice sheet between $16,5 \pm 1,0$ and $11,7 \pm 1,0$ ^{10}Be ka, and more rapidly between $10,5 \pm 1,0$ and $11,7 \pm 1,0$ ^{10}Be ka at Elgåhogna (Goehring et al., 2008). Dahl et al. (1997) suggested that the altitude limit of the Late Weichselian ice sheet did not exceed 1600 m.a.s.l in east-central southern Norway after 22 ka, which would indicate that Tron summit was ice free during this period. Garnes and Bergersen (1980) proposed that the inland ice melted down almost continuously with no significant stagnation or oscillations after the highest mountains area became ice-free.

1.4.4 Climate

The mean annual air temperature on Tron between 1957-2019 was -3°C - -1°C (SeNorge.no, 2020). During 2008/09 the mean annual air temperature ranged from 3.6°C to -0.1°C , and -4.5°C to -2.3°C during 2009/10 (Farbrot et al., 2011). Tron is located within the subarctic climate group, according to the Köpper-Geiger climate classification, which extends as a belt

from the east coast of Russia, through Iceland and North-America. This group characterizes cold continental climates, with absence of a dry season, and experiencing cold summers (Kottek et al., 2006). Due to its geographical location in the east of southern Norway, the climate Tron is a part of characterizes as continental (Farbrot et al., 2011). Characteristics associated with continentality comprises high precipitation and dry soils due to evaporation during summer months (Ballantyne and Harris, 1994). Tron may be affected by Atlantic Ocean maritime air during advective weather conditions (Farbrot et al., 2011). Maritime climates are characterized by a narrower range in seasonal temperature variations than continental climates, and the influence of maritime air decreases progressively due to increased continentality (Ballantyne and Harris, 1994).

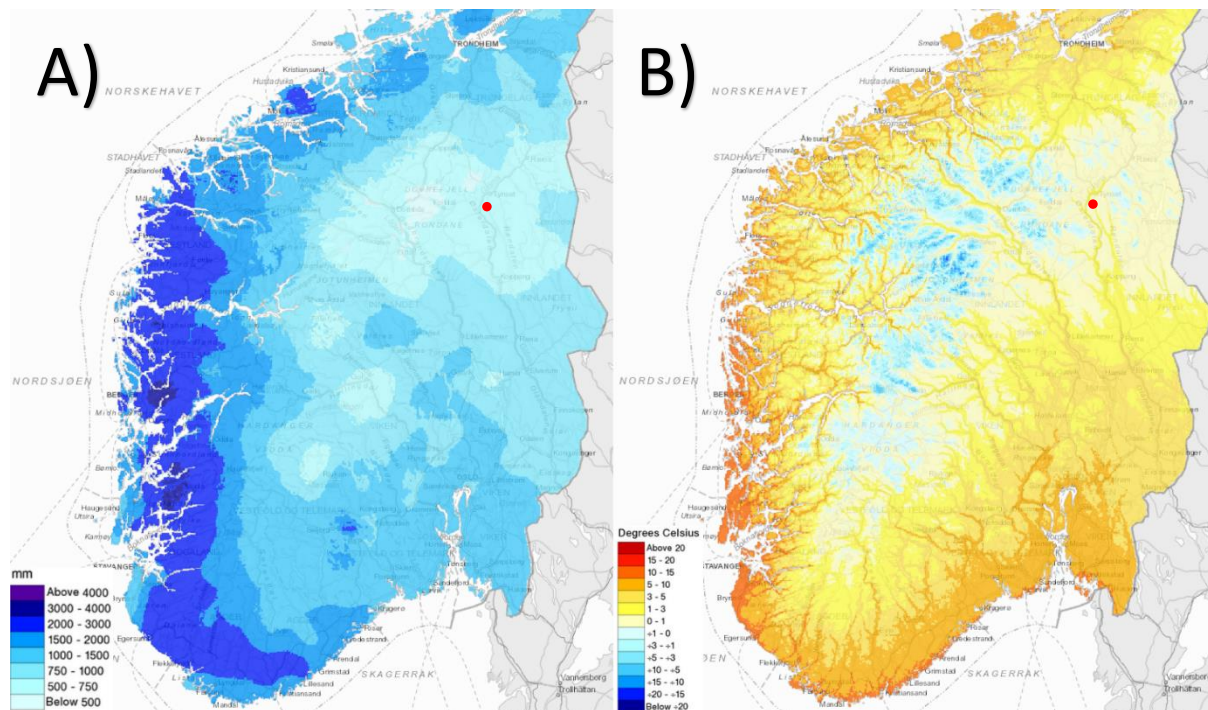


FIGURE 1.4 A) YEARLY PRECIPITATION, AND (B) YEARLY TEMPERATURE, SOUTHERN NORWAY 1957-2020. LOCATION OF TRON MARKED IN RED (SE NORGE.NO, 2020).

The snow cover on Tron were reported to be thin or absent due to exposure to wind erosion (Farbrot et al., 2011; Westermann et al., 2013). The maximum snow depth registered from Tron borehole-(BH1) reached approximately 90 cm between 2008-2010, and a snow depth duration of at least 5 cm were recorded for 247 days during 2008/09, and 249 days during 2009/10 (Farbrot et al., 2011). Snow depth measurements on Tron during two consecutive winters between 2018 to 2020 implies high variability of the snow cover on the blockfield. The snow depths measured from a total of 40 points on the plateau ranged from 0 cm to >350 cm (values exceeded the measurement scale), showing the snow to fill up immersions/depressions in the

blockfield. The north-east slope experienced a lee effect due to constantly strong winds (Peter et al., in prep).

Mean annual ground surface temperature (MAGST) recorded was 0.8°C in 2008/09 and -0.2°C in 2009/10. (Hipp et al., 2012). Fig. 1.5 shows ground surface temperatures constantly below 0°C during the winter months from 2015/2016 to 2018/2019. In the lower atmosphere temperatures may increase with height due to temperature inversions. Such phenomena may influence ground surface temperature, permafrost thickness and distribution, in areas with high relief (Taylor et al., 1998). Temperature inversions were reported to be prominent during winter (Farbrot et al., 2011).

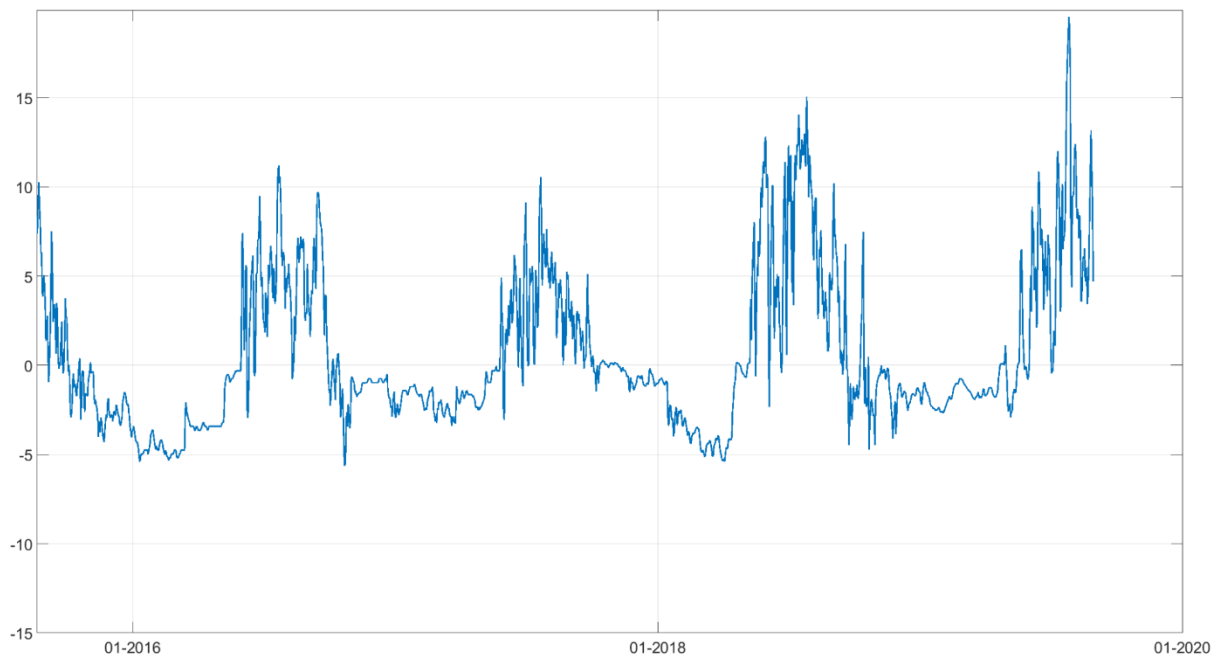


FIGURE 1.5 GROUND SURFACE TEMPERATURES TRO-BH1 (B. ETZELMÜLLER, PERSONAL COMMUNICATION, 28. JANUARY 2020).

1.4.5 Ground thermal regime

During the last 20-30 years the permafrost in Arctic lowlands has been subject to increased temperatures (Isaksen et al., 2011). The lower limit of permafrost decreases from above 1600 m a.s.l in Western Norway to below 1300 m a.s.l in Eastern Norway, and increases again further east. According to this, eastern parts of Norway is thought to represent the lowermost limits of mountain permafrost in Southern Scandinavia (Heggem et al., 2005). Located far east, Tron

differs from other block field sites in regard to its continental climate (Hipp et al., 2012). Permafrost presence in Southern parts of Norway are reserved to mountain regions and high-altitude plateaus (Westermann et al., 2013). Engelen (1995) found permafrost to be sporadic spread above 1625 m.a.s.l. on Tron, and assumed occurrence of permafrost in lower altitudes on the northern slope. Hipp et al. (2011) reported permafrost conditions at Tron to be at 1640 m a.s.l, with temperatures down to 0°C and signs indicative of permafrost degradation. Two boreholes were drilled into the blockfields, and one in a fine-grained moraine, in 2008 equipped with temperature loggers for measurements of ground surface temperatures, air temperature and snow depth (Farbrot et al., 2011; Hipp et al., 2012) In the period between 2008-2010 permafrost was scarce in the uppermost borehole, and seasonal frost in a depth of 2-4 meter on the other boreholes (Farbrot et al., 2011).

Farbrot et al. (2011) observed conditions on the north slope to be more suitable for permafrost, based on ground temperature measurements indicating a negative anomaly. This may be explained by the steeper slopes and the generally greater pore volume in the blockfield. Permafrost thickness was modelled to be up to 90 m and active layer thickness in the range of 1,3 to 6 m. The altitudinal zone of the lower limit of permafrost was below 1300 m a.s.l. The model indicates a rapid warming of permafrost since 1990, with an increase in the active layer thickness of 9 meters. The ground temperatures at 10 m depth increased by about 0.1°C to 0.7°C since the 1860s, and 0.1°C to 0.4°C at 100 m depths (Hipp et al., 2012). Fig. 1.6 shows the six uppermost temperature loggers on Tron summit (Tro-BH1), where all show temperatures above 0°C in late summer 2019.

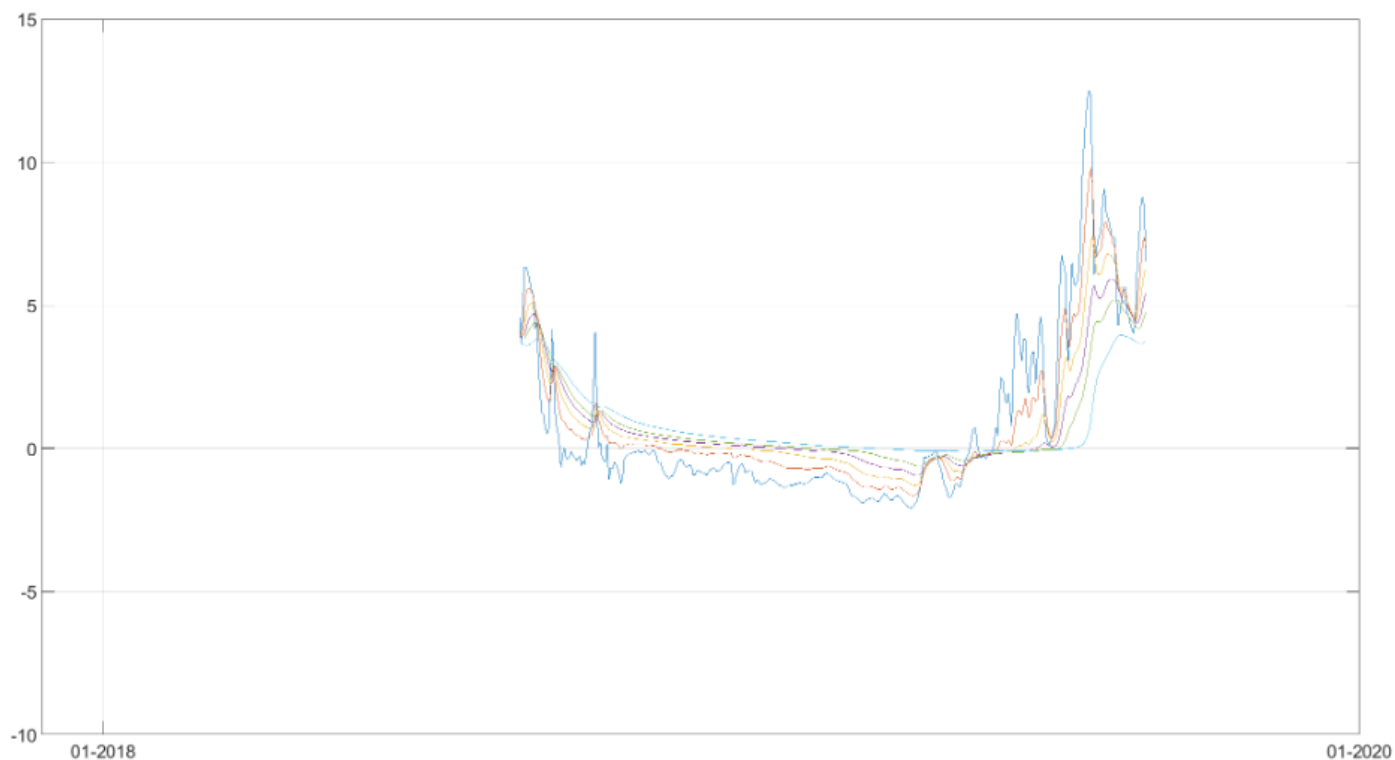


FIGURE 1.6 UPPERMOST SIX TEMPERATURE LOGGERS IN TRO-BH1 (B. ETZELMÜLLER, PERSONAL COMMUNICATION, 28. JANUARY 2020).

2 Theory

2.1 Ground thermal regime

2.1.1 Permafrost

Permafrost is a thermal condition used to describe soils, bedrock or sediment with temperatures below 0°C for minimum two consecutive years, without any dependency of ice or moisture content present (Ballantyne and Harris, 1994; Zhang et al., 2008). The present-day permafrost and ground ice distribution are a result of development during the glacial period and the ongoing heat exchange at the surface and within the ground (Zhang et al., 2008). Two concepts used to categorize between frozen and unfrozen ground, are respectively *cryotic*, ground temperatures below 0°C, and *noncryotic*, ground temperatures greater than 0°C. Permafrost thermal regime and thickness are the result of the governing factors, such as, mean annual air

temperature (MAAT), thermal conductivity of the ground and ground materials, and surface conditions (Ballantyne and Harris, 1994; Harris et al., 2009).

2.1.2 Controlling factors

Two conditions that mainly controls the thermal regime within permafrost are; atmospheric energy fluxes at the ground surface, and geothermal heat fluxes from the earth's interior (Williams and Smith, 1989).

The active layer, suited above the permafrost, is characterized by seasonally thawing and freezing, where migration of heat and water occurs. During winter freezeback, the hydrologic conductivity decreases as a result of pores filled with ice (Hinkel et al., 1996). Freeze and thaw of the active layer are largely governed by local lithology. Soils consisting of fine sands, silt and clay prevents porewater to freeze at 0°C, and requires temperatures to be slightly lower to allow freezing (Ballantyne and Harris, 1994). Within the active layer there is an interconnection between the thermal and moisture states (Boike et al., 1998).

In mountain environments, various factors, such as topography, surface cover, soil moisture and snow depth, affect the interaction between ground and air temperatures, and the following thermal regime (Harris et al., 2009; Isaksen et al., 2011). The factors determining permafrost presence relates to cold climate, snow (thickness/timing/duration), atmospheric conditions (wind/precipitation), vegetation, energy exchanges, heat transfer through the active layer and local factors connected to geology and hydrology (Etzelmüller et al., 2001). The two most important factors controlling permafrost distribution are elevation and topography. In contrary to maritime areas, such as western Norway, where elevation is sufficient to explain permafrost distribution, the more continental areas, like central parts of Scandinavia, topography plays a large role. This distinction relies on the higher summer temperatures in continental areas, contributing to denser vegetation and organic material. Vegetation is important in continental environments and has the ability to damp summer temperatures. Presence of organic material, which in frozen condition has higher thermal conductivity than when thawed, allow winter air temperatures to more easily penetrate into the ground (Etzelmüller and Frauenfelder, 2009).

Thermal offset is influenced by soil moisture, and explains the lower mean annual temperature difference at the permafrost table compared to the ground surface. Due to winter freezing of the active layer the conductivity is higher than the summer thawed active layer (Harris et al., 2009). Ground temperature are strongly affected by thermal regime during winter, in regard to

the effectiveness snow has as an isolating effect causing thermal offset between air and ground temperatures, especially significant in northern regions (Park et al., 2015).

Four theories have been postulated to explain the factors controlling the thermal regime in blockfields, summed up by Harris and Pedersen (1998):

The Balch effect is based on the difference in air density, where cold air replaces the warmer air in cavities in-between coarse blocks.

The chimney effect takes thick snow cover into account, with presence of voids allowing warm air to escape and get replaced by colder air.

Summer evaporation/sublimation of water/ice in the blocky debris. Due to these processes blocks experience cooling through fluctuations of latent heat.

Continuous air exchange with the atmosphere is subject to blockfields with lack of a continuous snow cover preventing a continuous exchange of air between the soil and the atmosphere, causing instantaneous warming and cooling of the blocks.

Blocky materials have high porosity causing a special environment of heat conduct, resulting in colder regimes than fine-grained soils (Gorbunov et al., 2004). Blocks protruding into and through the snow cover enhances the thermal conductivity on blockfield sites (Juliussen and Humlum, 2008). The heat conductor ability in snow are low, making the ground surface protected from short-term variations in air temperatures. Timing of snowfall and its thickness are essential in regard to the ground thermal regime. A thin snow cover during autumn allows heat fluctuations from the ground, while a thick snow cover accumulated in early winter restrict ground cooling (Ishikawa, 2003). Due to the low thermal conductivity in a thick snow cover, the temperature is largely governed by the heat transfer from the surface beneath (Isaksen et al., 2002). Thermal conductivity is four times higher of ice than water, resulting in a seasonal thermal offset (Juliussen and Humlum, 2007).

2.1.3 Subsurface thermal regime

Ground temperatures are mainly controlled by the conductive heat transfer. In addition, areas containing seasonal frost and discontinuous permafrost may be affected by groundwater circulation. Thermal properties of the ground may vary due to the mineral composition, organic content, density, moisture content and temperature, which may vary from the different layers. (Williams and Smith, 1989). The thermal parameters that controls the ground thermal regime

of permafrost are thermal conductivity and volumetric heat capacity, which both depend on the density and water content of local materials (Hipp, 2012).

2.2 Cryoturbation

The term cryoturbation comprehends all soil movements engaged by frost processes, which include frost heave, thaw settlement, differential movements by temperature change-engaged expansion and contraction, and segregated ice growth and disappearance. Cryoturbation is distinguished from other soil movement processes by the necessity of changes in the water-ice phase. A process embraced by cryoturbation are migration and sorting of particles (French, 2007).

2.2.1 Frost sorting processes

Permafrost environments may experience two-sided freezing when the mean annual ground temperature is several degrees below 0°C, and if it exceeds -5°C the upward freezing surpasses the downward freezing (Mackay, 1984).

Two hypothesis explaining upward frost sorting of clasts and sediment movement in soils are the *frost-pull theory* and *frost-push theory*. During *frost-pull* clasts are lifted as a cause of ice lensing during downward freezing, leaving behind an ice-rich void that fills with surrounding sediments during thawing, preventing the clast to return to its original placement. *Frost-push* explains how a frost front during freezing penetrates through the clast with subsequently ice formation around and beneath pushed the clast upwards. When thawing occurs sediments will start to fill the void beneath the frozen clast, which cause a vary displacement (Mackay, 1984; Ballantyne and Harris, 1994). Fine-grained fractions migrate under a wider specter of freezing rates compared to coarse fractions, which inevitably leads to sorting of homogenous material (French, 2007).

Vertical and lateral frost sorting in the active layer above permafrost are no different to permafrost absent environments experiencing seasonally-frozen ground.

Repeated cycles of freezing and thawing of poorly-sorted sediment in moisture soils segregates fines and clasts, and downward freezing and thawing cause a migration of the fine fractions downwards, while coarse fractions are lifted upwards.

2.3 Weathering characteristics

Weathering processes are continuously operating shaping the surface, due to interactions between the hydro-, bio-, litho- and atmosphere (Anand and Paine, 2002). Through physical and chemical weathering bedrock may decompose resulting in weathered regolith.

2.3.1 Chemical weathering

Chemical weathering comprises the chemical and mineralogical transformation of primary rocks and minerals at/or near the surface into products closer to equilibrium with Earth surface conditions (Dixon and Thorn, 2005).

When chemical weathering occurs on quartz, feldspar and olivine, the minerals become decomposed due to lattice breakdown. Crystal lattice describes the unique crystal structure minerals are composed of. Breakdown of lattice chemical bonds leads to formation of new chemical bonds, which is the result of the contact between minerals and rainwater percolation, soil and groundwater, and organic acids (Ballantyne, 2018).

The chemical reactions causing breakdown of crystal lattice are not fully understood, but the dominant reactions include solution, hydrolysis, carbonation, chelation, oxidation and reduction, which result in production of clay minerals or dissolved products (Ballantyne, 2018; Dixon and Thorn, 2005).

Solution is commonly the first phase of chemical weathering involving dissolving of minerals by water (Ollier, 1984), and occurs in all environments where moisture is present (Dixon and Thorn, 2005). Through contact with precipitation solution of calcite, dolomite, gypsum, halite and quartz occurs, due to dissolving of chemical bonds (Boggs, 2006).

Oxidation is the reaction occurring when minerals are in contact with atmospheric oxygen, or hydroxides if water is involved.

Reduction is the opposite of oxidation and involves oxygen ion removal from minerals.

Hydrolysis explains the chemical reaction resulting in breakdown of silicate minerals through interaction with acid. Minerals experiencing incomplete dissolution, incongruent dissolution, may produce kaolinite, illite and smectite if aluminum is present.

Carbonation occurs as a reaction between carbonate or bicarbonate ions with minerals.

Hydration is the addition of water to a mineral and is considered to be a very important process in the formation of clay minerals.

Chelation have the abilities to increase the mobility of mineral constituents, such as silica, iron and aluminum. It occurs as a result of bonding between mineral cation and organic acid.

Silicate minerals includes quartz, feldspar, mica, amphibole, pyroxene, olivine and various clay minerals. Chemical weathering of silicate minerals results from the thermodynamic conditions at the time of formation and the local conditions at the surface (White and Brantley, 1995).

Traces of chemical weathering processes involves the presence of secondary minerals, etched grain surfaces and the quantity of clay minerals (Goodfellow et al., 2008). According to findings by Strømsøe and Paasche (2011) clay and silt is mainly produced by chemical weathering, and particles larger than silt are caused by physical weathering. Grains smaller than 32 µm are probably products dominated by chemical weathering.

Areas subjected to at least seasonally periglacial processes, chemical weathering may be identified by low clay/silt ratios. The range of secondary minerals may be an indicator of the climate which the blockfields were formed (Goodfellow, 2012).

2.3.2 Mechanical weathering

In periglacial and permafrost environments frost weathering and changes in liquid water content and temperature are the causes behind mechanical weathering (Murton et al., 2007).

Frost weathering is a widespread process operating from the arctic to the high tropical mountains. This geomorphic process involves freeze and thaw of rocks and minerals containing water, and are divided into *volumetric expansion* and *ice segregation*. Volumetric expansion involves the nine percent expansion liquid water experience when freezing to ice. There are two scenarios which volumetric expansion fractures rock. First, rapid freezing of water-filled cracks and/or pores may lead to detachment of minerals and rock flakes. Secondly, hydrofracture caused by pore-water expulsion in saturated rocks consisting of coupled pores may lead to fractures. Volumetric expansion is thought to be the process which explains that due to multiple freeze-thaw cycles quartz sand breaks more easily than feldspar, and produces particles in the 5-10 µm range (Matsuoka and Murton, 2008). For ice segregation to occur, the need of thermally or gravitationally migrating water through porous soils are fundamental. In continuous permafrost environments the active layer is subject to two-sided freezing, and the upward freezing enhances migration of liquid water into the base of the active layer and the permafrost where segregated ice may form. Ice segregation may also form in areas where

permafrost is absent, but are seasonally frozen. This is proposed to be an important factor for bedrock fracturing (Murton et al., 2000; Murton et al., 2006; Murton, 2007; Matsuoka and Murton, 2008).

Frost shattering is thought to be unable to effectively break down rock without a symbiotic interaction with chemical processes (Whalley et al., 2004). Chemical weathering enhances disaggregation of rocks, while physical weathering enhances chemical dissolution by increased water access (White and Brantley, 1995). For either process to function, the necessity of structural weakness is fundamental. Discontinuities in form of joint and cracks enable infiltration of water, which further facilitates for frost shattering and chemical weathering to proceed (Whalley et al., 2004). Cracking of the bedrock are initiated by stress release, and presence of permafrost provides for saturation in the blockfield bed during summer. Upon winter freezing these conditions provides for further cracking and rock disintegration. Crack growth may also be assisted by oxidation of Fe along mineral surfaces (Goodfellow et al., 2008). Frost wedging are not capable of crack generation itself (Boelhouwers, 2004), it depends on water availability upon freezing and the presence of cracks, and is linked to blockfields in permafrost environments (Ballantyne, 2010). Formation of ice have the ability to generate and propagate cracks in rocks, followed by raised temperatures and thawing, this leads to weakening or detachment of rocks (Matsuoka and Murton, 2008).

Microgelivation comprises the generation and growth of microcracks, enlargement and merging of pores, granular disintegration and small flaking. Granular disintegration and small flaking leads to the production of fine sediments (μm -to- cm scale) (Matsuoka, 2001a; Matsuoka, 2001b), and granular disintegration is proposed to be the cause leading to edge-rounding of exposed boulder surfaces (Ballantyne, 2010). *Macrogelivation* tends to produce coarser materials (cm -to- m scale) and results from widening and lengthening of pre-existing macrocracks experiencing freezing of water-filled cracks (Matsuoka, 2001a; Matsuoka, 2001b).

Laboratory experiments have shown production of silt through frost weathering, which Goodfellow et al. (2008) interprets as the likely primary source for development of fine matrix in blockfields. Chemical weathering alteration of fine matrix strikes after the initial physical breakage from the parent rock.

The process of mechanical weathering cause breakage of rocks into smaller fragments without any significant changes to the chemical or mineralogical composition (Boggs, 2011).

Thermal stress occurs as an effect of a combination of cold air and heated rocks (Hall et al., 2002). Warming may cause the rocks to expand, while cooling lead to contractions, determined by the minerals present. Two types of thermally induces stress may cause rocks to fracture; thermal stress fatigue and thermal shock, differentiated by the degree of stress applied. Low frequent thermal stress may cause failure over time, while thermal shock has an immediate impact caused by rapid change in temperature (Hall, 1997; Murton, 2007).

Wetting and drying may cause weathering due to fluctuations of rock moisture. High amount of moisture content makes a lasting expansion of the rock even after moisture loss, which weakens its strength. Cycles of wetting and drying may also weaken the bonding strength of the minerals causing loss of strength and possible failure (Hall and Hall, 1996).

2.3.3 Biotic weathering

Biotic weathering is separated into biochemical weathering and biomechanical weathering. The process of biochemical weathering describes how micro-organisms (algae, lichen, fungi) may enhance chemical alteration of minerals in cold environments, while biomechanical weathering concerns grain and flake detachment of rocks (Ballantyne, 2018).

The occurrence of lichen may cause exfoliation of rocks, by growing on and within rocks, dissolvment of cement and hyphaes penetrating into the rocks, volumetric expansion and contractions of thallus (Murton, 2007).

Lichen presence enhance the weathering rate of plagioclase and olivine, due to organic anion production that lower the activation energy necessary for plagioclase dissolution (Arocena and Hall, 2004). The activity of lichen is partly controlled by the experienced thermal conditions, which is partly controlled by its color. The color of the lichen affects the thermal conditions beneath.

2.3.4 Controlling factors on weathering

The two depending factors controlling the rate of weathering are climate and lithology (Boggs, 2011).

2.3.4.1 Climate

Climate is assumed to influence landscape evolution in regard to its controlling effect on erosion and weathering processes. (Dixon et al., 2009). Both physical and chemical weathering depend on the presence of warmth and moisture within the ground surface. (Dixon and Thorn, 2005). Chemical weathering processes taking place in periglacial environments are no different

to those operating in other climates, with regard to the high degree of temperature independence, sufficient moisture availability, and favorable ground environment in general (Dixon and Thorn, 2005). Temperatures below the freezing point prevents chemical weathering from happening, while temperatures above have the tendency to increase the process (Ballantyne, 2018). Temperature is proposed to have a controlling effect on production of clay due to liquid water availability, which could restrict chemical weathering by reduced biological activity (Goodfellow, 2012). Precipitation regime controls the degree of leaching, the surface and subsurface runoff of dissolved solids (Ballantyne, 2018).

2.3.4.2 Lithology

Lithology is proposed to play a major control on rates of weathering by influencing the mineral availability (West et al., 2005). Lithology comprehends rock type, mineral composition, grain size and porosity (Boggs, 2006). Lithology influence the rate of dissolution of different mineral phases (White and Brantley, 1995). Minerals crystallize at different temperatures. Olivine and Ca-plagioclase crystallize at high temperatures from magma, and such minerals tend to be more unstable than minerals that crystallize at lower temperatures. Feldspar, biotite, albite and muscovite tends to have intermediate stability, while quartz usually is the most stable mineral. Minerals that crystallize at high temperatures are characterized by weaker ionic or ionic-covalent bonds (Faure, 1998; Boggs, 2006; Ballantyne, 2018). Quartz and K-feldspar are relatively resistant to weathering and diagenesis. Plagioclase, mica, chlorites and carbonates tend to be easily altered (Jeong et al., 2008).

2.3.5 Clay mineralogy

Weathering sites consists of secondary minerals, such as, clay minerals, iron oxides or hydroxides, and aluminum hydroxides (Boggs, 2011). The chemical alteration of primary minerals into secondary minerals reflects the nature, intensity and extent of the chemical weathering processes (Allen et al., 2001). In situ weathered minerals are mainly a product of hydrolysis and oxidation (Boggs, 2011).

Secondary clay minerals result from chemical alteration of primary minerals. Chemical reactions operate at slower rates in low temperature environments, which implies that presence of secondary minerals in periglacial regolith indicate prolonged stability (Hopkinson and Ballantyne, 2014).

Illite is a product of chemical weathering of K bearing minerals, mainly biotite but may also be a product of K feldspar. Illite occurs in various climates and occurs more frequently in blockfields than other regoliths (Goodfellow, 2012).

Kaolinite forms through a longer and more intense leaching conditions than illite and smectite (Boggs, 2011), in silicate mineral groups, excluding quartz (Goodfellow, 2012). Similar to Illite it is not associated with any specific climate (Ollier, 1984).

Gibbsite is an end product of chemical weathering, with an origin from Al-bearing silicate minerals (Goodfellow, 2012), forming through even more intense chemical weathering conditions than kaolinite (Boggs, 2011). Presence of gibbsite are in general expected in periglacial environments with precipitation and seasonal thaw (Goodfellow, 2012).

Smectite is a common product in silicate mineral groups, excluding quartz,

The most common end product of chemical weathered silicate minerals containing Fe are iron oxides (Goodfellow, 2012).

2.4 Blockfields

Blockfield is a term describing a cover of bouldery regolith in periglacial environments (Ballantyne, 2010). The occurrence of blockfields is dependable on lithologies favorable of block production (Boelhouwers, 2004). Two types of blockfields can be found, differentiated by the source of the regolith. Autochthonous blockfields has its origin in in-situ weathering of bedrock, elevated to the surface through frost heave. Allochthonous blockfields are formed through material transport from external sources (Boelhouwers, 1999, Rea et al., 1996). The blockfield mantled surface usually cover clasts of fine matrix; sand, silt and clay (Rea et al., 1996). Excavations in autochthonous blockfields have usually reached a depth of 1 m, and in some cases 2 m, before reaching the bedrock (Ballantyne, 2010).

2.5 Origin and development

The age and origin of blockfields have been widely discussed through the years, hence two models have been proposed to explain the development; the Neogene model and the periglacial model (Ballantyne, 2010).

2.5.1 The Neogene hypothesis

The assumptions behind a Neogene origin is based on chemical weathering and characteristics linked to the warmer and more humid climate in that era. Modification of the pre-existing regolith cover is thought to be a product of frost sorting during Quaternary. The presented evidence supportive of this comprises the high clay volume in the fine matrix, and limited evidence of frost wedging on glacially smoothed bedrock in cold environments. The presence of saprolite and secondary minerals, preferably gibbsite and kaolinite, in blockfield soils are assumed to indicate preglacial weathering. Clay-rich saprolites is seen as a strong indicator for Neogene age (Ballantyne, 2010).

2.5.2 The periglacial hypothesis

The periglacial model sees blockfields as developed by weathering and frost sorting during cold conditions in Quaternary (Ballantyne, 2010). Evidence proposed by Goodfellow et al. (2008) from blockfields in Northern Sweden, suggests an origin during Quaternary and Holocene, based on the dominance of physical weathering processes, although minor chemical weathering is present in fine matrix and clasts. The perception is that due to frost weathering in the lower parts of the active layer, blocks are formed in relation to seasonally refreezing. (Goodfellow et al., 2014)

Goodfellow et al. (2008) underlines that blockfields may have origin in different periods, meaning both Neogene and Quaternary/Holocene can be responsible for blockfield development, highlighting that blockfields differ from each other, and they are not all the same. The perception of the “glacial buzzsaw” has been challenged by evidence of landforms surviving beneath the cold-based ice with non or minimum modification (Kleman, 1994). Other assumptions postulated is that blockfields represent summits protruded as nunataks during LGM (Ballantyne, 1998). Meltwater channels have been identified to have eroded blockfields, thus suggesting it has been preserved below cold-based ice sheets (Ballantyne, 2010).

Several factors support an old origin of blockfields, consists of current inactivity, surface blocks with large occurrence of lichen, slow weathering rates of intact bedrock, preservation beneath former ice sheets (Goodfellow, 2007). Whalley et al. (2004) implies blockfield formation to be at least of Neogene age, possibly Mesozoic. According to Goodfellow (2012) there is no clear evidence of a Neogene origin, as nearly all characteristics points to physical and chemical weathering during Quaternary. Chemical weathering also occurs in humid periglacial environments, and has the ability to produce gibbsite and kaolinite, at a slower rate,

during Quaternary. The presence of gibbsite may be explained by liquid water in regolith in seasonally periglacial environments (Goodfellow et al., 2014; Hopkinson and Ballantyne, 2014). According to Boelhouwers (2004) formation of periglacial blockfields is possible through microgelivation in porous bedrock, and secondly, frost wedging in bedrock consisting of fractures.

The presence of erratic blocks indicate that Tron has been covered by ice at some point, but were probably nunataks during most of the glacier periods (Engelien 1995). No evidence of glacial erosion has been identified, and the presence of a thick blockfield suggests limited glacial modification (Strømsøe and Paasche, 2011).

Techniques utilized to determine blockfield age and origin has been put steps forward through measurements of cosmogenic nuclide concentrations. TCN concentrations in regolith can be combined with benthic $\delta^{18}\text{O}$ records, which may provide valuable information to better understand the complexity surrounding former ice-covered, now relict bedrock surfaces. Measurements of TCN concentrations are widely performed due to the possibility to investigate surfaces formerly covered by ice sheets (Li et al., 2007). Cosmogenic nuclides are proved to be accumulated only under non-glaciated periods (Stroeven et al. 2002). Data obtained by Stroeven et al. (2002) using the method mentioned above, infers blockfields as relict landforms that have been preserved under cold-based ice, suggesting an age between 605 ka and 1 Ma. Cold-based ice sheets have the capabilities to preserve weathered surfaces, such as blockfields, from the overriding ice (Sugden et al., 2005). By obtaining information through cosmogenic nuclide dating on bedrock surfaces in southeastern Norway, Linge et al. (2006) support a pre-Quaternary age of blockfields. The blockfield summits at Blåhø (1617 m.a.s.l) and Elgåhogna (1460 m.a.s.l) were most likely covered by low erosive ice during LGM, according to Goehring et al. (2008).

2.6 Tors and surface lowering

A tor is a remaining mass of bedrock protruding above its surroundings. Its formation is a result of differential weathering of exposed bedrock and the adjacent blockfield cover, due to higher erosion rates of the surroundings. The erosion rates are controlled by the resistance of the bedrock. The landform is present in all climates and on different lithologies (Ballantyne, 2010).

Quaternary surface lowering of blockfield surfaces are mainly explained by three processes; *glacial erosion, mass movement* and/or *in-situ weathering and erosion*. Glacial erosion may have modified the blockfield cover and lowered the surface during deglaciation. The mass

movement view emphasizes surface lowering as a result of debris transport by frost creep. The third alternative proposed are slow weathering of the blockfield cover and subsequently removal by wind or surface wash (Ballantyne, 2010).

2.7 Grain size and morphology

Particle morphology comprehends the parameters form, roundness and surface texture, all providers of valuable information of origin, transport and depositional environment of the sediments (Barret, 1980; Benn and Ballantyne, 1993; Blott and Pye, 2008). The parameters are independent of the.

Form reflects the outline and variations in proportions of the particle. Roundness is a measure of the sharpness of the particle corners and edges. Surface texture accounts for the relief between the corners. The surface may be smoothed by polishing or contain ridges, fractures, scratches and pits. The surface texture may be a product of various processes, such as mechanical abrasion during transport, tectonic polishing, chemical corrosion and etching. (Barrett, 1980; Blott et al., 2004; Blott and Pye, 2008; Boggs, 2011)

Shape of particles are measured by the long-, intermediate-, and short- particle axes (L, I, S). The term equant is used for particles with equal lengths of all the axes. Platy particles have equal L- and I-axes, with a small S-axis. Elongated particles have a L-axis significantly longer than the I- and S-axis (Benn, 2007).

Three processes that cause wear of particles are abrasion, impact and grinding. The size, shape and surface texture of sediments change during abrasion, and this change is controlled by size, angularity, rock type, rigor, and distance. Gravel-sized angular particles experience rapidly rounding with movement equal to 25 km. (Krumbein, 1941).

A common perception regarding the shape of the matrix is that angular sediments is a diagnostic feature for a frost weathering origin of blockfields. The form of clasts is strongly influenced by their lithology. Crystalline rocks (gabbro, gneiss and granite) have the tendency to produce equant-shaped particles, while sandstones and shale usually produce platy-formed clasts. Macroglivation usually produce angular clasts, while microglivation increase roundness by weathering of edges and corners (Benn, 2007).

The particle-size is fundamental and affects entrainment, transport and deposition (Blott et al., 2004). Particle size reflects the weathering and erosion processes at the specific site, which holds valuable information (Boggs, 2006).

2.8 Loess

Loess is a clastic sediment of aeolian origin, and commonly consists of silt sized particles (Pye, 1995; Haase et al., 2007; Sprafke and Obreht, 2016). In addition to silt-sized particles, loess deposits usually consist of sand and clay (Pavelić et al., 2016). Three mechanisms are involved in the formation of loess deposits, which are particle formation, particle transport, and particle deposition (Wright, 1995). The production of silt-sized particles is assumed to include; the release of existing silt-sized particles from the parent rock, glacial grinding, fluvial abrasion and crushing, aeolian abrasion, salt weathering, chemical weathering, clay pellet aggregation, and biological processes (Pye, 1995). Production of silt-sized fractions through comminution of coarser fractions are numerous, and includes; salt weathering, insolation weathering, frost weathering, aeolian abrasion, and fluvial abrasion (Smith et al., 2002). The features of loess vary on a global scale in regard of thickness, grain size, mineralogy, geochemical composition and characteristics, morphology and color. The variation throughout the world reflects the geological nature and the effectiveness of sediment mixing. Loess deposits are usually modified by reworking during or post-deposition, by bioturbation, weathering and pedogenesis. Loess deposits have been identified to mainly consist of quartz, in addition to minor input of feldspar, carbonates, both heavy and clay minerals. Silt sized particles, ranging from 2-63 μm , constitutes at least 50% of the loess deposits, but the median size of loess particles lies within the range of 20-40 μm (Pye, 1984; Pye, 1995). Silt-sized particles is optimal for wind transport, and loess deposits may be found from hilltops to valley bottoms (Ollier, 1984), and is suggested to cover as much as 10% of the Earth's surface (Muhs et al., 2004). Grains $>20 \mu\text{m}$ settles quickly when the turbulence initiated by strong wind decreases, while smaller size fractions may remain for days or weeks in suspension. Long distance transported material in Earth's atmosphere is majorly fractions smaller than 10 μm , and many are smaller than 2 μm . Continental loess deposits are usually composed of particles within the 10-50 μm size range, while particles that are transported great distances and deposited in oceans are mainly smaller than 10 μm (Pye, 2015). The minerals constituting the Pleistocene loess in Hungary, are quartz (20-50%), carbonate minerals (10-40%), micas (10-15%), feldspars (5-15%), clay minerals (5-25%), and minor occurrence of the heavy minerals. Similar mineralogy has been identified at Paks, Hungary and from loess deposits in Serbia (Újvári et al., 2010).

Loess are mostly of Pleistocene age, when large amount of silt-sized particles where produced by glacial grinding (Pavelić et al., 2016)

The grain shape of silt in loess depends on the mechanisms responsible for its formation, crystallographic characteristics and weathering history, but the grains are majorly blocky and angular/subangular. The formation of silt grains in chemical weathering environments tend to lead to edge-rounding as a result of solution and reprecipitation processes. Grains formed by through mechanical crushing usually show sharp edges (Pye, 1984).

2.8.1 Quaternary dust transport

Dust transportation in the atmosphere is an important tracer of atmospheric circulation. In polar environments, ice cores reaching back to the last glaciation has shown that the dust concentration in ice significantly varies with climate (Andersen et al., 1998).

Three processes proposed to explain the dust depositions in glacial climate are; a more vigorous atmospheric circulation, a weakened hydrological cycle, and extended source areas of dust due to soil moisture changes and/or reduction of vegetated cover (Mahowald et al., 1999).

Last Glacial Maximum marks the transition from Pleistocene to the Holocene, and during this period, Europe was characterized by dustier, colder, windier, and less vegetated conditions than the present. The dust cycles over central-Europe during LGM are hypothesized to be dominated by eastern winds. The patterns of emission and deposition rate of the eastern winds, indicate major westward transport of dust along the south and east margin of the Eurasian ice sheet. Simulation of dust emission indicates that European dust mostly was emitted from areas between the Alps, the Black Sea, and the Eurasian ice sheet. Significant dust amounts from areas within W-Poland, E-Germany, and Czechia were transported northwestward to N-Germany, Denmark, S-Sweden, and the North Sea (Schaffernicht et al., 2020).

Records from ice cores and marine sediments have suggested that the average deposition rates of aeolian sediments were 2-20 times higher during glacial periods than interglacial periods (Mahowald et al., 1999).

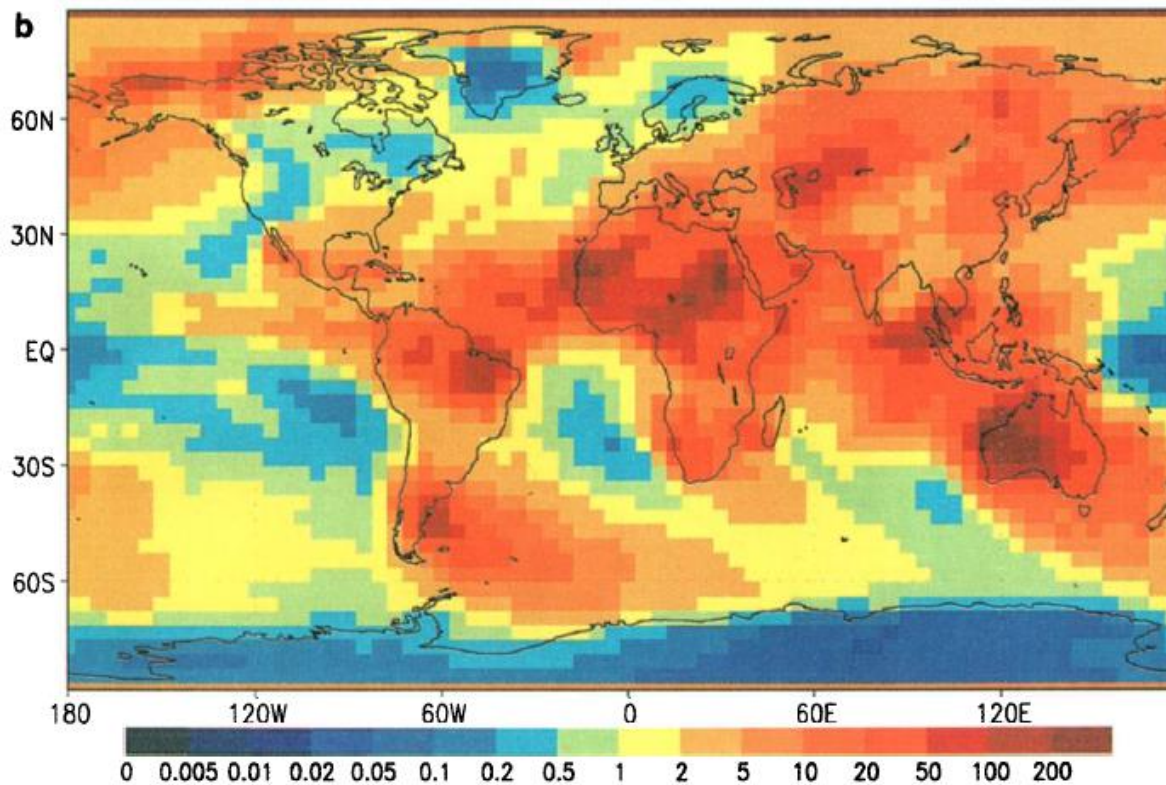


FIGURE 2.1 SIMULATED DUST DEPOSITION ($\text{G M}^{-2} \text{YR}^{-1}$) DURING LAST GLACIER MAXIMUM (MAHOWALD ET AL., 1999).

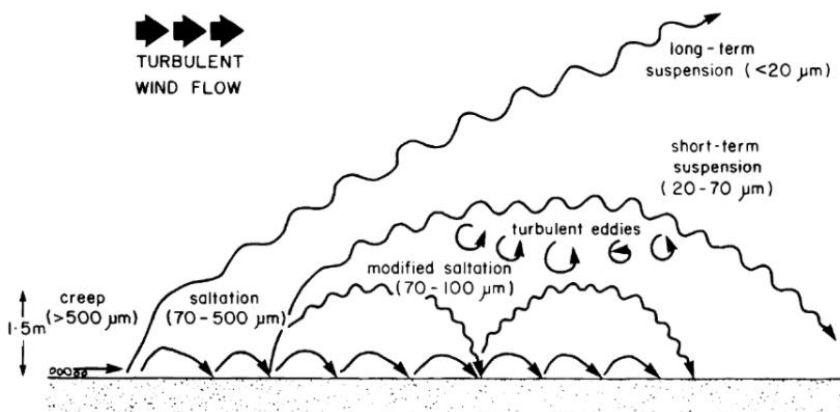


FIGURE 2.2 DIFFERENT MODES OF AEOLIAN TRANSPORT (PYE, 2015).

Sediment transport by wind are usually divided into creep, saltation and suspension (as shown in fig. 2.2) (Vandenberghe, 2013; Pye, 2015). The rate, height and distance of sediment transport depends on the amount of sediments available, grain properties, and the wind strength. Deposition of sediments depends largely on suitable dust traps in the terrain (Vandenberghe, 2013).

Aeolian transported sediments are often affected by reworking post-deposition, which cause sorting of the particles and may mix with other sediments (Vandenberghe, 2013).

3 Methods

The methods forming this thesis involves the approach in sediment sampling and the laboratory analysis in form of Scanning electron microscope (SEM) based Automated Mineralogy (AMS), and classification of coarse fractions.

3.1 Sediment sampling of pits

Two pits were manually excavated in the blockfield. For each pit four horizontal soil profiles were sampled for analysis of weathering characteristics and soil variation, at the same depth interval of 20-30, 40-50, 60-70 and 80-90 cm. In addition, two vertical profiles were sampled for the OSL-dating at the depths of 30-40 and 50-60 cm.

The first visit to Tron took place on September 17th in weather conditions constantly changing between clear sky and snow blizzards. The temperatures during the nights beforehand and the following mornings were below 0°C, climbing above during the day. The surface cover of TrP1 consisted of a mixture of gravel and fine sediments in-between sporadic boulders. A depth of 1 meter was excavated into the soil. The uppermost 20 cm was completely frozen.

The next visit happened on September 23th following a period of warmer temperatures. Clear blue sky and temperatures well above 0°C made the overall conditions more satisfying. In contrary to the last field work the soil was completely unfrozen making it easier to breach the top layer and made the soil more accessible. The walls in the pit were relatively unstable due to the change in conditions, which led to collapsing of the walls. The sediments were quite saturated, which suggests that the frozen uppermost zone from the first visit had thawed out in accordance with the rising temperatures during this period. The surface was mixture of boulders, gravel and a mixture of fine sediments. The soil was characterized by unsorted material with presence of gravel throughout the pit. The diameter of the largest gravel was measured to 10 cm, and were found at 75 cm depth. A depth of 95 cm was reached, 5 cm short of the depth of TrP1.



FIGURE 3.1 SURFACE COVER OF TRP1.



FIGURE 3.2 SURFACE COVER OF TRP2 PRE-EXCAVATION. PLOT MARKED BY DIGGING BAR.

3.2 Laboratory techniques

The samples were weighted pre and post drying in order to obtain moisture content. All samples were dried in a Termaks TS8024 oven set to 40°C as preparations to conduct the dry sieving. Following Blott and Pye (2012) classification, the range from medium gravel (8-16 mm) to very coarse gravel (32-64 mm) were filtered out from the finer sediments in order to photograph and describe shape and characteristics. Samples of fines were dry sieved for the <2 mm to >63 µm size fractions. Each size fractions were weighted to establish the percentage of each sample.

3.2.1 Grain-size analysis of coarse fractions

The coarse fractions of the sediment samples were classified according to Blott and Pye (2012) with measuring tape. The size range of the fractions ranged from medium gravel (8-16mm), Coarse gravel (16-32mm), very coarse gravel (32-64mm) to very small boulder (64-128mm). This was done in order to get a distribution of the coarse material from every depth sampled in both pits, giving the opportunity for a comparison of the vertical transect.

3.2.2 Grain morphology and mineralogy characterization of coarse fraction

The aim of the clast form analysis is to clarify the lithology, weathering and movement of the substrate. In order to obtain such information, the morphometrics; *shape*, *roundness* and *mineralogy* are interpreted.

The gravel separated from the finer-grained fractions was spread out on a paper sheet and photographed giving the advantage of a clear visual classification. Following the roundness and sphericity classification of Powers (1953) (Fig. 3.3) every particle was classified accordingly.

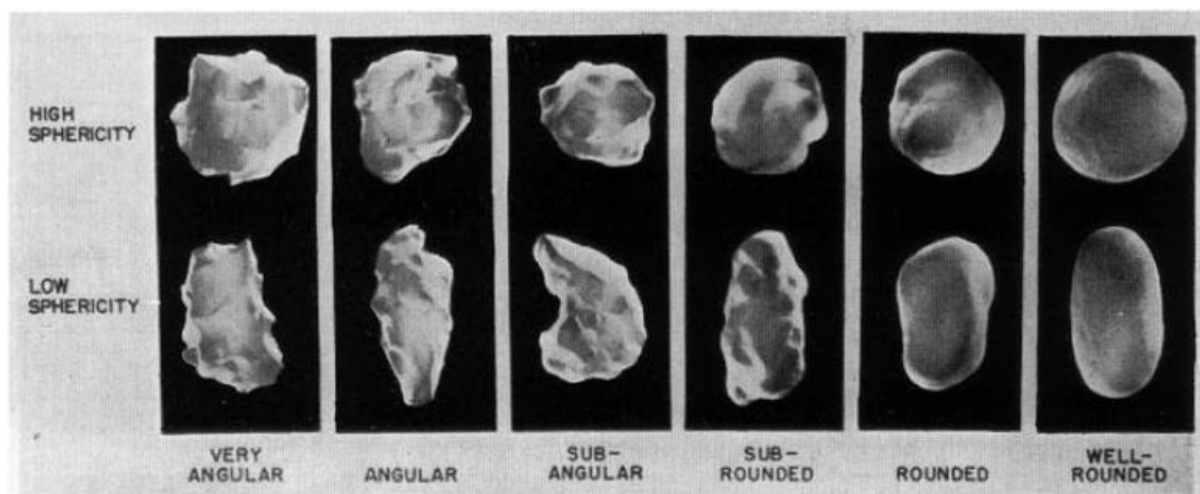


FIGURE 3.3 ILLUSTRATION OF PARTICLE SHAPE CLASSIFICATION (POWERS, 1953).

The variations of the gravel sphericity are split into the terms; *equant*, *elongated* and *platy*. *Equant* meaning that the long-, intermediate- and short-axis are similar. *Elongated* describes the L-axis to be significantly longer than the I- and S-axis. *Platy* refers to gravel with a S-axis considerably smaller than the L- and I-axis (as visualized in fig. 3.4).

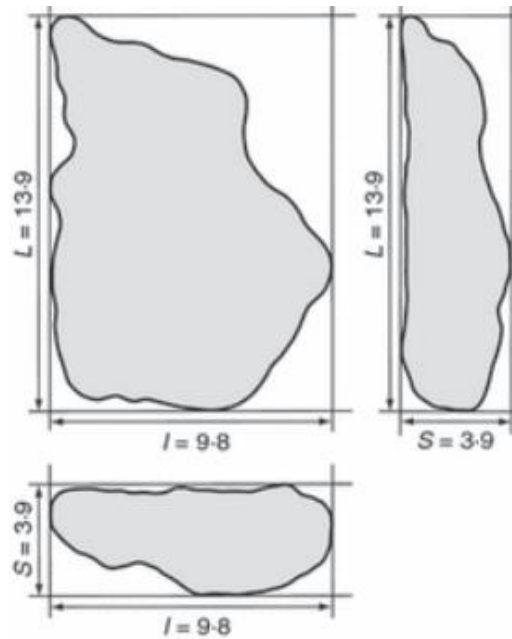


FIGURE 3.4 VISUALIZATION OF LONG(L), INTERMEDIATE (I), AND SHORT(S)-AXIS (BLOTT AND PYE, 2008).

3.3 Automated mineralogy analysis

3.3.1 Overview

In order to maximize information about mineral formation and processes affecting them, accurate identification of minerals and quantification of their abundance is essential. Automated mineralogy analysis is able to measure all particles in a sample, and commonly are a minimum of 300 grains used to produce modal mineralogy with statistical validity. To capture the information with most relevance, a size range of the measurement is set to exclude unnecessary particles. The next step is to determine the stepping interval of the electron beam, which are based on desired resolution and the size range encapsulating the minerals of interest. The AMS then systematically maps the chemistry and particle sizes, which subsequently provides modal mineralogy, particle and grain size and morphology (Pirrie and Rollinson, 2011).

Automated mineralogy systems are generally a combination of scanning electron microscope (SEM), backscattered electron (BSE) and energy dispersive spectrometry (EDS) (Bushell,

2012). This quantitative analytical technique has the advantages to provide valuable information of particle and grain properties (such as size, shape and texture) (Røisi and Aasly, 2018). The last years have shown an increase in developments of scanning electron microscope energy dispersive spectrometry automated mineralogy (SEM-EDS-AM), giving way to the 2nd generation of SEM-EDS-AM containing the ability to classify particles and distinct types of particles (Graham, 2017). Automated quantitative mineralogy is an ideal tool to visualize and quantify minerals, morphology and chemistry of sediment samples (Keulen et al., 2020). High-resolution BSE images provides important morphology parameters, such as *area*, *elongation*, *feret maximum diameter* etc., and used in combination with textural features it improves understanding of mineralogy and textural characteristics (Graham et al., 2015; Graham, 2017).

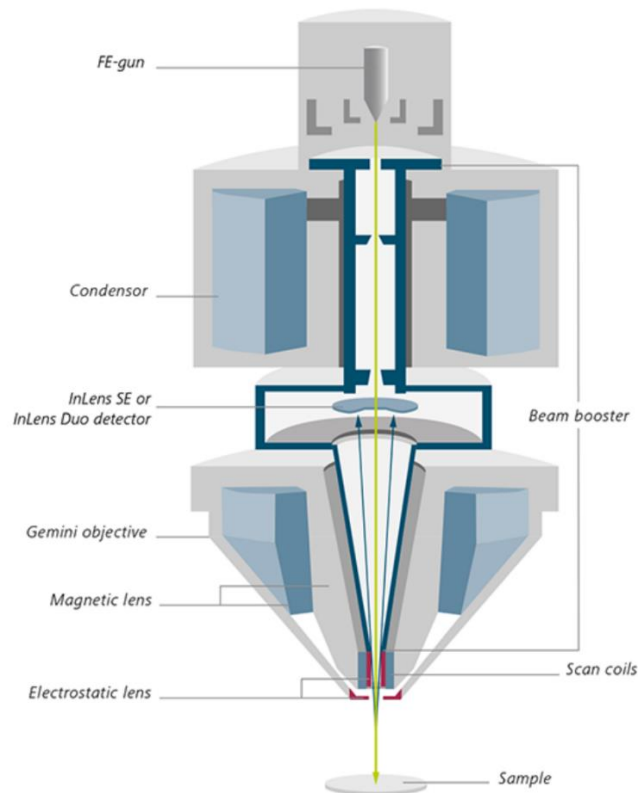


FIGURE 3.5 OVERVIEW OF THE TECHNOLOGY (ZEISS, 2020)

The field emission SEM uses a focused electron beam that scans the surface of the input sample in order to generate an image or an analysis. The FE-gun emits electrons that pass through the anode aperture. The electron beam is focused on the sample by the objective lens, which consists of an electromagnetic and electrostatic lens. When the primary electron beam hits the sample, secondary electrons and backscattered electrons are generated due to electron beam

interaction processes. The detector creates images and produce information from the samples properties by detecting signals from the secondary electrons and backscattered electrons.

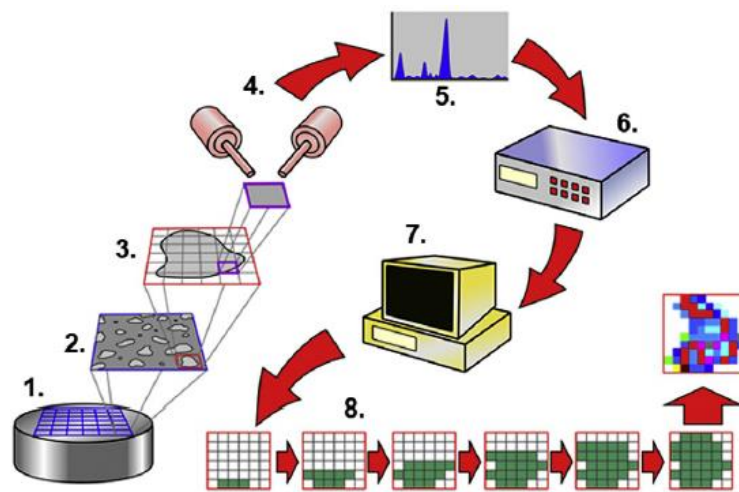


FIGURE 3.6 VISUALIZATION OF THE STEPWISE PROCEDURE (ROLLINSON, 2019).

The stepwise example of a QEMSCAN procedure in fig 3.6 involves (1) scanning of the sample, (2) backscattered electron to differentiate particles, (3) scanning of particles or area on micron pixels, (4) each analysis point or pixel examined by the EDS X-ray detectors, (5) the acquired chemical spectrum, (6) Processing of the chemical spectrum, (7) identification of minerals based on mineral recipe, (8) creation of false-color image with pixel mineral classification (Rollinson, 2019).

3.3.2 Procedure

The analysis was done by the Department of Geoscience and Petroleum, NTNU using the Zeiss Sigma 300 field emission SEM equipped with Bruker EDS, panchromatic CL and high-speed EBSD, and with the Zeiss Mineralogic mining v1.06.03 automated quantitative mineralogy software.

As preparation for the AMS, the fine-grained samples consisting of $>63 \mu\text{m}$ were weighed and 2g of sample from every depth was extracted and mixed with 0,5g graphite. Adding graphite has a positive effect of preventing touching particles (clumping and coagulation), hence improving the analysis of each particle (Røisi and Aasly, 2018). Polished blocks were prepared by the Department of Geoscience and Petroleum, NTNU.

The samples were analyzed by two modes: *Spot Centroid (SC)* and *mapping*. The mapping mode analyze each grain of the sample making it more time consuming, but on the other hand more detailed information are obtained. This mode analyzes each pixel of an overlaying grid resulting in a detailed map of the sample (Keulen et al. 2020). Spot Centroid identify individual grains and assign their mineral composition based on analysis at the center of the grain. This interpolation of each grain decreases the time of measurement due to less points getting measured, but may have the disadvantage of making each grain mono-mineralic. The software Zeiss Mineralogic were applied to process the minerals based on an input of a mineral recipe of the expected minerals in the lithology of Tron. Mineralogic have different ways to visualize the results from the same samples. This analysis is visualized in false-color to separate different minerals, and in greyscale to improve morphology differences. In table 3.1 the parameters set for both analyses are listed.

TABLE 3.1 ANALYTICAL CONDITIONS FOR MINERAL MAPPING AND SPOT CENTROID-ANALYSIS

Analysis mode	Acceleration voltage (kV)	Working Distance (mm)	Aperture Size (µm)	Mapping Step Size (µm)	Pixel Size (µm)	Magnification
Mineral mapping	20	8,5	120	2,5	X	178,6X
Spot Centroid	20	8,5	120	X	625,14	178,6X

3.3.2.1 Grain morphology classification and distribution of fine fraction

Analysis of the morphology of the silt-sized fractions (2-63µm) were done by extraction of the morphometric values assigned to each particle. *Feret max diameter* is the measurement of the largest diameter of the particles. *Area* describes the area of the particle. *Perimeter* measures the silhouette of the particle, where high values reflects irregular shapes. The *compactness* of the particles is calculated with the equation below. By combining these parameters, the aim is to obtain information in regard weathering and transport processes responsible for the morphology.

$$Compactness = Perimeter^2 / (4 * \pi * Area)$$

3.3.2.2 Grain-size distribution of fine fraction

In order to investigate grain-size distribution of the fine fraction, Zeiss Mineralogic provides features, such as modal mineralogy, which contains data containing grain-size, mineral abundance, liberation and association. Modal mineralogy presents a list of the minerals occurring with their weight percentage assigned. In regard to sediment particles, the grain size is the most fundamental property (Blott and Pye, 2001). Grain-size distribution curves of the silt fraction are produced to compare similarities and /or variations between depths in each pit respectively, and between both pits.

3.3.2.3 Mineral abundance

To assign minerals to the silt-sized particles, the samples from each depth in both pits were analyzed by the Spot Centroid-analysis mode. The mapping analysis was performed only on the sections comprising TrP1. Establishing the mineral occurrence and abundance in the soil of the summit plateau provide valuable information considering subsurface processes, which will be correlated to findings reported in earlier research. Comparison of the modal mineralogy from each sampled section can illuminate the vertical movement of the sediments and to what degree sediment sorting occurs. This way the similarities and variations within, and between, the designated pits can be made.

4 Results

The following subchapters will present classification of clast morphology and size distribution. Subsequently, the output of the Automated Mineralogy-analysis of the silt fractions (2-63 μ m) will be presented by modal mineralogy, mineral abundance, grain-size and morphology. Results from two analysis modes (Spot Centroid and Mapping) will be presented and compared. The resulting values in the following tables and figures are separated into their respective pits and depths, TrP1; S1(20-30 cm), S2(40-50 cm), S3 (60-70 cm) and S4 (80-90 cm), TrP2; S5 (20-30 cm), S6 (40-50 cm), S7 (60-70 cm) and S8 (80-90 cm).

4.1 General description of the pits

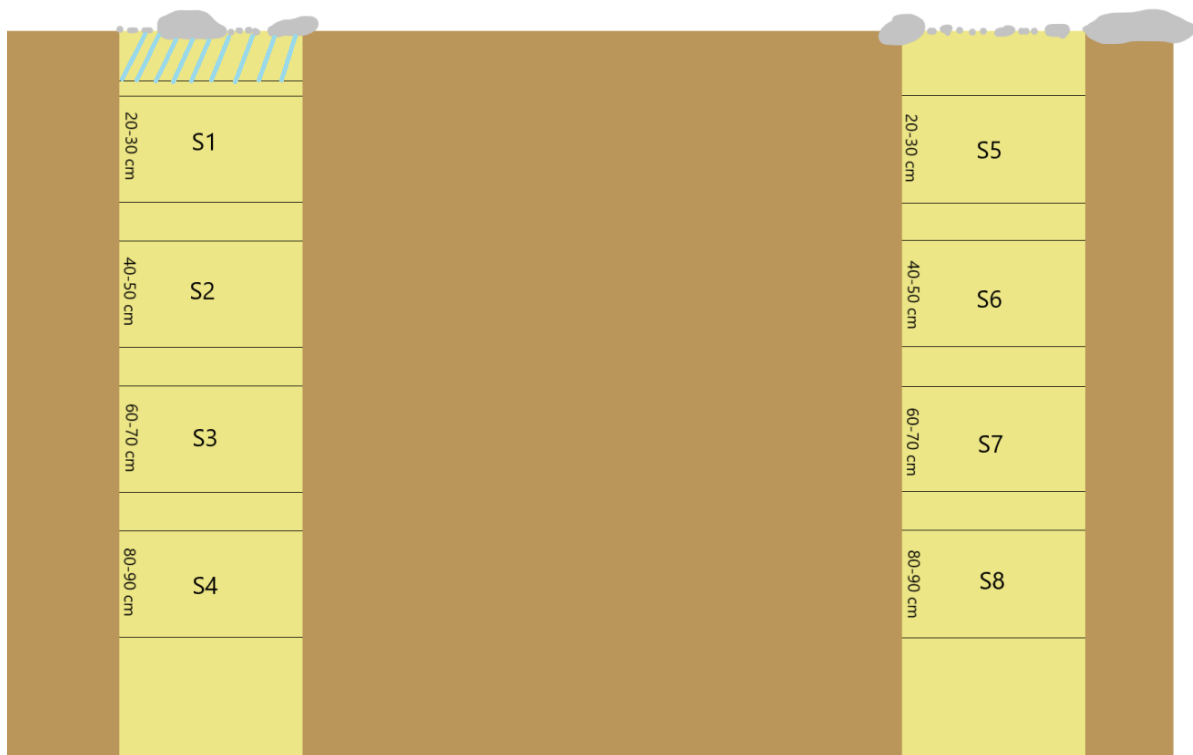


FIGURE 4.1 VISUALIZATION OF TRP1 (S1-S4) AND TRP2 (S5-S8) COLUMNS WITH DEPTH LABELS ATTACHED.

Fig. 4.1 is a visualization of the pits excavated during this work. The sections represent the depth of sediment sampling with label descriptions attached.

4.1.1 TrP1

The surface cover of TrP1 consisted of a mixture of boulders and gravel with a mixture of fine sediments in-between (fig. 3.1). The uppermost 15 cm in the soil were frozen, and contained largely fine sediments. A minor contributor to the uppermost layer came from sporadic gravel-sized fractions. A large boulder (512-1024 mm) was present at the depth of 30 cm which extended downwards. At a depth of 72 cm there was an occurrence of brownish soil, which may indicate traces of Fe-oxidation. At similar depth there was higher occurrence of gravel compared to the upper 50 cm.

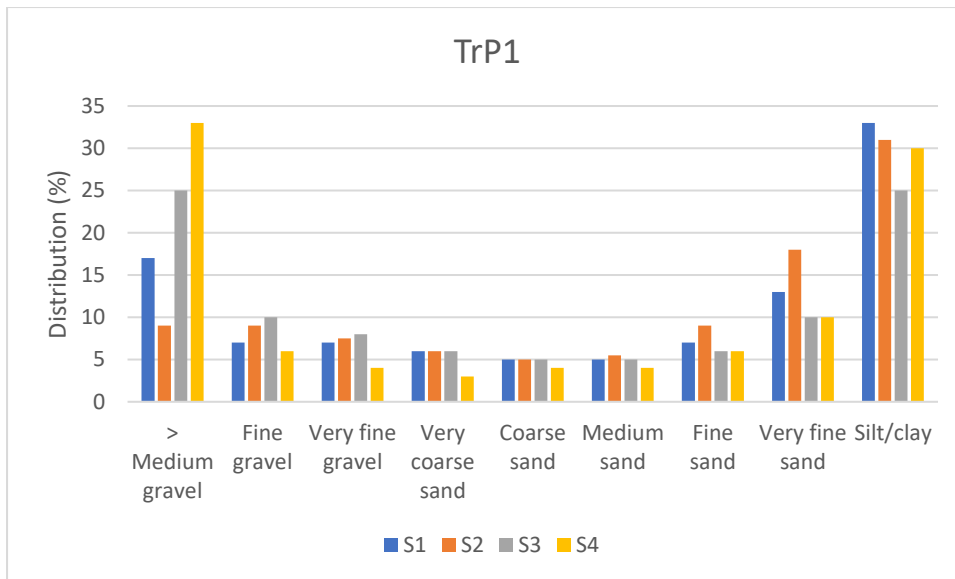


FIGURE 4.2 DISTRIBUTION (%) OF THE SEDIMENT COMPOSITION IN TrP1

Fig. 4.2 shows the grain-size distribution obtained by dry sieving of the samples constituting the depths in TrP1. The amount of >medium gravel (>8mm) lies at slightly above 15% in S1 (20-30 cm), while it decreases in S2 (40-50 cm) and then occur at higher rate with depth. Both fine gravel (4-8 mm) and very fine gravel (2-4 mm) increase with depth in the uppermost three sections before a decrease in S4 (80-90 cm). Very coarse sand (1-2 mm) and coarse sand (500 μm -1 mm) occurs at a steady rate from S1-S3, while the amount decreases in S4. Medium sand (250-500 μm), fine sand (125-250 μm) and very fine sand (63-125 μm) have the highest occurrence in S2. Both medium and fine sand is relatively even in their distribution between depths. The very fine sand has similar distribution in S3 and S4. The silt/clay amount decrease from S1-S3 before it increases in S4.

4.1.2 TrP2

The surface layer of TrP2 was a mixture of coarse sand and gravel, which is visualized in fig. 3.2. Detailed observations of the pit's stratigraphy were impossible due to the amount of saturation in regard to rising temperatures after a period of freezing temperatures. At depths of 50 cm a higher concentration of gravel was found in comparison to the upper parts of the pit. At 75 cm depth cobble-sized rocks could be observed. Organic matter was found in the samples extracted from the depths S5 and S6 cm in pit 2.

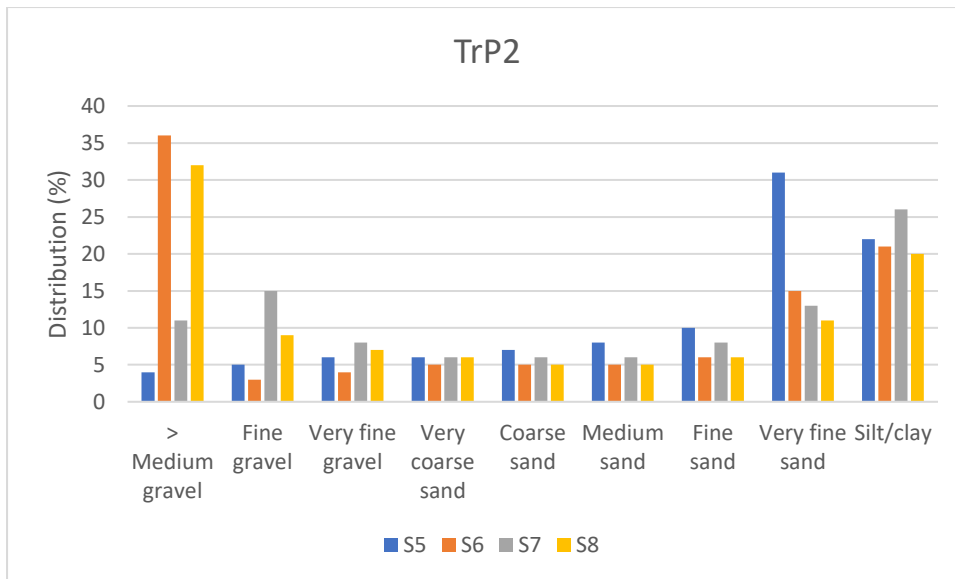


FIGURE 4.3 DISTRIBUTION (%) OF SEDIMENT COMPOSITION IN PIT2

Fig. 4.3 shows that the >medium gravel sized concentration vary between the depths, with high occurrence in S6/S8, while S5 reveals a scarce occurrence. The fine gravel peaks in S7 where it makes up to ~15% of the sample, in great contrast to S6 that consists of less than 5%. Very fine gravel is relatively consistent, with a minor decrease in S6. The amount of sand fractions shows a gradual increase from very coarse sand to very fine sand in S5. The amount of very fine sand decreases with depth. The highest amount of silt/clay occurs in S7, whereas S8 consists of the lowest amount.

4.2 Classification and description of grain morphologies of the coarse fraction

The clasts are classified in regard to size and morphology. The sizes are divided according to Blott and Pye (2008), with medium gravel (8-16 mm), coarse gravel (16-32 mm), very coarse gravel (32-64 mm), and very small boulder (64 –128 mm). The morphology is classified following the particle shape classification of Powers (1953).

TABLE 4.1 CLASSIFICATION OF GRAVEL SIZES AND SHAPE (%)

TrP1	Very small boulder	Very coarse gravel	Coarse gravel	Medium gravel	Angular	Subrounded	High sphericity	Low sphericity	Equant/Cubic	Elongated	Platy/Slabby
S1		4	38	58	97	3	71	29	76	7	17
S2			31	69	96	4	72	28	50	6	44
S3		8	38	54	97	3	72	28	78	8	14
S4		13	48	39	99	1	56	44	77	10	13
TrP2											
S5		5	38	57	100	0	62	38	64	15	21
S6		5	14	10	71	99	1	54	46	74	9
S7			8	44	48	97	3	75	25	68	11
S8			5	46	49	100	0	78	22	75	6

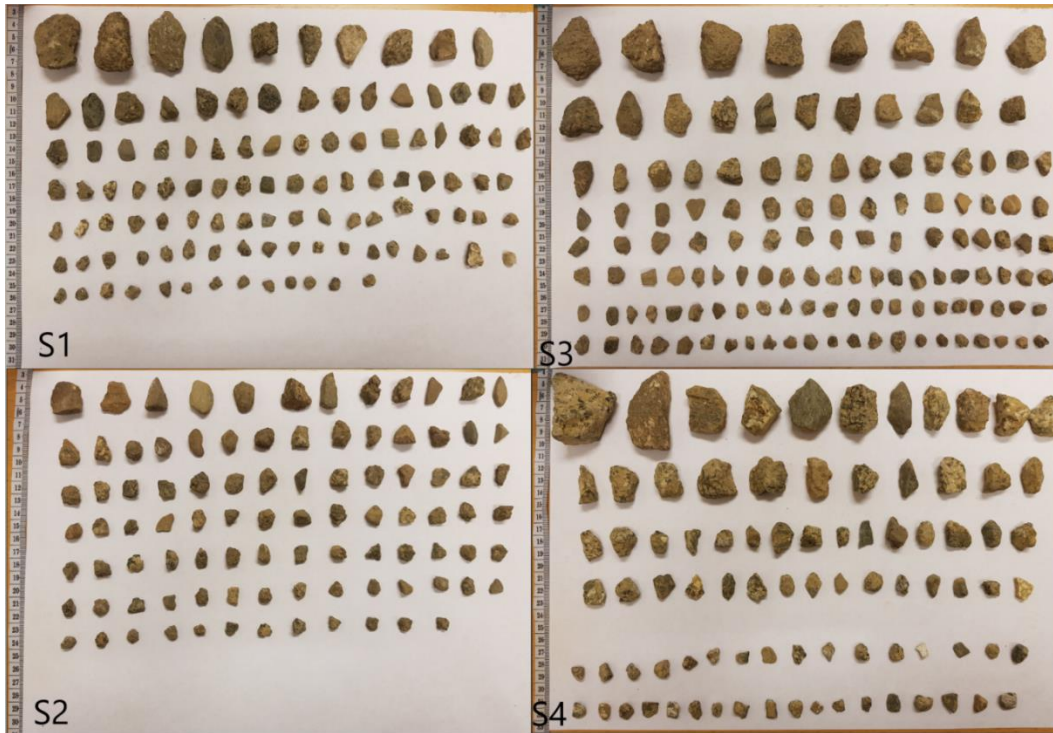


FIGURE 4.4 VISUAL SURVEY OF GRAVEL EXTRACTED FROM TRP1

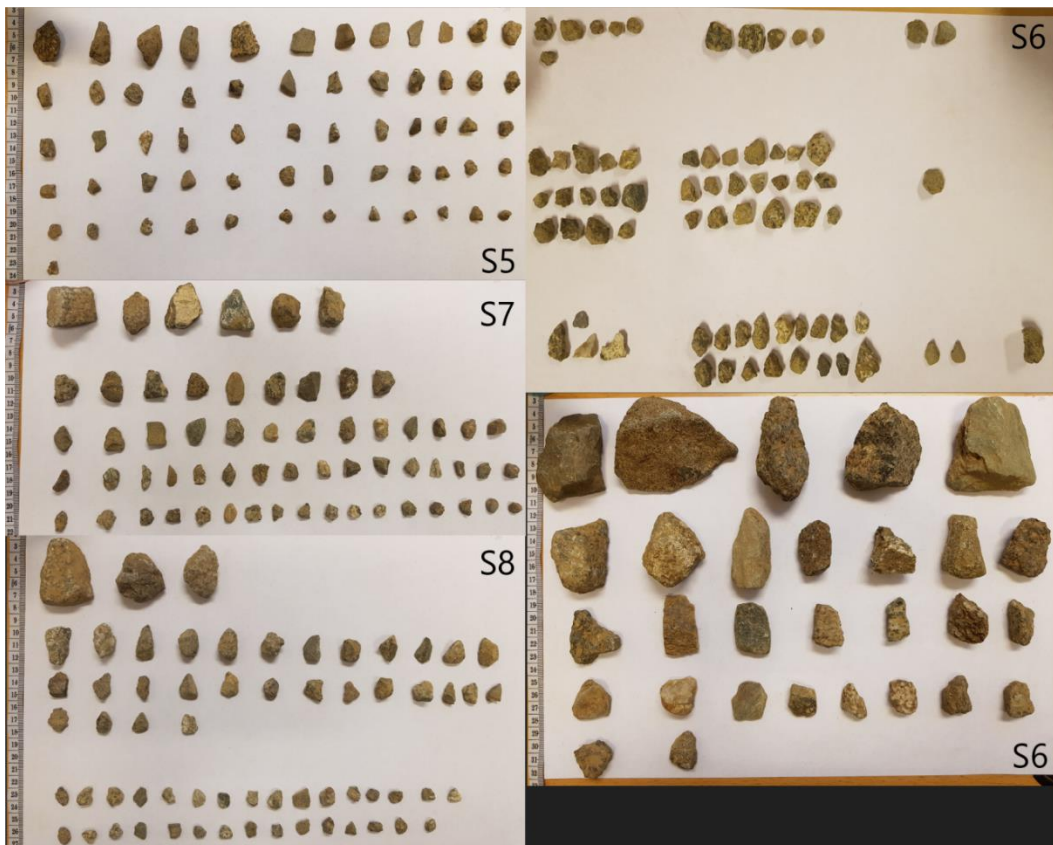


FIGURE 4.5 VISUAL SURVEY OF GRAVEL AND VERY SMALL BOULDERS IN TRP2

The sampled coarse fractions are to a high degree characterized by being angular, with >96% angularity in each depth (table 4.1). The highest occurrence of sub-rounded gravel was found in TrP1, where a small amount is present in each depth. S5 and S8 are the only depths not containing any sub-rounded clasts. Equant-shaped gravel dominates each dept of both pits, followed by platy shapes and elongated. Gabbro is the dominant rock type throughout the samples, as one would expect on this mountain.

4.3 Grain size distribution coarse fractions

The resulting grain-size distribution of the coarse fraction are classified in accordance to Blott and Pye (2012), with medium gravel (8-16 mm), coarse gravel (16-32 mm), very coarse gravel (32-64 mm) and very small boulder (64-128 mm).

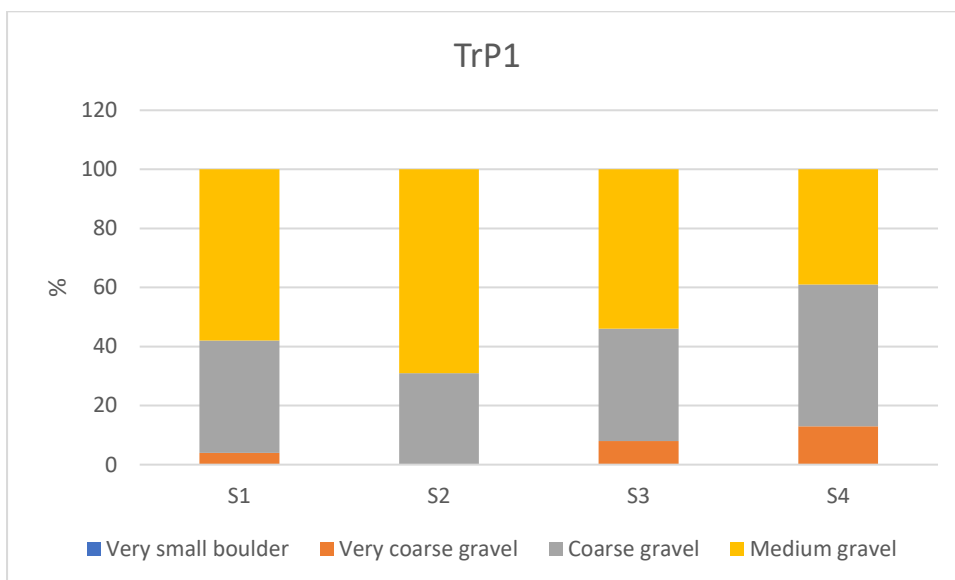


FIGURE 4.6 TRP1 GRAIN-SIZE DISTRIBUTION OF COARSE FRACTIONS.

The presented distribution of the clasts within the gravel size-range in TrP1, show that medium gravel makes up the largest portion among the fractions. In S1, the medium gravel concentration is slightly below 60%, while the largest abundance is found in S2. The occurrence decreases with depth from S2, with the lowest amount found in the deepest section, S4. The amount of clasts comprised of the coarse gravel size-range, show an occurrence of 31-38% between S1-S3, while S4 constitutes of 48%. Very coarse gravel occurred in each section, with the except of S2. In the depths were the fractions were identified, the distribution shows an increase in amount with depth.

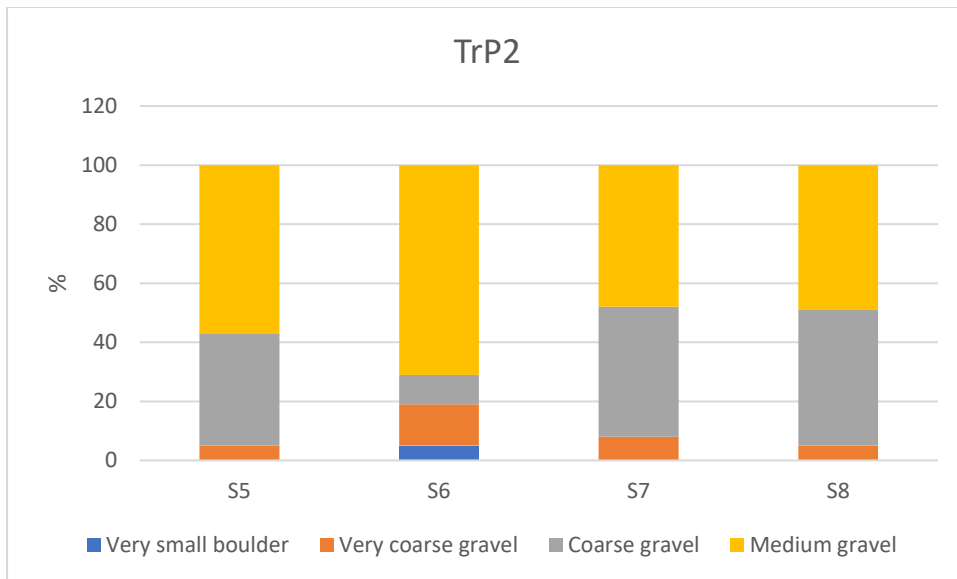


FIGURE 4.7 TRP2 GRAIN-SIZE DISTRIBUTION OF COARSE FRACTIONS

Medium gravel is the most abundant constituent of TrP2, and makes up to over 60% of the coarse fractions in S6. Coarse gravel is present in every section of the pit, but in significantly lower amounts in S6. Among the very coarse gravel, the highest abundance occurs in S6. Very small boulders make up 5% of the fractions in TrP2, occurring only in S2.

The distribution of medium gravel is relatively similar across the pits, and follow a similar pattern with depth. The marked difference in the coarse gravel content occurs in S6, where the amount is significantly lower than at every other depth within both pits. Very coarse gravel is present in every depth, with the exception of S2, and the similar depth in TrP2 (S6), has the largest concentration within this fraction. Very small boulders were found only within the section S6.

4.4 Grain size distribution and mineralogy of fine fractions

In this subchapter the distribution of average grain size, grain size standard deviation, and the mineralogy assigned to the particles by both *Spot Centroid* and *mineral mapping* analyses are presented. The respective analysis modes result in different grain size measurements making a comparative analysis possible.

TABLE 4.2 COMPILATION OF BULK DATA IN TRP1 OBTAINED BY MINERAL MAPPING.

Mineral	Area %				Grain Size (μm)				Grain Size Std Dev (μm)			
	S1	S2	S3	S4	S1	S2	S3	S4	S1	S2	S3	S4
Plagioclase	20,65	19,58	20,50	20,60	8,55	8,45	9,05	8,58	10,89	10,22	11,12	11,03
Titanite	0,21	0,19	0,15	0,17	6,18	6,36	6,41	5,80	4,72	4,82	4,63	4,43
Epidote	1,35	1,68	1,57	1,55	9,36	10,87	9,82	10,12	10,40	10,97	10,96	11,61
Magnetite	0,40	0,41	0,46	0,42	5,28	5,07	5,08	5,35	4,99	5,14	5,00	6,38
Ilmenite	0,22	0,18	0,52	0,30	12,87	13,36	16,31	12,74	13,58	12,44	18,07	13,09
Rutile	0,13	0,09	0,13	0,12	10,02	10,51	10,06	10,75	9,53	7,79	9,41	11,56
Calcite	0,00	0,00	0,01	0,00	3,51	3,00	4,08	3,36	1,59	1,20	2,83	1,50
Zircon	0,11	0,00	0,01	0,02	16,76	5,88	5,82	8,66	22,62	4,47	4,84	8,58
Hematite	0,02	0,02	0,03	0,05	3,91	3,61	4,13	5,09	3,44	2,56	5,10	5,11
Olivine	0,73	0,58	0,57	0,44	5,22	5,04	5,16	4,89	5,92	5,04	5,36	4,74
Almandine	1,56	1,59	1,73	1,73	6,11	5,67	5,82	6,06	7,40	6,81	7,84	7,77
K feldspar	3,74	3,95	3,51	3,60	7,69	7,46	7,47	7,41	9,43	9,22	8,87	9,34
Quartz	23,13	22,45	24,10	24,75	17,81	16,94	18,33	19,59	15,27	14,53	15,66	15,92
Muscovite	2,89	3,03	2,94	2,91	5,60	5,60	5,78	6,04	6,88	6,19	6,71	7,13
Kaolinite	13,82	13,78	12,51	14,62	5,48	5,49	5,40	5,75	5,60	5,74	5,54	5,88
Clinopyroxene (augite)	5,10	6,07	5,79	4,68	10,84	11,53	11,19	10,92	11,50	12,78	11,97	11,82
Amphibole	4,30	4,34	4,30	3,83	5,79	5,73	5,77	5,83	6,62	6,42	6,71	6,78
Biotite	0,92	0,91	1,01	0,90	4,22	4,06	4,37	4,23	4,12	3,39	4,12	4,39
Chlorite (clinocllore)	0,45	0,45	0,36	0,34	4,37	4,52	4,31	4,28	4,34	4,37	4,13	4,03
Chlorite (chamosite)	1,45	1,72	1,51	1,32	5,86	6,24	5,53	5,53	6,77	8,07	6,82	6,41
Apatite	0,00	0,02	0,02	0,00	5,62	7,84	8,88	3,62	2,89	8,01	9,53	2,50

Table 4.2 presents the area (%), average grain size (μm) and grain size standard deviation (μm) measured of the minerals assigned by the mineral mapping-analysis. Quartz represents the largest particles and covers the largest area in each depth. By classification of the average grain sizes into the size range of the silt fractions, 7% are *Coarse silt (16-31 μm)*: Quartz, ilmenite (S3) and zircon (S1). 25% goes into *Medium silt (8-16 μm)*: Plagioclase, augite, epidote, rutile, ilmenite (S1/S2/S4), zircon (S4), apatite (S3). *Fine silt (4-8 μm)* makes up 61% and consists of: Titanite, magnetite, olivine, almandine, K feldspar, muscovite, kaolinite, amphibole, biotite, clinocllore, chamosite, zircon (S2/S3), apatite (S1/S2), hematite (S3/S4) and calcite (S3). *Very fine silt (2-4 μm)* comprehends 7%: calcite (S1/S2/S4), hematite (S1/S2) and apatite (S4).

The zircon found in S1 represents the largest standard deviation from the average grain size. Other stands out are ilmenite (S3), apatite (S2/S3)

TABLE 4.3 COMPILATION OF BULK DATA IN TRP1 BY SPOT CENTROID.

Mineral	Area %				Grain Size (µm)				Grain Size Std Dev (µm)			
	S1	S2	S3	S4	S1	S2	S3	S4	S1	S2	S3	S4
Plagioclase	23,40	23,40	23,34	23,34	22,92	22,34	23,29	22,45	16,89	15,97	17,62	15,51
Titanite	0,13	0,14	0,12	0,09	15,86	15,48	14,88	14,22	10,54	10,55	9,86	9,61
Epidote	1,52	1,52	1,41	1,63	19,63	18,44	18,37	20,98	13,38	12,93	12,40	13,22
Magnetite	0,31	0,30	0,31	0,29	14,70	13,75	13,63	14,77	11,14	9,97	10,25	11,24
Ilmenite	0,24	0,23	0,22	0,29	20,50	20,92	20,48	22,28	14,50	14,03	14,33	15,37
Rutile	0,08	0,08	0,08	0,10	15,93	16,56	15,52	16,94	9,37	11,68	9,90	11,65
Calcite	0,00	0,00	0,00	0,00	14,03	11,45	13,66	13,37	12,23	7,14	8,29	8,01
Zircon	0,03	0,03	0,02	0,02	15,83	16,65	16,47	14,02	13,27	12,51	9,53	8,85
Hematite	0,03	0,03	0,01	0,03	21,36	18,60	15,05	21,32	16,69	13,85	11,89	18,35
Olivine	0,56	0,58	0,59	0,43	20,11	20,09	20,73	20,25	14,89	15,47	16,84	14,12
Almandine	1,71	1,66	1,86	1,51	18,68	17,31	18,67	20,78	13,67	12,19	13,87	13,84
K feldspar	3,27	3,25	3,24	3,21	18,16	17,75	18,40	18,83	13,64	13,09	13,37	13,38
Quartz	30,27	28,52	30,20	33,76	28,23	26,95	28,55	28,19	19,34	18,03	19,93	18,37
Muscovite	3,38	3,78	3,49	3,30	22,09	22,52	22,70	22,58	15,71	15,78	16,32	15,62
Kaolinite	8,88	9,32	8,56	9,48	19,50	18,71	19,64	20,58	14,32	13,63	14,83	14,22
Clinopyroxene (augite)	5,46	5,41	5,68	5,10	17,99	17,57	18,22	19,29	13,75	13,20	14,04	14,09
Amphibole	4,29	4,40	4,40	3,19	17,85	17,22	17,97	19,25	13,07	12,41	13,60	13,36
Biotite	0,93	1,01	0,97	0,66	20,59	20,44	20,49	21,34	14,35	13,96	14,19	13,92
Chlorite (clinocllore)	0,55	0,57	0,52	0,52	23,57	21,97	23,79	22,10	17,69	15,95	18,85	15,88
Chlorite (chamosite)	1,39	1,38	1,32	1,70	24,34	23,66	24,21	25,15	16,97	16,45	16,84	16,69
Apatite	0,01	0,01	0,03	0,02	21,58	14,98	18,26	21,56	14,95	6,86	10,68	17,93

The measurements of the Spot Centroid-analysis (table 4.3) show that quartz stands out compared to the other minerals, in both average grain size and area covered. The lowest average grain size of quartz is measured in S2, while S3 contains the largest measured particles. Calcite, magnetite, and titanite have the lowest average grain size. The average grain size of titanite, magnetite, and calcite in each depth lies within the *medium silt* size range, accompanied by rutile (S1/S3), Zircon (S1/S4) and hematite (S3). The remaining minerals classifies as *coarse silt*. The grain size standard deviation is relatively equal throughout the depths, except from calcite (S1), zircon, and mostly apatite.

The grain size standard deviation shows in general minor differences, with a few exceptions, which have a pronounced deviation. The minerals with the most deviations are zircon, which show a decrease in deviation with depth (from 13,2 - 8,8), apatite ranging from 17,9 to 6,8, and calcite with a range from 12,2 to 7,4.

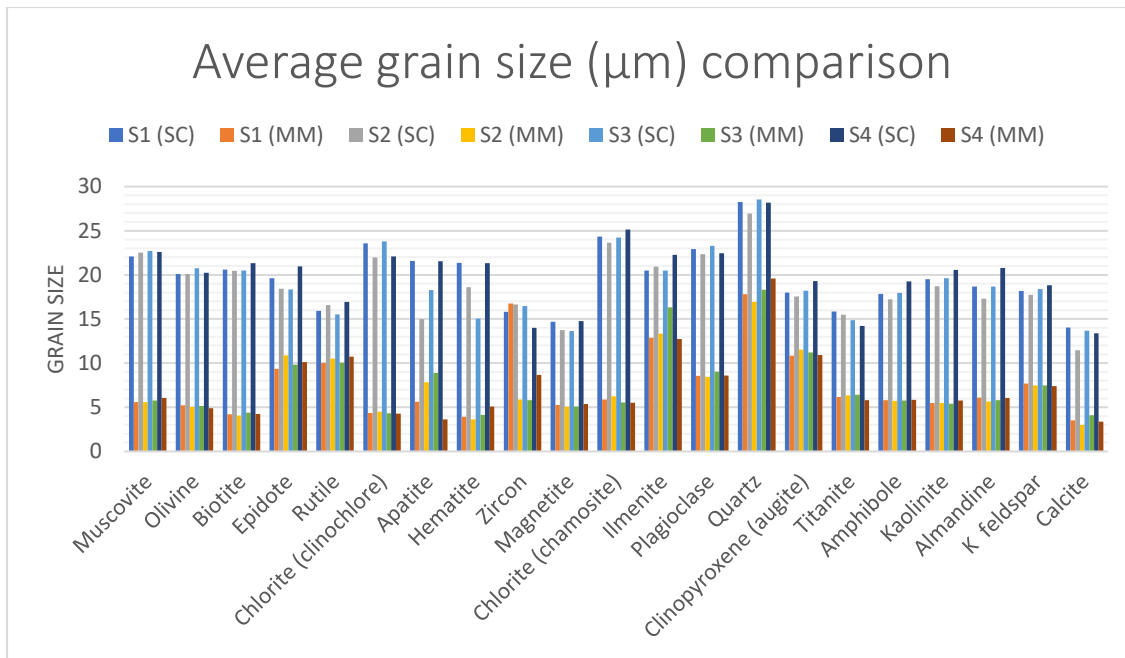


FIGURE 4.8 AVERAGE GRAIN SIZE (μm) COMPARISON OF MEASUREMENTS BY SPOT CENTROID (SC) AND MINERAL MAPPING (MM) IN TRP1.

Fig. 4.8 visualize the average grain size presented in table 2 and 3, in order to get a better impression of the different outcome of the two analyses. The average grain size measurements show in general considerably larger sizes of the particles analyzed by Spot Centroid compared to mineral mapping, expect from zircon in S1. The average grain size of zircon in S1 measured by mineral mapping deviates from the trend, being assigned higher value than the Spot Centroid-analysis. The average grain size of apatite in S4 is measured to be smallest by the mineral mapping-analysis, while Spot Centroid measures it to almost being the largest in the same depth. The quartz particles which holds the largest average grain sizes in each depth, have an average of 27,98 μm in the Spot Centroid-analysis, and 18,16 μm in the mineral mapping. The standard deviation tends to be more equal in the Spot Centroid compared to mineral mapping (table 4.1 and 4.2).

TABLE 4.4 GRAIN-SIZE DISTRIBUTION BASED ON FERET MAX DIAMETER OBTAINED FROM MINERAL MAPPING-ANALYSIS IN TRP1 AND SPOT CENTROID IN TRP1 AND TRP2.

	TrP1				TrP1				TrP2			
	Mineral mapping				Spot Centroid				Spot Centroid			
	Ferret max diameter (%)				Ferret max diameter (%)				Ferret max diameter (%)			
Grain fractions	S1	S2	S3	S4	S1	S2	S3	S4	S5	S6	S7	S8
Very fine sand	2,08	1,64	2,16	2,45	2,69	2,19	2,99	2,52	2,08	2,29	2,49	2,17
Very coarse silt	16,30	14,43	16,36	18,12	16,40	15,59	16,56	17,81	18,00	18,20	17,85	17,20
Coarse silt	33,07	32,45	32,85	33,72	28,68	28,81	28,01	31,30	32,41	32,09	31,59	31,74
Medium silt	42,29	44,77	42,39	39,93	36,10	37,29	35,44	34,67	33,70	33,01	32,77	33,69
Fine silt	6,25	6,70	6,23	5,78	10,76	11,53	11,50	8,21	7,98	8,22	8,07	8,41
Very fine silt					2,37	1,98	2,34	2,45	2,58	2,86	2,86	2,76
Clay					3,00	2,60	3,16	3,03	3,25	3,33	4,36	4,04

Table 4.4 shows that the mineral mapping-analysis for TrP1 only provides occurrence of grains in the range from fine silt (4-8 µm) to very fine sand (63-125 µm). The coarsest fraction, very fine sand, has a similar prevalence in the depths at ~2%. There is a marked mode within medium silt (8-16 µm), which accounts for almost 40% in each depth. Coarse silt (16-31 µm) ranges from ~32 - ~34%, while very coarse silt has a slightly more uneven distribution, ranging from ~14% in S2 to ~18% in S4. The fine silt fractions make up ~6 - ~7% of each depth.

The Spot Centroid-analysis for TrP1 and TrP2 embraces a larger grain size range, which includes very fine silt (2-4) and clay fractions (<2 µm). The order of the distribution is similar to the mineral mapping-analysis, with highest percentages in medium silt, followed by coarse silt and very coarse silt (31-63 µm).

TABLE 4.5 GRAIN-SIZE DISTRIBUTION OF QUARTZ BASED ON FERET MAX DIAMETER OBTAINED FROM BOTH ANALYSES IN TRP1.

	Quartz TrP1								
	Mineral mapping				Spot Centroid				
	Ferret max diameter (%)				Ferret max diameter (%)				
Grain fractions	S1	S2	S3	S4	S1	S2	S3	S4	
Very fine sand		4,27	3,10	4,16	5,08	6,43	4,75	6,94	5,85
Very coarse silt		25,67	22,12	25,19	29,02	28,99	28,50	28,96	30,10
Coarse silt		34,17	34,71	33,75	35,07	33,12	34,08	32,47	33,93
Medium silt		31,15	34,13	31,77	26,11	26,05	26,69	25,93	25,96
Fine silt		4,74	5,94	5,13	4,73	5,40	5,99	5,69	4,15

Table 4.5 shows the grain-size distribution of quartz based on the feret max diameter measurements by both Spot Centroid and mineral mapping in TrP1. Both analyses show a low occurrence of very fine sand and fine silt, while very coarse silt, coarse silt and medium silt makes up the largest concentrations. Coarse silt comprises the largest amount in each depth in regard to both analyses.

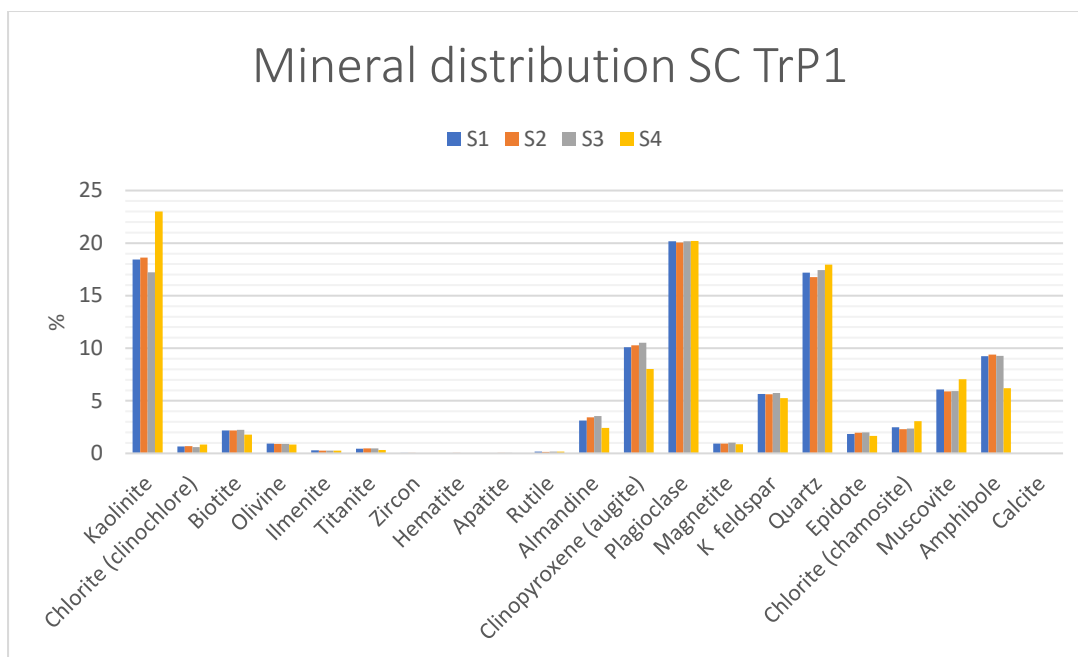


FIGURE 4.9 MINERAL DISTRIBUTION BY SPOT CENTROID IN TRP1.

The modal mineralogy conducted by Spot Centroid in TrP1 shows plagioclase, kaolinite and quartz to be most abundant throughout the pit. The plagioclase occurs at a steady rate of ~20% in each section. Kaolinite has the richest measured occurrence of a single mineral, with a peak exceeding 23%, which is found in S4. The mean content of the kaolinite identified in TrP1 is approximately 19.3%. Quartz has a consistent occurrence of ~17% at each depth. Augite and amphibole have relatively similar tendencies in their distributions, with the lowest amount occurring in S4. Muscovite content peaks in S4 with a total of 7%, compared to a range between 5-6% in the overlaying sections. Zircon, hematite, apatite and calcite have the lowest prevalence in each section, ranging from ~0,01 to 0,06%. Rutile has a slightly higher occurrence within the range of 0,1 to 0,2%.

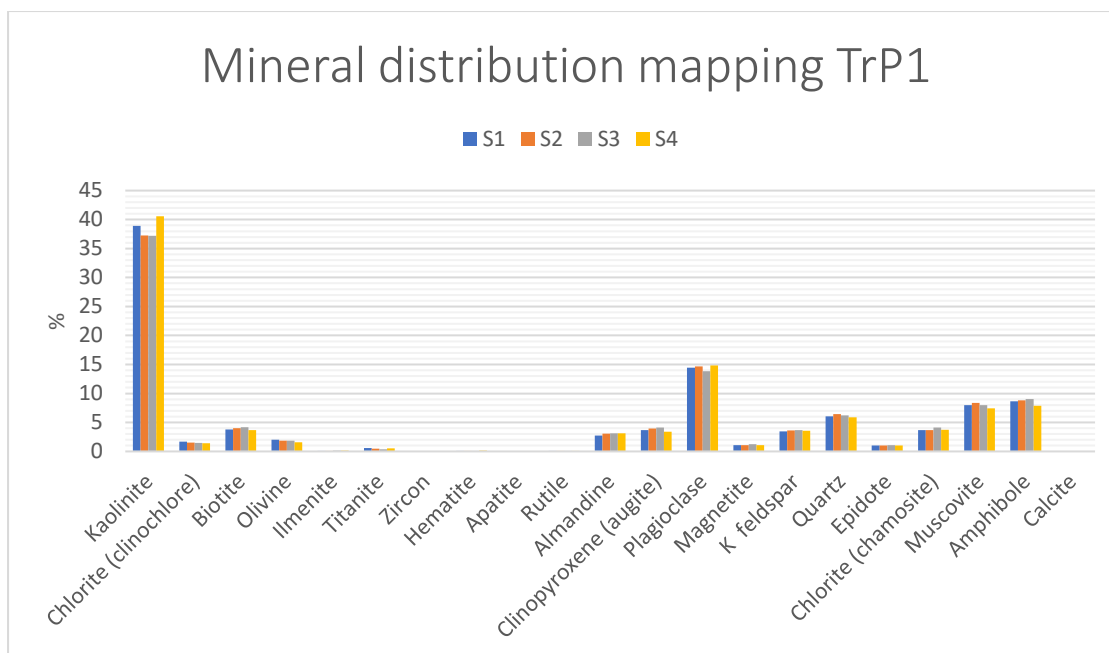


FIGURE 4.10 MINERAL DISTRIBUTION BY MINERAL MAPPING IN TRP1.

According to the mineral mapping analysis the occurrence of kaolinite in TrP1 is even higher, with at least 37% in every section. The most distinct presence of kaolinite is in S4 exceeding 40%, which is much higher than according to the SC analysis. Plagioclase features second in abundance, which amounts to ~15% in S2/S4 and ~14% in S3. Amphibole and muscovite lie within 7-9% each. Quartz has a stable vertical extent of ~6% in all depths of TrP1. The distribution of K feldspar, biotite, augite and chamosite have similar tendencies. Olivine is present by an occurrence of slightly below 2%. The lowest occurrence is observed for the minerals; zircon, apatite, rutile and calcite, separately making up <0,1% of the total. Hematite has a slightly higher occurrence ranging from ~0,1 to ~0,2%.

4.4.1 Comparison of mineral distribution in TrP1 by Spot Centroid and mineral mapping

The differences between the analyses are considerable. The kaolinite occurrence varies from 17-23% in the SC-analysis, while 37-40% are identified by the mapping analysis. Both analyses indicate highest occurrence of kaolinite in S4, while the other depths differentiate. Plagioclase has a similar prevalence according to both analyses, but the total percentage identified is ~5% lower in the mapping than in SC. The amount of identified quartz shows a ~10% gap in favor of SC. SC-analysis shows an occurrence of 8-11%, only 3-4% are identified by mapping. The remaining minerals have a deviation of less than 2% between the two analyses.

4.5 Grain morphology of fine fractions

The morphometrics assigned to each particle by the analysis modes Spot Centroid and Mineral mapping are presented to gain information about grain-size and morphology. The compactness values indicative of sphericity is derived from the perimeter and area parameters.

TABLE 4.6 COMPACTNESS (%) MEASUREMENTS OBTAINED FROM MINERAL MAPPING-ANALYSIS IN TRP1 AND SPOT CENTROID IN TRP1 AND TRP2.

	TrP1				TrP1				TrP2			
	Mineral mapping				Spot Centroid				Spot Centroid			
	Compactness(%)				Compactness(%)				Compactness(%)			
Value	S1	S2	S3	S4	S1	S2	S3	S4	S5	S6	S7	S8
1-1,5	16,570	18,135	16,823	19,886	25,008	27,363	27,424	15,423	14,778	14,714	7,831	6,973
1,5-2	25,727	26,934	25,517	28,177	23,467	24,381	24,158	19,256	18,783	19,255	11,604	10,138
2-2,5	16,824	16,024	16,777	16,739	13,601	13,751	13,560	12,445	12,432	12,589	10,888	10,198
2,5-3	11,492	11,541	11,483	11,049	8,514	8,322	8,339	8,592	8,868	8,956	9,174	9,127
3-3,5	7,849	7,616	7,751	7,183	5,682	5,327	5,406	6,337	6,478	6,607	7,679	7,969
3,5-4	5,837	5,525	5,706	4,739	4,062	3,824	3,815	4,936	4,992	5,047	6,411	6,889
4-4,5	3,952	3,748	3,884	3,395	2,969	2,730	2,692	3,875	4,031	3,998	5,229	5,752
4,5-5	2,939	2,507	2,899	2,378	2,296	2,073	2,100	3,188	3,171	3,150	4,484	4,834
5-10	7,826	7,079	8,117	5,799	9,282	8,153	8,308	14,646	15,037	14,442	21,893	23,683
10-15	0,754	0,636	0,833	0,532	2,761	2,295	2,301	5,135	5,142	4,979	7,077	7,425
15-20	0,132	0,151	0,160	0,087	1,169	0,959	0,966	2,481	2,520	2,423	3,121	3,066
20-50	0,100	0,099	0,050	0,035	1,146	0,789	0,907	3,387	3,468	3,515	4,093	3,537
50-100		0,005			0,040	0,029	0,023	0,288	0,285	0,311	0,481	0,374
100-200					0,003	0,003	0,001	0,012	0,013	0,013	0,035	0,033
200-300									0,001		0,001	0,001
>300											0,0003	0,0003

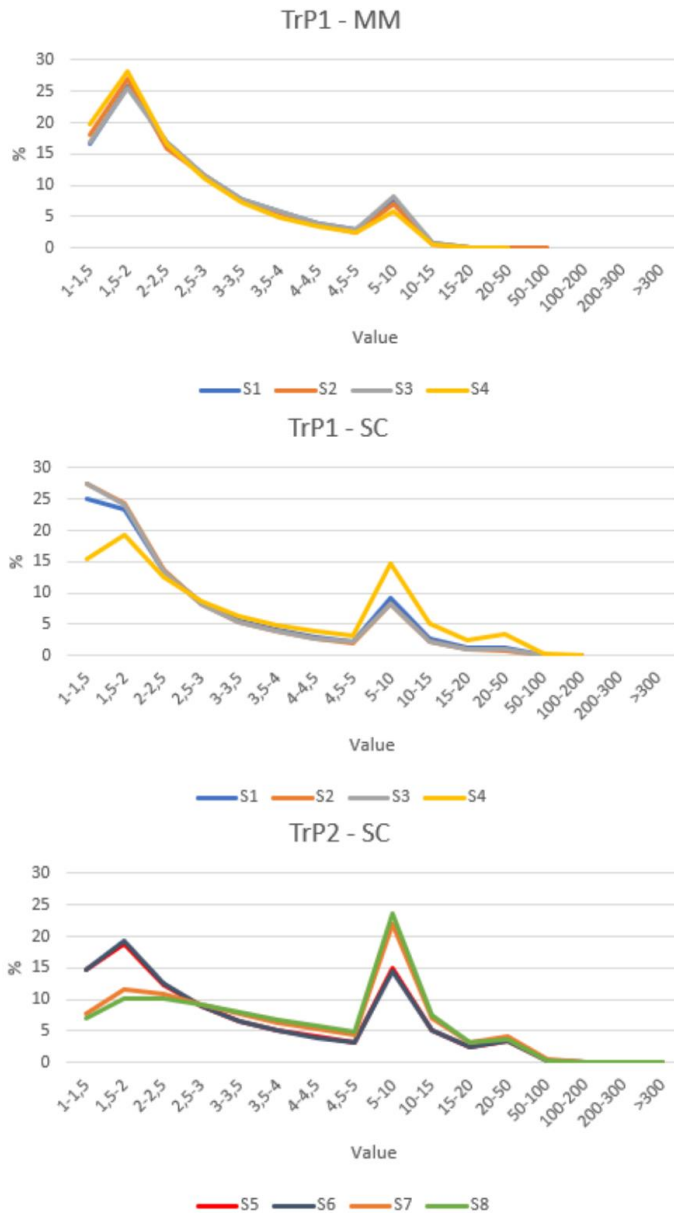


FIGURE 4.11 DISTRIBUTION OF THE TOTAL PARTICLE COMPACTNESS OBTAINED FROM BOTH ANALYSES IN TRP1 AND FROM THE SC-ANALYSIS FOR TRP2.

The results derived from the mineral mapping of TrP1 and Spot Centroid-analysis of the total particles in TrP1 and TrP2, shown in table 4.1 and fig. 4.10, contain the compactness values and distribution within each depth. The compactness value of 1 is the minimum value and it indicates that the particle has the shape of a circular blob, while higher values indicate an increase of convoluted shapes. The compactness values are classified into narrow ranges among the lowest values, with regard to the aim of identifying in-situ or foreign origin of the particles, while broader ranges apply for the high value particles.

4.5.1 Comparison of compactness measurements between both analyses within TrP1

The respective analyses provide results that differs from one another. The Spot Centroid-analysis implies in general that the highest concentration of particles occurs in the lowest value range, while the mineral mapping-analysis concludes with highest occurrence within the adjacent value range. Within the second lowest value range (1,5-2), Spot Centroid measures the lowest concentration among the depths in S4, while mineral mapping shows highest occurrence in S4. The mineral mapping-analysis shows an even distribution, with just minor differences between the depths, while the SC-analysis shows S4 to deviate markedly from the other depths.

The measurements derived from the Spot Centroid-analysis of TrP1 shows that the lowest value range comprises the highest percentages in S1, S2 and S3, while S4 has the highest concentration within the second lowest range. The lowest value range within S4 show a significant decrease compared to the similar range within the other depths.

4.5.2 Comparison of Spot Centroid compactness measurements between TrP1 and TrP2

The resulting compactness measurements show a significant difference between the pits. Table 4.4 shows a larger concentration of particles within the three lowest compactness value ranges in TrP1 compared to TrP2. Within the lowest range (1-1,5), TrP1 has a minimum of 10% higher occurrence at the depths of 20-30 cm and 40-50 cm, than the measured amount in TrP2. Within the depths of 60-70 cm (S3/S7), TrP1 has ~20% larger concentration than TrP2. The deepest depth ranges from 80-90 cm (S4/S8), show that TrP2 has a concentration of only ~7%, compared to 15% in TrP1. Values exceeding 2,5 shows that TrP2 has the largest concentrations throughout the depths, including values exceeding the whole range of TrP1.

4.5.3 Grain morphology of quartz and plagioclase

The morphology of the quartz and plagioclase minerals are presented in order to compare the commonly occurring gabbro mineral plagioclase to the more uncommon mineral, quartz.

TABLE 4.7 COMPACTNESS (%) OF QUARTZ IN TRP1 OBTAINED FROM BOTH ANALYSES.

Quartz TrP1									
	Mineral mapping					Spot Centroid			
	Compactness (%)					Compactness(%)			
Value	S1	S2	S3	S4		S1	S2	S3	S4
1-1,5	23,144	25,959	23,123	28,808		41,625	44,491	42,764	27,045
1,5-2	32,089	34,157	32,575	32,684		28,079	27,093	26,938	32,994
2-2,5	15,474	14,188	16,029	14,135		11,895	11,221	11,993	15,023
2,5-3	9,794	9,301	9,679	8,497		6,152	6,291	6,371	7,952
3-3,5	5,456	5,439	5,646	4,808		3,853	3,434	3,680	5,005
3,5-4	4,025	3,521	3,826	3,067		2,432	2,236	2,415	3,388
4-4,5	2,683	2,128	2,316	2,342		1,605	1,367	1,678	2,166
4,5-5	1,699	1,051	1,717	1,492		1,081	0,944	1,205	1,551
5-10	5,076	3,573	4,405	3,689		2,924	2,614	2,696	4,161
10-15	0,335	0,447	0,476	0,373		0,322	0,244	0,247	0,553
15-20	0,089	0,184	0,186	0,083		0,023	0,055	0,009	0,112
20-50	0,134	0,053	0,021	0,021		0,009	0,010	0,004	0,050

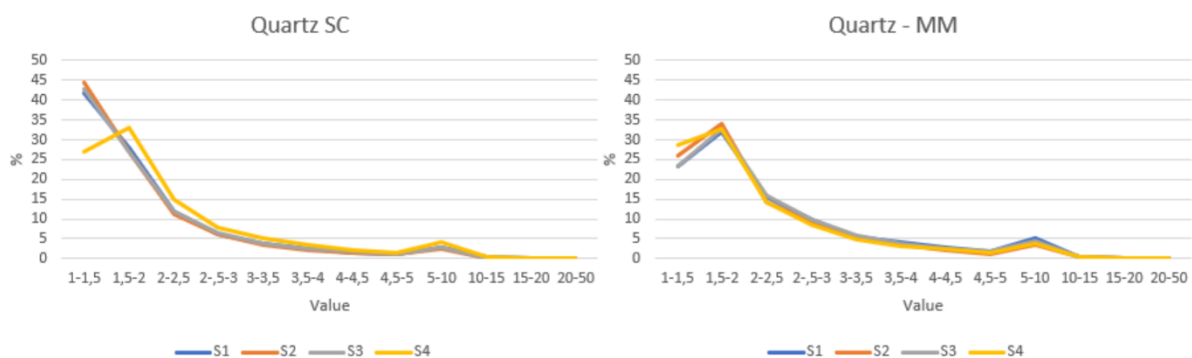


FIGURE 4.12 DISTRIBUTION OF QUARTZ COMPACTNESS IN TRP1 OBTAINED FROM SPOT CENTROID (SC) AND MINERAL MAPPING (MM).

The compactness of quartz ranges from ranges from 23-28% within the lowest value range, comprising the second highest concentration. The highest percentages are assigned to the particles with a compactness within the 1,5 to 2 value range, which comprises ~32- ~34% of the total quartz particles within each depth.

The quartz measured through Spot Centroid show a high concentration (~42 - ~44%) within the lowest value range at the three upper depths, while S4 records for a significant decrease, containing only 27%. The compactness measurements of the lower value ranges in S4 deviates from the overlying depths, which have an even distribution.

TABLE 4.8 COMPACTNESS (%) OF PLAGIOCLASE IN TRP1 OBTAINED FROM BOTH ANALYSES.

Plagioclase TrP1									
	Mineral mapping					Spot Centroid			
	Compactness(%)					Compactness(%)			
Value	S1	S2	S3	S4		S1	S2	S3	S4
1-1,5	18,360	21,376	18,578	22,267		38,356	42,107	41,029	20,572
1,5-2	27,127	28,329	27,687	28,833		26,490	26,133	25,674	25,522
2-2,5	15,983	14,939	16,016	15,812		12,525	12,176	11,925	15,022
2,5-3	10,516	10,466	10,235	10,173		7,161	6,715	6,911	10,064
3-3,5	7,007	6,776	6,452	6,242		4,448	3,837	4,360	6,788
3,5-4	5,172	4,798	5,028	4,333		3,000	2,604	2,831	4,982
4-4,5	3,620	3,277	3,268	3,004		2,041	1,670	1,762	3,593
4,5-5	2,524	2,022	2,765	2,222		1,431	1,199	1,420	2,743
5-10	7,795	6,732	8,547	6,097		3,900	3,225	3,675	8,638
10-15	1,096	0,841	1,029	0,804		0,519	0,274	0,362	1,409
15-20	0,259	0,221	0,311	0,134		0,108	0,051	0,043	0,421
20-50	0,172	0,221	0,084	0,078		0,021	0,009	0,008	0,234
50-100									0,012

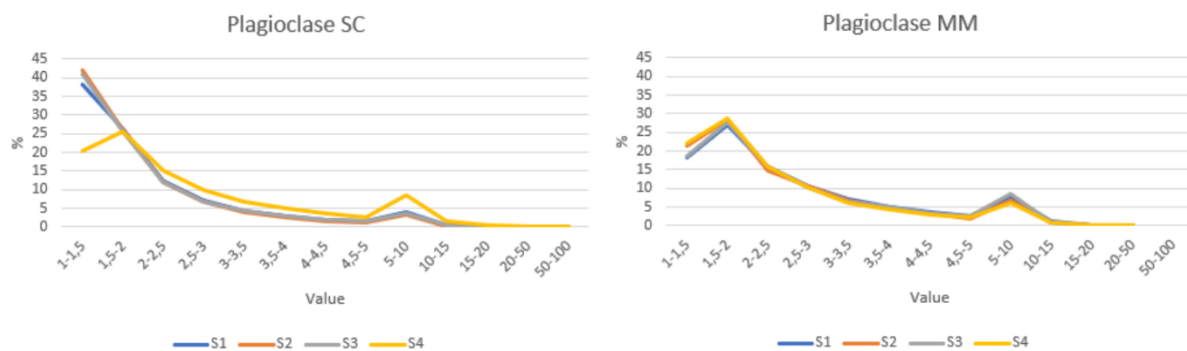


FIGURE 4.13 DISTRIBUTION OF PLAGIOCLASE COMPACTNESS OBTAINED FROM BOTH ANALYSES.

The mineral mapping-analysis shows minor differences between the depths in the lowest value range, while the remaining value ranges show similar distribution between the depths. The highest concentration is located within the 1,5 to 2 value range, encapsulating ~27-~29% of the total plagioclase particles in each depth.

The Spot Centroid-analysis provide measurements where the distribution in S4 deviates from the other depths. The largest concentrations of plagioclase particles within the lowest value range, indicative of high sphericity. The distribution of the most compact particles within the lowest value range, show that the middle depths in the column contains the largest concentration, while the deepest section of TrP1 contains the least amount. S4 accounts for approximately 20% less than S2 and S3.

4.5.4 Comparison of quartz and plagioclase compactness

The Spot Centroid-analysis assigns compactness values within the lowest value range (1-1,5) to at least 40% of the quartz in S1/S2/S3, while S4 contains 27%. A similar pattern is recorded for among the plagioclase, where S1-S3 consists of 38-42% and S4 has 20%. Both minerals have the largest concentration within S2, followed by S3, S1 and S4 in that order.

The data provided from the mineral mapping-analysis shows that quartz and plagioclase have both the largest concentrations within the second lowest range of compactness values (1,5-2). Quartz compactness occurs from 32-34%, while plagioclase range from 27-29% within the value range. The next largest concentration takes place within the lowest value range of 1-1,5 for both minerals, with quartz exceeding plagioclase again.

4.5.5 SEM

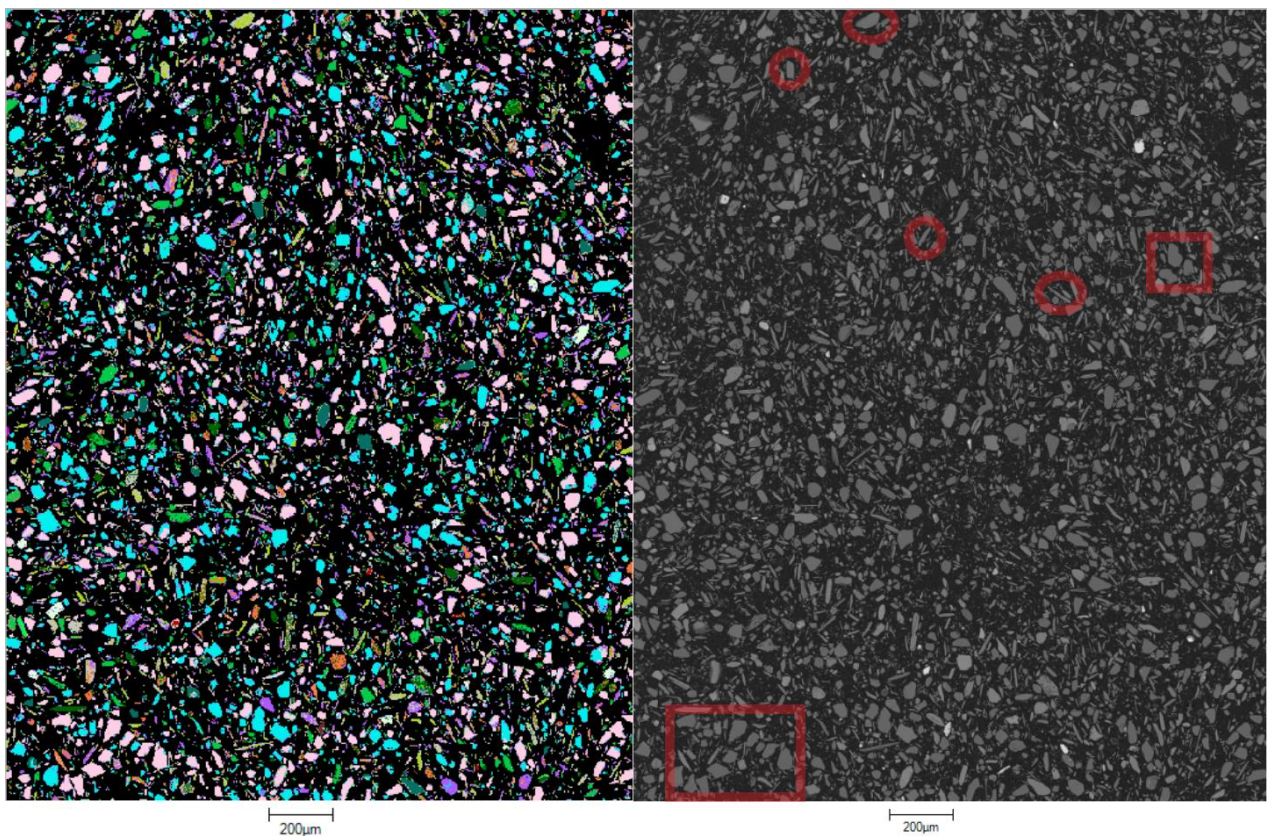


FIGURE 4.14 FALSE-COLOR IMAGE AND BACKSCATTERED ELECTRON IMAGE (BSE) AT 20-30 CM DEPTH (S1) IN TRP1. THE SQUARES ENCAPSULATE EXAMPLES OF BLOCKY QUARTZ, AND THE CIRCLES SHOW MUSCOVITE. FULL IMAGES OF EACH DEPTH CAN BE FOUND IN THE APPENDIX.

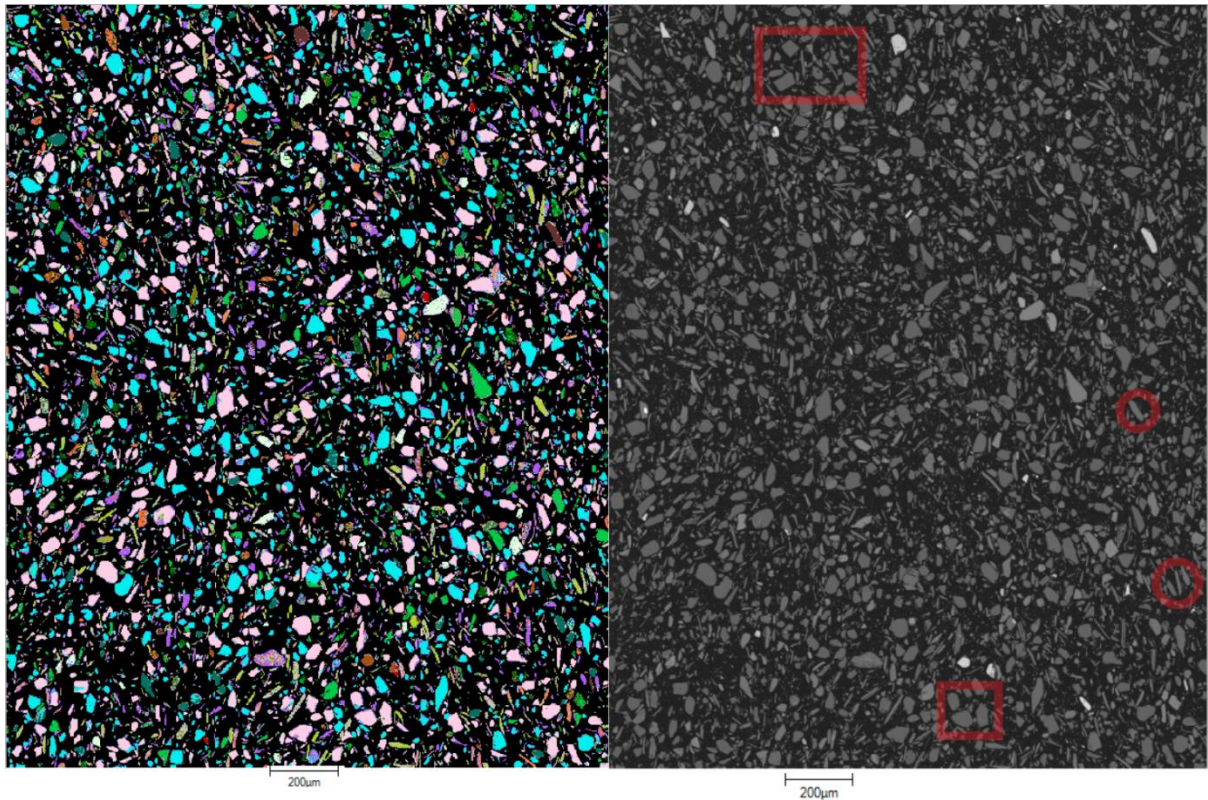


FIGURE 4.15 FALSE-COLOR IMAGE AND BACKSCATTERED ELECTRON IMAGE (BSE) AT 80-90 CM DEPTH (S4) IN TRP1. THE SQUARES ENCAPSULATE EXAMPLES OF BLOCKY QUARTZ, AND THE CIRCLES SHOW MUSCOVITE.

Almandine	Biotite	Chlorite (clinochlore)	Hematite	Kaolinite	Olivine	Rutile	Not Classified Unclassified
Amphibole	Calcite	Clinopyroxene (augite)	Ilmenite	Magnetite	Plagioclase	Titanite	
Apatite	Chlorite (chamosite)	Epidote	K feldspar	Muscovite	Quartz	Zircon	

5 Discussion

In this chapter the data presented in chapter 4 will be compiled and discussed. The morphology parameters and mineralogy assigned by the analyses will be interpreted and correlated to available literature, in order to investigate if aeolian transported silt have contributed to the stratigraphic composition of the blockfield. The question, if loess can be distinguished from in-situ weathered silt will be attempted to answer here.

5.1 Grain morphology and size of the loess-sized particles

According to Pye (1984), the silt grains found in loess tends to mostly be blocky and angular or subangular, while Liu et al. (2016) found the silt grains in loess deposits in China to be square-like and subangular or subrounded with image analysis. Rogers and Smalley (1993) observed that loess particles tend to majorly be of blade shapes (72%), followed by disc/rod shapes (27%), and minor occurrence of spherical shapes (1%) with the Monte Carlo method, and similar results were reported from a reproducing attempt by Howarth (2010).

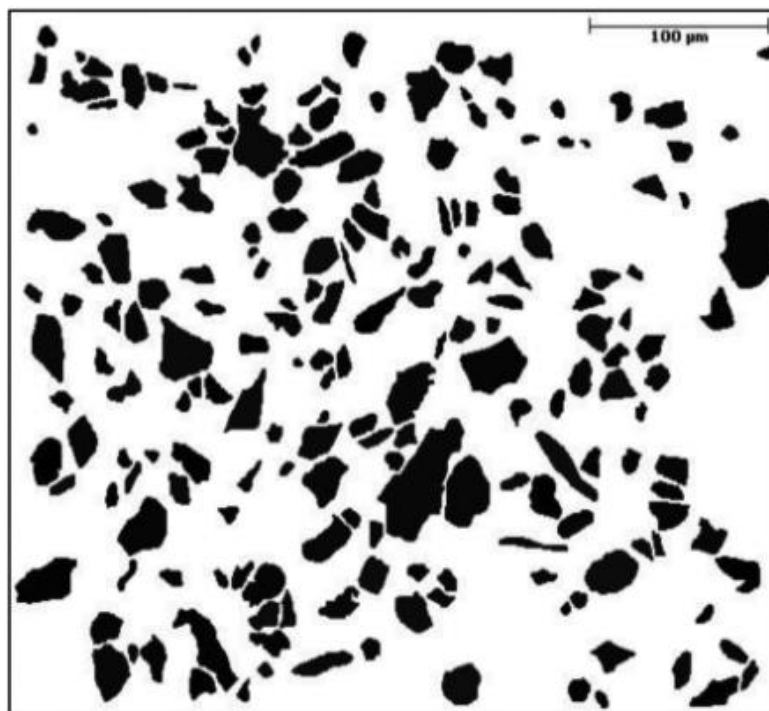


FIGURE 5.1 SEM MICROGRAPH OF LOESS IN CHINA (LIU ET AL., 2016)

Liu et al. (2016) found the loess particles in China (fig. 5.1) constituting quartz, muscovite, albite and calcite, to mostly have the form of a square, while being angular to subangular.

The selected sections of silt-sized particles visualized in fig. 4.14 and 4.15, contain a variety of grain shapes. The quartz grains are majorly blocky and angular or subangular, which correlates to the descriptions given by Pye (1984). There is also occurrence of quartz that clearly show edge-rounding. Fig. 5.2 is a magnified image of the framed quartz silt in fig. 4.14 and 4.15, and presents examples from 20-30 cm depth (S1) and 80-90 cm depth (S4) in TrP1. The shape of the quartz silt shows similar shape characteristics to the 2D-image from China (fig. 5.1) and the stated characteristics by Pye (1984), with square-like shapes and angular, subangular to subrounded corners.

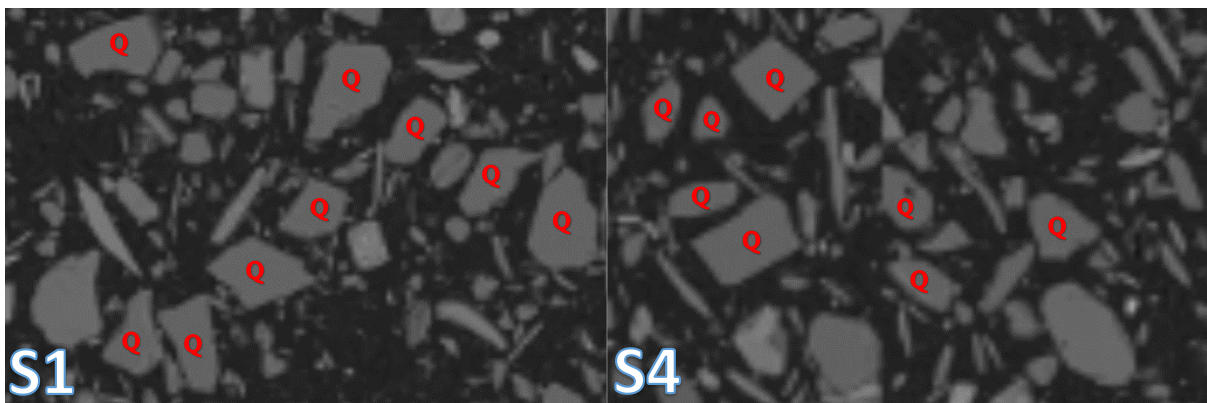


FIGURE 5.2 MAGNIFIED BACKSCATTERED-ELECTRON IMAGE (BSE) OF SQUARES CONTAINING QUARTZ (Q) IN FIG. 4.14 AND FIG. 4.15. S1 (20-30CM) AND S4 (80-90 CM)

The muscovite found in fig 4.14 and 4.15 have in general elongated shapes, which also is the case in the Chinese loess (Liu et al., 2016). In fig 5.3 a selection of muscovite from the uppermost and the lowermost depth in TrP1 are magnified, and shows the most prevalent thin, narrow-shaped particles.

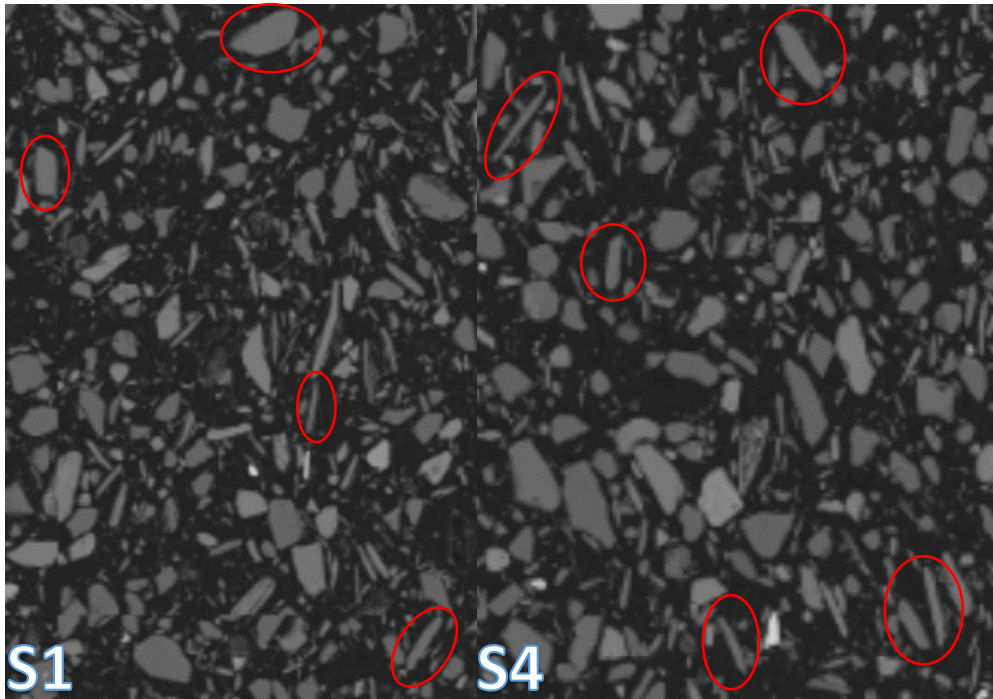


FIGURE 5.3 MAGNIFIED BACKSCATTERED-ELECTRON IMAGE (BSE) OF THE MUSCOVITE PRESENTED IN FIG. 4.13 AND 4.14. S1 (20-30 CM) AND S4 (80-90 CM).

Taking the compactness measurements into account (fig. 4.11, table, 4.6), the majority of the particles seems to have a blocky, square-like shape, which correlates with the 2D-images provide by the analyses. These characteristics show similarities to the observations of Pye (1984), Rogers and Smalley (1993) and Liu et al. (2016). The compactness values obtained from the mineral mapping-analysis show no tendencies of marked variations between depths in TrP1 or among the quartz and plagioclase in the same pit, which points to similar prevalence within the column.

According to Pye (2015), the mode in the grain-size distribution of loess in continental loess deposits lies within the range of 10-50 μm , and $<10 \mu\text{m}$ for ocean deposited long distance transported particles. Liu et al. (2016) identified the median particle size to be 12 μm from the Loess plateau in China. Using the feret max diameter measurements from the mineral mapping-analysis as indicator of grain size, 16-19% of the silt-sized particles in TrP1 are smaller than 10 μm , while ~77-78% fall within the range of 10-50 μm range. The Spot Centroid-analysis of the depth sections in TrP1 shows a range from ~66-71% within 10-50 μm , and ~23-28% smaller than 10 μm . Wright et al. (1998) considered loess to be predominantly quartz particles within the 20-60 μm size range. The feret max diameter of the quartz obtained from the Spot Centroid-analysis, shows that approximately 50% of the content at each depth in TrP1 fall into

the 20-60 μm range stated by Wright et al. (1998), while the mineral mapping-analysis provide a distribution from 43-51% within the same size range.

5.2 Mineralogy of the loess-sized particles

The analyses of the loess fraction (2-63 μm) identifies the presence of 21 minerals in the depth sections extracted from TrP1. Fig. 4.9 and 4.10, show that quartz, plagioclase and kaolinite are the most abundant minerals. The characteristic gabbroic minerals; augite, olivine, and plagioclase feldspar identified from the Lyngen gabbro (Whalley et al., 2004), and the mineral composition of the Pee Dee gabbro, southern USA of plagioclase (41%), biotite (10%), augite (14%), magnetite (9%) and ilmenite (4%) (Fritz, 1988), are all present in the samples from Tron. The identified mineralogy (subchapter 4.4) correlates well with the findings of Wellings (1996). Wellings identified plagioclase, orthopyroxene, clinopyroxene and olivine on the summit plateau, while amphibole, plagioclase, serpentine and white mica was mapped on the northeast slope. Except for orthopyroxene and serpentine, the same minerals were identified through both analyses. The resulting modal mineralogy of the mineral mapping (fig. 4.10) shows kaolinite to be the most abundant mineral by a large margin at every depth, while the Spot Centroid-analysis (fig. 4.9) identify a smaller amount. Both analyses conclude with the largest concentration at the depth of 80-90 cm. The presence of kaolinite, along with other secondary minerals, has been interpreted as an indication of weathering during Neogene climate conditions (Rea et al., 1996), whereas Goodfellow (2012) shows that secondary minerals may form during periglacial conditions. The presence of kaolinite indicates advanced chemical weathering (Goodfellow, 2012). Kaolinite is a product of weathering or alteration of aluminosilicate mineral, and mainly muscovite and plagioclase (Haberlah et al., 2011). Kaolinite has also been reported from the summit by Strømsøe and Paasche (2011), and could not be excluded with certainty from chlorite in the XRF-analysis by Halleraker (2011).

Quartz is a prevalent mineral on the Tron summit according to the Spot Centroid-analysis (fig. 4.9), where it makes up approximately 17% at each sampled depth in TrP1. The quartz abundance identified through the mineral mapping-analysis shows a mean content of 6% at each depth, which contradicts with the findings of the Spot Centroid-analysis. The geological mapping by Wellings (1996) did not reveal occurrence of quartz above 1200 m.a.s.l on the massif, but the mineral proved to be prevalent beneath that height. Quartz is not expected to occur in such rates in gabbro lithology, which may indicate foreign contamination. Possible contribution to the quartz content in the blockfield sediment could stem from weathered

erratics, which subsequently was inherited to the soil by sedimentological mixing. Occurrence of erratics has been reported on Tron by both Engelién (1995) and Halleraker (2011), where the latter observed quartz-rich glacial erratics located on the tors. Other possible explanation may be an aeolian influx. Quartz is usually the dominant constituent in most loess deposits, making up 45-55% of the content (Pye, 1995). Quartz are also reported from lithologies elsewhere that it is not expected. The findings of quartz and muscovite in the Duoštečohkka amphibole, northern Sweden are considered to be of aeolian origin and/or from tills (Goodfellow et al., 2014). Tills are mapped up to 1400 m.a.s.l on Tron (Thoresen and Follestad, 1999), which may be a potential source for the occurrence of quartz and muscovite on the summit. In the Lyngen gabbro, northern Norway, quartz veins were identified by Munday (1974), such veins are not observed on Tron (Halleraker, 2011). The mineralogy identified from the sediments sampled in TrP1 show similarities to the mineralogy of the loess deposits in eastern Europe (Újvári et al., 2010), and the Loess plateau in China (Liu et al., 2016).

5.2.1 Potential time of deposition

If loess is present on Tron, it would probably have its origin from the glacial periods during Quaternary, which are recognized to be characterized by lots of glacial, tectonic, and wind activity (French, 2007; Haase et al., 2007; Muhs, 2013). Dust deposition occurred on a higher rate during glacial periods (Mahowald et al. 1999). The plausible source for the potential occurrence of loess may be seen in context with the dust transport simulation of Schaffernicht et al. (2020), where dust deposition in Denmark, southern Sweden and the North Sea basin stemmed from the areas around west-Poland, east-Germany and Czechia. Dahl et al. (1997) implied that the wind directions were predominant from north-northeast and south-southwest during Late Weichselian. Dahl et al. (1997) proposed that Tron protruded as a nunatak during the Late Weichselian, If Tron summit avoided glacial cover during the windy conditions in Quaternary, the blockfields would function as an efficient dust entrapment mechanism due to its rough topography. Mangerud (2004) implies Tron was glaciated during the last glaciation, which means that the loess particles could have been deposited temporarily on the glacier surface, before being deposited on the mountain during glacial retreat or by meltwater drainage. The particles would then be mixed into the sediment stratigraphy during freeze and thaw processes.

5.2.2 Comparison of Spot Centroid and mineral mapping-analyses

The results from the Spot Centroid and mineral mapping-analyses show significant differences in regard to distribution of minerals, average grain size of minerals and the total particles analyzed. The differences in average grain size (fig. 4.8), show a general trend of larger sizes measured through the Spot Centroid-analysis. The only exception occurs in the zircon measurement in S1, where the mineral mapping-analysis assigns the largest grain size. The Spot Centroid-analysis calculates the geometric centre of the grains, and assigns a composition based on one analysis spot (Graham et al., 2015). This may be the factor explaining the larger grain sizes measured by this analysis compared to the mineral mapping-analysis, and that mineral mapping is the best suited approach for the loess fraction.

The compactness values measured by the Spot Centroid-analysis show that S4 deviates markedly within the lowest value range in TrP1, and for both the plagioclase and quartz. The Spot Centroid-analysis of TrP2 also show marked deviations between the depths, but in this case the two lowermost depths deviate from the upper two. The mineral mapping-analysis show a fairly similar distribution of the same particles, which could mean that the Spot Centroid-analysis overestimates the grain sizes and that mineral mapping-analysis is the most trustworthy in this context.

5.2.3 Potential error sources through SEM method/preparations

During preparations for the SEM-analysis, the orientation of the grains mixed in the graphite may result in such a way that the largest particle surfaces not necessarily are visible, which could affect the morphological and grain-size measurements. Using graphite as filler does not necessarily prevent particle segregation (Røisi and Aasly, 2018), which could lead to touching particles, and could subsequently have affected the grain-size measurements. The input of a mineral recipe, which makes the premise for the minerals assigned to the particles, could affect the results. Each depth contains unclassified minerals, which could mean that there is occurrence of minerals in the pits that were not identified and/or that the chemical composition of minerals in the recipe had some missing components.

5.3 Origin of clasts and the loess-sized fractions

The Last Glacial Maximum (LGM), which is considered to comprise the largest ice volume during the last glacial cycle, was characterized by very cold conditions with annual global mean temperatures 1.85-9.17°C lower than the present (Strandberg et al., 2010). The modelled ground temperatures on Tron shows an increase of +0.1°C to +0.7°C at 10m depth, and +0.1°C

to +0.4°C at 100m depth in the period 1860-2009 (Hipp et al., 2011). Permafrost has been a permanent fixture on Tron until recently, where there are signs of permafrost degradation and talik development (Hipp et al., 2011; Westermann et al., 2013).

Gravel-sized clasts occur at every sampled depth in both pits, and tend to be a product of macrogelivation (Ollier, 1984; Matsuoka, 2001a). The majority of the clasts (fig.4.4, 4.5) show characteristics of being equant, which tend to be favorable for weathered gabbro (Benn, 2004). Gabbro is by far the most abundant rock type in every transect and depth in both pits, which correlates with the lithology of Tron massif (Wellings, 1995; Ramsey and Siedlecka, 2001). Gabbro is a high porosity rock type that is acknowledged to be more vulnerable to weathering (Matsuoka, 2001). Ice segregation is acknowledged to be an important factor in fracturing of moist, fine-grained porous rocks in periglacial and permafrost environments (Murton, 2007; Matsuoka and Murton, 2008), which is a possible mechanism producing the gravel-sized fractions on Tron. Fig. 1.3 shows that fine to medium grained gabbro is mapped below 1200 m.a.s.l by Ramsey and Siedlecka (2001). The clasts are dominated of angular and subangular shapes and are probably a product of macrogelivation, while the few showing features of edge-rounding are probably exposed to granular disintegration, which tend to increase roundness (Benn, 2004). Both the clasts and the loess-sized fraction are mainly angular to subangular, which may indicate that they have been exposed to the same processes. According to Halleraker (2011) the present weathering on Tron are mainly chemical weathering, while frost weathering is only limited. The clasts originate presumably from in-situ weathering at a time where frost-related weathering occurred in higher rates than present.

Glacial abrasion, frost action and fluvio-glacial abrasion are recognized to be the dominant processes in formation of silt-sized particles in cold climates (Pye, 2015). The silt-sized particles on Tron are presumable not a product of in-situ glacial abrasion during the last glaciation. The glacier cover on Tron during Quaternary are assumed to be cold-based during Late Weichselian (Dahl et al., 1997), which is supported by Halleraker (2011) and Strømsøe and Paasche (2011), due to low modification of the underlying landforms. That does not exclude the possibility of an erosive warm-based glacier during earlier glaciations. Meltwater channels do occur on the southwest-west slopes of Tron (Thoresen and Follestad, 1999; Halleraker, 2011), which could potentially be a contributor to the occurrence of silt-sized particles on Tron by comminution of coarser fractions (Smith et al., 2002). Strømsøe and Paasche (2011) inferred that chemical weathering replaces the influence of physical weathering

in the comminution of particles smaller than 32 μm , which could be an important formation mechanism for the silt-sized fractions on Tron.

5.4 Further research

Samples from four horizons were collected for optically stimulated luminescence (OSL)-dating with the intention of obtaining information about the time of deposition of the sediments, but the process was not initiated due to economic reasons. An approach with a combination of OSL-dating and cosmogenic nuclide-dating could provide a mutual validation of the time of deposition.

6 Conclusion

In this thesis eight horizontal sections were extracted from two pits on the Tron summit blockfield. The aim shaping the thesis was to investigate if loess could be distinguished from in-situ weathered silt within these samples, through the application of the analysis modes provided from the scanning electron microscope based automated mineralogy.

The data showed that considerable amounts of fine-grained sediments are present in the excavated pits in the blockfield. The clast fractions are unevenly distributed within the columns. The compactness of the loess-sized fractions imply that the majority of the particles are bulky, in regard to the absence of particles assigned the value indicative of being circular. The mineral mapping-analysis provides compactness measurements indicative of a similar distribution between the depths of the column, while the Spot Centroid-analysis implied significant differences between the lowermost depth in TrP1, and the two lowermost depths in TrP2, compared to the upper sections of the columns. This trend is also observed for the compactness of quartz and plagioclase. It cannot be said with certainty which of the analyses provide the most precise measurements, but it seems that Spot Centroid overestimates the grain-sizes.

The mineralogy reflects in general the lithology and earlier geological mapping. The prominent outlier is the occurrence of quartz, which does not correlate with the bedrock geology on the summit. It was not possible to clarify if the quartz silt is a product of in-situ weathering in the lowermost parts of the mountain and has been vertically transported to the summit by freeze and thaw-processes, deposited in tills from subglacial transport, and/or origin from aeolian transport. If loess occurs on Tron, it probably is reasonable to see it in context with the dust deposition in Denmark, southern Sweden and the North Sea basin during Last Glacial Maximum (LGM).

The feret max diameter states that approximately 50% of quartz silt at each depth in TrP1 lies within the range of 20-60 μm according to Spot Centroid, while the mineral mapping-analysis provide a range of 43-51% within the same range characterizing loess deposits.

Both the gravel-sized clasts and the loess-sized fraction are characterized by being mostly angular to subangular, which may account for exposure to similar processes.

The analysis modes Spot Centroid and mineral mapping produce in general distinct differences in grain-size measurements and distribution of minerals. The mineral mapping is favorable in regard to its more detailed approach.

The grain morphology and mineralogy have similar features as loess deposits in China and eastern-Europe, but an occurrence could not be determined. Based on this study, this method itself are not sufficient to establish if loess particles are deposited on Tron, but could be a supportive analysis tool in correspondence with other methods.

7 List of references

- Allen, C. E., Darmody, R. G., Thorn, C. E., Dixon, J. C., & Schlyter, P. (2001). Clay mineralogy, chemical weathering and landscape evolution in Arctic–Alpine Sweden. *Geoderma*, 99(3-4), 277-294.
- Anand, R. R., & Paine, M. (2002). Regolith geology of the Yilgarn Craton, Western Australia: implications for exploration. *Australian Journal of Earth Sciences*, 49(1), 3-162.
- Andersen, K. K., Armengaud, A., & Genthon, C. (1998). Atmospheric dust under glacial and interglacial conditions. *Geophysical Research Letters*, 25(13), 2281-2284.
- Arocena, J. M., & Hall, K. (2004). Dark and light lichen coloration and basalt weathering in a cold environment: preliminary results from northern Canada. *Polar Geography*, 28(1), 32-42.
- Ballantyne, C. K. & Harris, C. 1994: *The periglaciation of Great Britain*. X, 330 s. Cambridge University Press, Cambridge.
- Ballantyne, C. K., McCarroll, D., Nesje, A., Dahl, S. O., & Stone, J. O. (1998). The last ice sheet in north-west Scotland: reconstruction and implications. *Quaternary Science Reviews*, 17(12), 1149-1184.
- Ballantyne, C. K. (2010). A general model of autochthonous blockfield evolution. *Permafrost and Periglacial Processes*, 21(4), 289-300.
- Ballantyne, C. K. (2018). *Periglacial geomorphology*. John Wiley & Sons.
- Benn, D. I., & Ballantyne, C. K. (1993). The description and representation of particle shape. *Earth Surface Processes and Landforms*, 18(7), 665-672.
- Benn, D. (2007). Clast Form Analysis. 2, 904-909.
- Berthling, I., & Sollid, J. L. (1999). The drainage history of glacial lake Nedre Glåmsjø, southern Central Norway. *Norsk Geografisk Tidsskrift-Norwegian Journal of Geography*, 53(4), 190-201.
- Bertran, P., Liard, M., Sitzia, L., & Tissoux, H. (2016). A map of Pleistocene aeolian deposits in Western Europe, with special emphasis on France. *Journal of Quaternary Science*, 31(8), 844-856.

- Blott, S. J., Croft, D. J., Pye, K., Saye, S. E., & Wilson, H. E. (2004). Particle size analysis by laser diffraction. *Geological Society, London, Special Publications*, 232(1), 63-73.
- Blott, S. J., & Pye, K. (2008). Particle shape: a review and new methods of characterization and classification. *Sedimentology*, 55(1), 31-63.
- Blott, S. J., & Pye, K. (2012). Particle size scales and classification of sediment types based on particle size distributions: Review and recommended procedures. *Sedimentology*, 59(7), 2071-2096.
- Boelhouwers, J. C. (1999). Relict periglacial slope deposits in the Hex River Mountains, South Africa: observations and palaeoenvironmental implications. *Geomorphology*, 30(3), 245-258.
- Boelhouwers, J. (2004). New perspectives on autochthonous blockfield development. *Polar Geography*, 28(2), 133-146.
- Boggs, S. (2011). *Principles of sedimentology and stratigraphy* (5th ed.). Boston: Prentice Hall.
- Boike, J., Roth, K., & Overduin, P. P. (1998). Thermal and hydrologic dynamics of the active layer at a continuous permafrost site (Taymyr Peninsula, Siberia). *Water Resources Research*, 34(3), 355-363.
- Bushell, C. (2012). The PGM flotation predictor: Predicting PGM ore flotation performance using results from automated mineralogy systems. *Minerals Engineering*, 36, 75-80.
- Dahl, S. O., Nesje, A., & Øvstedal, J. (1997). Cirque glaciers as morphological evidence for a thin Younger Dryas ice sheet in east-central southern Norway. *Boreas*, 26(3), 161-180.
- Darmody, R. G., Thorn, C. E., Seppälä, M., Campbell, S. W., Li, Y. K., & Harbor, J. (2008). Age and weathering status of granite tors in Arctic Finland (~68 N). *Geomorphology*, 94(1-2), 10-23.
- Dixon, J. C., & Thorn, C. E. (2005). Chemical weathering and landscape development in mid-latitude alpine environments. *Geomorphology*, 67(1-2), 127-145.
- Dixon, J. L., Heimsath, A. M., & Amundson, R. (2009). The critical role of climate and saprolite weathering in landscape evolution. *Earth Surface Processes and Landforms*, 34(11), 1507-1521.

- Engelien, E. (1995). Blokkmark og permafrost på Tron i Nord-Østerdal, Sør-Norge. *Cand. scient thesis*.
- Etzelmüller, B., & Frauenfelder, R. (2009). Factors controlling the distribution of mountain permafrost in the Northern Hemisphere and their influence on sediment transfer. *Arctic, Antarctic, and Alpine Research*, 41(1), 48-58.
- Farbrot, H., Hipp, T. F., Etzelmüller, B., Isaksen, K., Ødegård, R. S., Schuler, T. V., & Humlum, O. (2011). Air and ground temperature variations observed along elevation and continentality gradients in Southern Norway. *Permafrost and Periglacial Processes*, 22(4), 343-360.
- Faure, G. (1998). Principles and applications of geochemistry: A comprehensive textbook for geology students (2nd ed.). Upper Saddle River, N.J: Prentice Hall.
- Fjellanger, J., Sørbel, L., Linge, H., Brook, E. J., Raisbeck, G. M., & Yiou, F. (2006). Glacial survival of blockfields on the Varanger Peninsula, northern Norway. *Geomorphology*, 82(3-4), 255-272.
- Folk, R. L. (1980). *Petrology of sedimentary rocks*. Hemphill publishing company.
- Follestad, B. A. (1990). Block fields, ice-flow directions and the Pleistocene ice sheet in Nordmøre and Romsdal, West Norway. *Norsk geologisk tidsskrift*, 70, 27-33.
- French, H. (2007). *The periglacial environment* (3rd ed.). Chichester: Wiley.
- Fritz, S. (1988). A comparative study of gabbro and granite weathering. *Chemical Geology: Official Journal of the European Association for Geochemistry*, 68(3-4), 275-290
- Garnes, K., & Bergersen, O. F. (1980). Wastage features of the inland ice sheet in central South Norway. *Boreas*, 9(4), 251-269.
- Goehring, B. M., Brook, E. J., Linge, H., Raisbeck, G. M., & Yiou, F. (2008). Beryllium-10 exposure ages of erratic boulders in southern Norway and implications for the history of the Fennoscandian Ice Sheet. *Quaternary Science Reviews*, 27(3-4), 320-336.
- Gómez-Heras, M., Smith, B. J., & Fort, R. (2006). Surface temperature differences between minerals in crystalline rocks: Implications for granular disaggregation of granites through thermal fatigue. *Geomorphology*, 78(3-4), 236-249.

- Goodfellow, B. W. (2007). Relict non-glacial surfaces in formerly glaciated landscapes. *Earth-Science Reviews*, 80(1-2), 47-73.
- Goodfellow, B. W., Fredin, O., Derron, M. H., & Stroeven, A. P. (2009). Weathering processes and Quaternary origin of an alpine blockfield in Arctic Sweden. *Boreas*, 38(2), 379-398.
- Goodfellow, B. W. (2012). A granulometry and secondary mineral fingerprint of chemical weathering in periglacial landscapes and its application to blockfield origins. *Quaternary Science Reviews*, 57, 121-135.
- Goodfellow, B. W., Stroeven, A. P., Fabel, D., Fredin, O., Derron, M. H., Bintanja, R., & Caffee, M. W. (2014). Arctic-alpine blockfields in northern Sweden: Quaternary not Neogene. *Earth Surface Dynamics Discussions*, 2, 47-93.
- Gorbunov, A. P., Marchenko, S. S., & Seversky, E. V. (2004). The thermal environment of blocky materials in the mountains of Central Asia. *Permafrost and Periglacial Processes*, 15(1), 95-98.
- Graham, S. D., Brough, C., & Cropp, A. (2015). An introduction to Zeiss Mineralogic Mining and the correlation of light microscopy with automated mineralogy: a case study using BMS and PGM analysis of samples from a PGE-bearing chromitite prospect. *Precious Met*, 1-12.
- Graham, S. (2017, December). Automated Mineralogy: The Past, Present and Future. In *2017-Sustainable Industrial Processing Summit* (Vol. 4, pp. 96-115). Flogen Star Outreach.
- Gruber, S., & Haeberli, W. (2009). Mountain permafrost. In *Permafrost soils* (pp. 33-44). Springer, Berlin, Heidelberg.
- Haase, D., Fink, J., Haase, G., Ruske, R., Pécsi, M., Richter, H., ... & Jäger, K. D. (2007). Loess in Europe—its spatial distribution based on a European Loess Map, scale 1: 2,500,000. *Quaternary Science Reviews*, 26(9-10), 1301-1312.
- Haberlah, D., Strong, C., Pirrie, D., Rollinson, G. K., Gottlieb, P., Botha, P. P., & Butcher, A. R. (2011). Automated petrography applications in Quaternary Science. *Quaternary Australasia*, 28(2), 3.
- Hall, K., & Hall, A. (1996). Weathering by wetting and drying: some experimental results. *Earth Surface Processes and Landforms*, 21(4), 365-376.

- Hall, K. (1999). The role of thermal stress fatigue in the breakdown of rock in cold regions. *Geomorphology*, 31(1-4), 47-63.
- Halleraker, C. 2011: Kjemisk analyse av forvittringsmateriale fra et autoktont blokkhav og torformer, samt geomorfologisk kartlegging av Tron, Nord-Østerdalen i Hedmark, Sør-Norge. Masteroppgave. Institutt for geovitenskap, Universitetet i Bergen
- Harris, S. A., & Pedersen, D. E. (1998). Thermal regimes beneath coarse blocky materials. *Permafrost and periglacial processes*, 9(2), 107-120.
- Heggem, E. S., Juliussen, H., & Etzelmüller, B. (2005). Mountain permafrost in central-eastern Norway. *Norsk Geografisk Tidsskrift-Norwegian Journal of Geography*, 59(2), 94-108.
- Hinkel, K. M., Nelson, F. E., Shur, Y., Brown, J., & Everett, K. R. (1996). Temporal changes in moisture content of the active layer and near-surface permafrost at Barrow, Alaska, USA: 1962–1994. *Arctic and Alpine Research*, 28(3), 300-310.
- Hipp, T., Etzelmüller, B., Farbro, H., & Schuler, T. V. (2011). Modelling the temperature evolution of permafrost and seasonal frost in southern Norway during the 20th and 21st century. *The Cryosphere Discussions*, 5(2), 811-854.
- Hipp, T., Etzelmüller, B., Farbro, H., Schuler, T. V., & Westermann, S. (2012). Modelling borehole temperatures in Southern Norway—insights into permafrost dynamics during the 20th and 21st century. *The Cryosphere*, 6(3), 553-571.
- Hipp, T., & Universitetet i Oslo Det matematisk-naturvitenskapelige fakultet. (2012). Mountain Permafrost in Southern Norway: Distribution, Spatial Variability and Impacts of Climate Change, No. 1223.
- Hjulström, F., Sundborg, Å., & Falk, Å. (1955). Problems concerning the deposits of windblown silt in Sweden. *Geografiska Annaler*, 37(1-2), 86-117.
- Hopkinson, C., & Ballantyne, C. K. (2014). Age and origin of blockfields on Scottish mountains. *Scottish Geographical Journal*, 130(2), 116-141.
- Hughes, A. L., Gyllencreutz, R., Lohne, Ø. S., Mangerud, J., & Svendsen, J. I. (2016). The last Eurasian ice sheets—a chronological database and time-slice reconstruction, DATED-1. *Boreas*, 45(1), 1-45.

- Høgaas, F., & Longva, O. The early Holocene ice-dammed lake Nedre Glomsjø in Mid-Norway: an open lake system succeeding an actively retreating ice sheet. *NORWEGIAN JOURNAL OF GEOLOGY*, 98(4).
- Isaksen, K., Hauck, C., Gudevang, E., Ødegård, R. S., & Sollid, J. L. (2002). Mountain permafrost distribution in Dovrefjell and Jotunheimen, southern Norway, based on BTS and DC resistivity tomography data. *Norsk Geografisk Tidsskrift-Norwegian Journal of Geography*, 56(2), 122-136.
- Isaksen, K., Ødegård, R. S., Etzelmüller, B., Hilbich, C., Hauck, C., Farbrod, H., & Hipp, T. F. (2011). Degrading mountain permafrost in southern Norway: spatial and temporal variability of mean ground temperatures, 1999–2009. *Permafrost and Periglacial Processes*, 22(4), 361-377.
- Ishikawa, M. (2003). Thermal regimes at the snow–ground interface and their implications for permafrost investigation. *Geomorphology*, 52(1-2), 105-120.
- Juliussen, H., & Humlum, O. (2007). Towards a TTOP ground temperature model for mountainous terrain in central-eastern Norway. *Permafrost and Periglacial Processes*, 18(2), 161-184.
- Juliussen, H., & Humlum, O. (2008). Thermal regime of openwork block fields on the mountains Elgåhogna and Sølen, central-eastern Norway. *Permafrost and Periglacial Processes*, 19(1), 1-18.
- Keulen, N., Malkki, S. N., & Graham, S. (2020). Automated Quantitative Mineralogy Applied to Metamorphic Rocks. *Minerals*, 10(1), 47.
- Kottek, M., Grieser, J., Beck, C., Rudolf, B., & Rubel, F. (2006). World map of the Köppen-Geiger climate classification updated. *Meteorologische Zeitschrift*, 15(3), 259-263.
- Kleman, J. (1994). Preservation of landforms under ice sheets and ice caps. *Geomorphology*, 9(1), 19-32.
- Krumbein, W. C. (1941). The effects of abrasion on the size, shape and roundness of rock fragments. *The Journal of Geology*, 49(5), 482-520.
- Li, Y., Fabel, D., Stroeven, A. P., & Harbor, J. (2008). Unraveling complex exposure-burial histories of bedrock surfaces under ice sheets by integrating cosmogenic nuclide concentrations with climate proxy records. *Geomorphology*, 99(1-4), 139-149.

- Liu, Z., Liu, F., Ma, F., Wang, M., Bai, X., Zheng, Y., ... & Zhang, G. (2016). Collapsibility, composition, and microstructure of loess in China. *Canadian Geotechnical Journal*, 53(4), 673-686.
- Linge, H., Brook, E. J., Nesje, A., Raisbeck, G. M., Yiou, F., & Clark, H. (2006). In situ ¹⁰Be exposure ages from southeastern Norway: implications for the geometry of the Weichselian Scandinavian ice sheet. *Quaternary Science Reviews*, 25(9-10), 1097-1109.
- Mackay, J. R. (1984). The frost heave of stones in the active layer above permafrost with downward and upward freezing. *Arctic and Alpine Research*, 16(4), 439-446.
- Mahowald, N., Kohfeld, K., Hansson, M., Balkanski, Y., Harrison, S. P., Prentice, I. C., ... & Rodhe, H. (1999). Dust sources and deposition during the last glacial maximum and current climate: A comparison of model results with paleodata from ice cores and marine sediments. *Journal of Geophysical Research: Atmospheres*, 104(D13), 15895-15916.
- Mangerud, J. (2004). Ice sheet limits on Norway and the Norwegian continental shelf. *Quaternary glaciations—Extent and chronology*, 1, 271-294.
- Marr, P., & Löffler, J. (2017). Establishing a multi-proxy approach to alpine blockfield evolution in south-central Norway. *AUC Geographica*, 52(2), 219-236.
- Marr, P., Winkler, S., & Löffler, J. (2018). Investigations on blockfields and related landforms at Blåhø (Southern Norway) using Schmidt-hammer exposure-age dating: palaeoclimatic and morphodynamic implications. *Geografiska Annaler: Series A, Physical Geography*, 100(3), 285-306.
- Matsuoka, N. (2001). Microgelivation versus macrogelivation: towards bridging the gap between laboratory and field frost weathering. *Permafrost and Periglacial Processes*, 12(3), 299-313.
- Matsuoka, N. (2001b). Direct observation of frost wedging in alpine bedrock. *Earth Surface Processes and Landforms: The Journal of the British Geomorphological Research Group*, 26(6), 601-614.
- Matsuoka, N., & Murton, J. (2008). Frost weathering: recent advances and future directions. *Permafrost and Periglacial Processes*, 19(2), 195-210.

- Mitchell, J. K., & Soga, K. (2005). *Fundamentals of soil behavior* (Vol. 3). New York: John Wiley & Sons.
- Muhs, D. R. (2013). The geologic records of dust in the Quaternary. *Aeolian Research*, 9, 3-48.
- Munday, R. J. (1974). The geology of the northern half of the Lyngen Peninsula, Troms, Norway. *Norsk Geologisk Tidsskrift*, 54(suppl 1), 49-62.
- Murthy, V. N. S. (2002). *Geotechnical engineering: principles and practices of soil mechanics and foundation engineering*. CRC press.
- Murton, J. B., Coutard, J. P., Lautridou, J. P., Ozouf, J. C., Robinson, D. A., Williams, R. B., ... & Simmons, P. (2000). Experimental design for a pilot study on bedrock weathering near the permafrost table. *Earth Surface Processes and Landforms: The Journal of the British Geomorphological Research Group*, 25(12), 1281-1294.
- Murton, J. B., Peterson, R., & Ozouf, J. C. (2006). Bedrock fracture by ice segregation in cold regions. *Science*, 314(5802), 1127-1129.
- Murton, J., & Elias, Scott A. (2007). Periglacial landforms, rock forms; rock weathering. In *Encyclopedia of Quaternary science; Volume 3* (pp. 2249-2256). Amsterdam: Elsevier.
- Nesje, A., Dahl, S. O., Anda, E., & Rye, N. (1988). Block fields in southern Norway: Significance for the Late Weichselian ice sheet. *Norsk Geologisk Tidsskrift*, 68(3), 149-169.
- Nesje, A., McCarroll, D., & Dahl, S. O. (1994). Degree of rock surface weathering as an indicator of ice-sheet thickness along an east—west transect across southern Norway. *Journal of Quaternary Science*, 9(4), 337-347.
- NGU. (2020). Bedrock. Available from: http://geo.ngu.no/kart/losmasse_mobil/
- Olsen, L., Sveian, H., Bergstrøm, B., Ottesen, D., & Rise, L. (2013). Quaternary glaciations and their variations in Norway and on the Norwegian continental shelf. *Quaternary Geology of Norway*, 13, 27-78.
- Paasche, Ø., Strømsøe, J. R., Dahl, S. O., & Linge, H. (2006). Weathering characteristics of arctic islands in northern Norway. *Geomorphology*, 82(3-4), 430-452.

- Park, H., Fedorov, A. N., Zheleznyak, M. N., Konstantinov, P. Y., & Walsh, J. E. (2015). Effect of snow cover on pan-Arctic permafrost thermal regimes. *Climate Dynamics*, 44(9-10), 2873-2895.
- Paus, A., Velle, G., Larsen, J., Nesje, A., & Lie, Ø. (2006). Lateglacial nunataks in central Scandinavia: Biostratigraphical evidence for ice thickness from Lake Flåfattjønn, Tynset, Norway. *Quaternary Science Reviews*, 25(11-12), 1228-1246.
- Pavelić, D., Kovačić, M., Banak, A., Jiménez-Moreno, G., Marković, F., Pikelj, K., ... & Belak, M. (2016). Early Miocene European loess: A new record of aridity in southern Europe. *Bulletin*, 128(1-2), 110-121.
- Phillips, W. M., Hall, A. M., Mottram, R., Fifield, L. K., & Sugden, D. E. (2006). Cosmogenic ¹⁰Be and ²⁶Al exposure ages of tors and erratics, Cairngorm Mountains, Scotland: timescales for the development of a classic landscape of selective linear glacial erosion. *Geomorphology*, 73(3-4), 222-245.
- Pirrie, D., & Rollinson, G. K. (2011). Unlocking the applications of automated mineral analysis. *Geology Today*, 27(6), 226-235.
- Powers, M. C. (1953). A new roundness scale for sedimentary particles. *Journal of Sedimentary Research*, 23(2), 117-119.
- Pye, K. (1984). Loess. *Progress in Physical Geography*, 8(2), 176-217.
- Pye, K. (1995). The nature, origin and accumulation of loess. *Quaternary Science Reviews*, 14(7-8), 653-667.
- Pye, K. (2015). *Aeolian dust and dust deposits*. Elsevier.
- Ramsey, D. & Siedlecka, A. 2001: Berggrunnskart ALVDAL 1619 III, M 1:50 000, foreløpig utgave. *Norges geologiske undersøkelse*.
- Rea, B. R., Whalley, W. B., Rainey, M. M., & Gordon, J. E. (1996). Blockfields, old or new? Evidence and implications from some plateaus in northern Norway. *Geomorphology*, 15(2), 109-121.
- Roaldset, E., Pettersen, E., Longva, O., & Mangerud, J. (1982). Remnants of preglacial weathering in western Norway. *Norsk Geologisk Tidsskrift*, 62(3), 169-178.
- Rollinson, G. (2019). Automated Mineralogy by SEM-EDS.

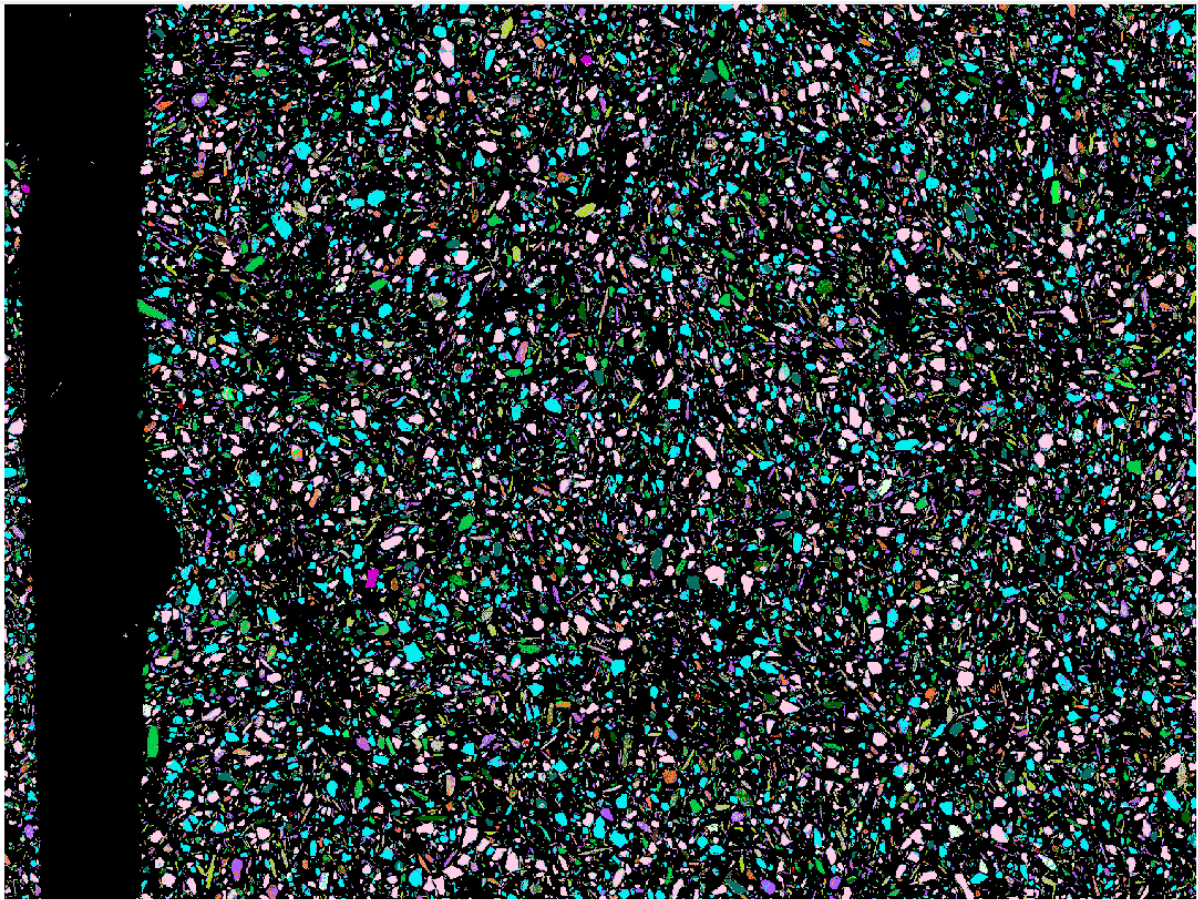
- Røisi, I., & Aasly, K. (2018). The effect of graphite filler in sample preparation for automated mineralogy—a preliminary study.
- Schaffernicht, E. J., Ludwig, P., & Shao, Y. (2020). Linkage between dust cycle and loess of the Last Glacial Maximum in Europe. *Atmospheric Chemistry & Physics*, 20(8).
- SeNorge. (2020). Available from: <http://www.senorge.no/>
- Smith, B. J., Wright, J. S., & Whalley, W. B. (2002). Sources of non-glacial, loess-size quartz silt and the origins of “desert loess”. *Earth-Science Reviews*, 59(1-4), 1-26.
- Sprafke, T., & Obrecht, I. (2016). Loess: rock, sediment or soil—what is missing for its definition?. *Quaternary International*, 399, 198-207.
- Statens Kartverk. (2020). Available from: <https://norgeskart.no/>
- Strandberg, G., Brandefelt, J., Kjellström, E., & Smith, B. (2011). High-resolution regional simulation of last glacial maximum climate in Europe. *Tellus A: Dynamic Meteorology and Oceanography*, 63(1), 107-125.
- Stroeven, A. P., Fabel, D., Hättestrand, C., & Harbor, J. (2002). A relict landscape in the centre of Fennoscandian glaciation: cosmogenic radionuclide evidence of tors preserved through multiple glacial cycles. *Geomorphology*, 44(1-2), 145-154.
- Strømsøe, J. R., & Paasche, Ø. (2011). Weathering patterns in high-latitude regolith. *Journal of Geophysical Research: Earth Surface*, 116(F3).
- Sugden, D. E., Balco, G., Cowdery, S. G., Stone, J. O., & Sass III, L. C. (2005). Selective glacial erosion and weathering zones in the coastal mountains of Marie Byrd Land, Antarctica. *Geomorphology*, 67(3-4), 317-334.
- Taylor, A., Nixon, M., Eley, J., Burgess, M., & Egginton, P. (1998, June). Effect of atmospheric temperature inversions on ground surface temperatures and discontinuous permafrost, Norman Wells, Mackenzie Valley, Canada. In *Proceedings of the Seventh International Conference on Permafrost, Yellowknife, NWT, Université Laval, Quebec, Collection Nordicana* (No. 57, pp. 1043-1048).
- Thoresen, M. & Follestad, B.A.. ALVDAL Kommune, Kwartærgeologisk kart i M 1:60 000. Norges geologiske undersøkelse 1999.

- Thorn, C. E., Darmody, R. G., Dixon, J. C., & Schlyter, P. (2001). The chemical weathering regime of Kärkevagge, arctic–alpine Sweden. *Geomorphology*, *41*(1), 37-52.
- Újvári, G., Kovács, J., Varga, G., Raucsik, B., & Marković, S. B. (2010). Dust flux estimates for the Last Glacial Period in East Central Europe based on terrestrial records of loess deposits: a review. *Quaternary Science Reviews*, *29*(23-24), 3157-3166.
- Újvári, G., Stevens, T., Molnár, M., Demény, A., Lambert, F., Varga, G., ... & Kovács, J. (2017). Coupled European and Greenland last glacial dust activity driven by North Atlantic climate. *Proceedings of the National Academy of Sciences*, *114*(50), E10632-E10638.
- Westermann, S., Schuler, T., Gislås, K., & Etzelmüller, B. (2013). Transient thermal modeling of permafrost conditions in Southern Norway. *The Cryosphere*, *7*(2), 719-739.
- Wellings, S. (1996). Geology of the Tronfjell massif: placing mafic magmatism into a tectono-stratigraphic framework.
- Wellings SA, Sturt BA. (1998). Tectonic setting of the Tronfjell Massif; further evidence for pre-Scandian orogenesis in the Trondheim Nappe Complex, Central Norway. *Norges Geologiske Undersøkelse Bulletin* 434, 109–115.
- West, A. J., Galy, A., & Bickle, M. (2005). Tectonic and climatic controls on silicate weathering. *Earth and Planetary Science Letters*, *235*(1-2), 211-228.
- Whalley, W. B., Rea, B. R., & Rainey, M. M. (2004). Weathering, blockfields, and fracture systems and the implications for long-term landscape formation: some evidence from Lyngen and Øksfordjøkelen areas in north Norway. *Polar Geography*, *28*(2), 93-119.
- White, A. F., & Brantley, S. L. (1995). Weathering rates of silicate minerals. *Chemical Weathering Rates of Silicate Minerals, Reviews in Mineralogy*, *31*, 1-22.
- Williams, P., & Smith, M. (1989). *The frozen earth: Fundamentals of geocryology (Studies in polar research)*. Cambridge: Cambridge University Press.
- Wright, J., Smith, B., & Whalley, B. (1998). Mechanisms of loess-sized quartz silt production and their relative effectiveness: laboratory simulations. *Geomorphology*, *23*(1), 15-34.
- Zeiss. (2020). Available from: <https://www.zeiss.com/microscopy/int/products/scanning-electron-microscopes/sigma.html>

Zhang, T., Barry, R. G., Knowles, K., Heginbottom, J. A., & Brown, J. (2008). Statistics and characteristics of permafrost and ground-ice distribution in the Northern Hemisphere. *Polar Geography*, 31(1-2), 47-68.

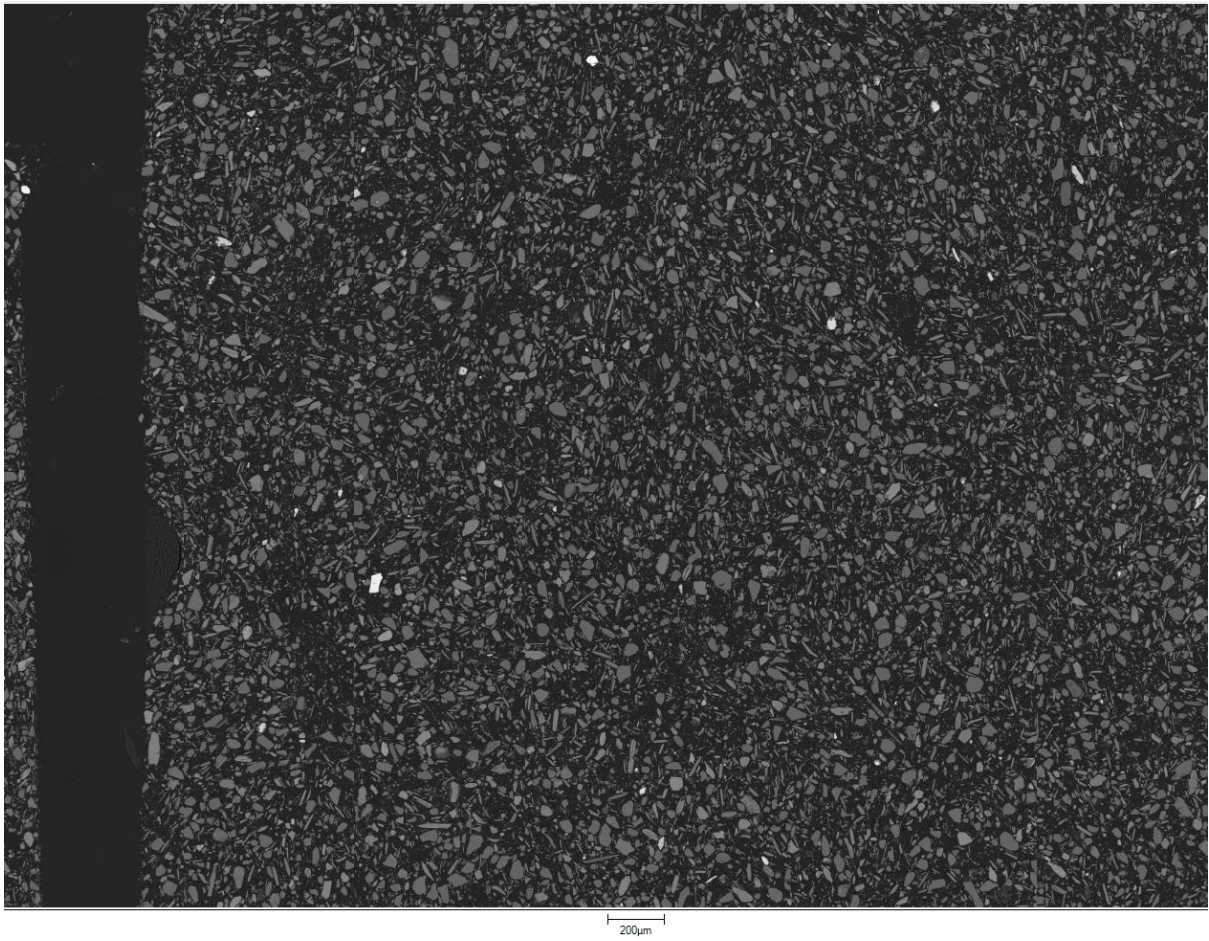
8 Appendix

S1: False-color image

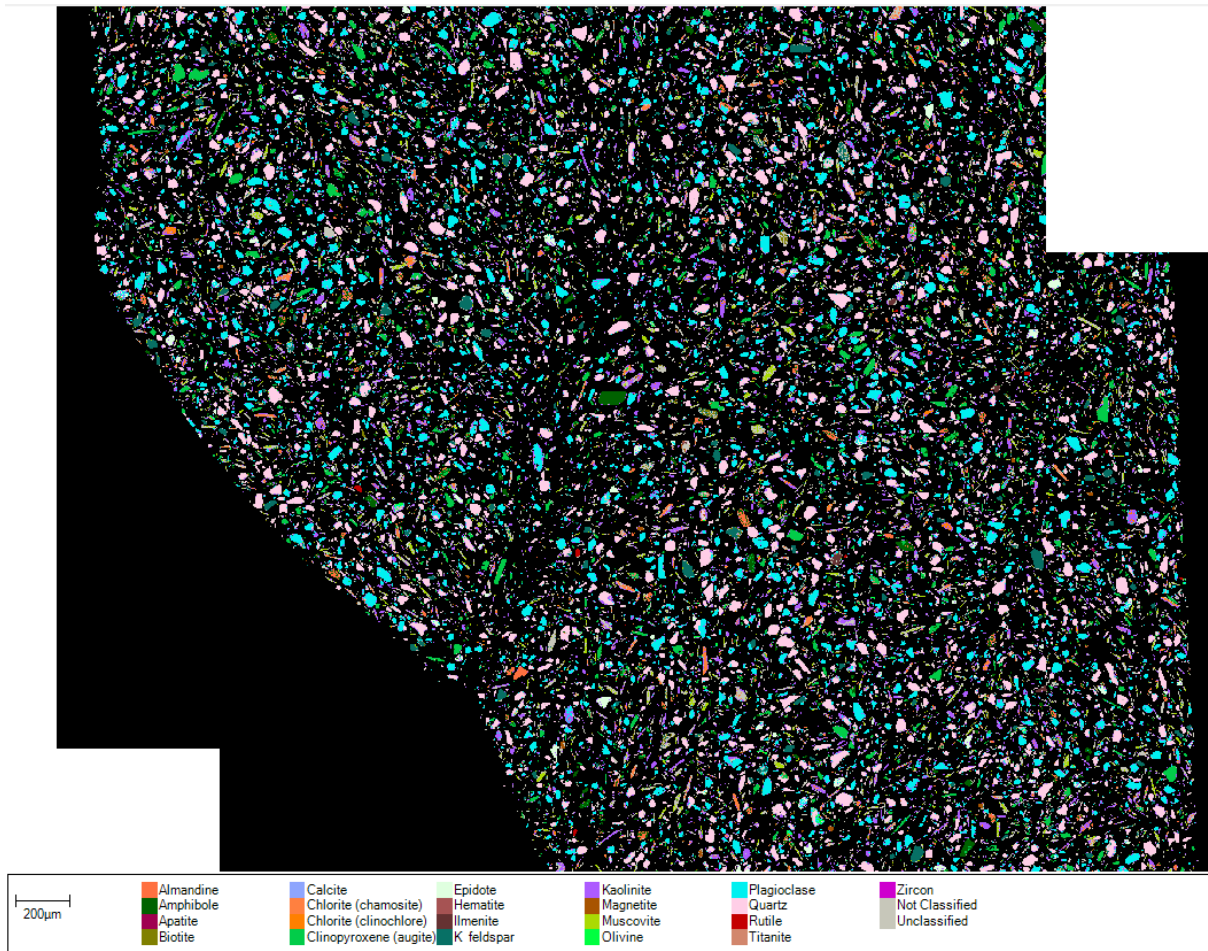


- | | | | | | | | |
|-----------|---------|------------------------|------------|-----------|-------------|----------|--------------------------------|
| Almandine | Biotite | Chlorite (clinocllore) | Hematite | Kaolinite | Olivine | Rutile | Not Classified
Unclassified |
| Amphibole | Calcite | Chlorite (chamosite) | Ilmenite | Magnetite | Plagioclase | Titanite | |
| Apatite | | Epidote | K feldspar | Muscovite | Quartz | Zircon | |

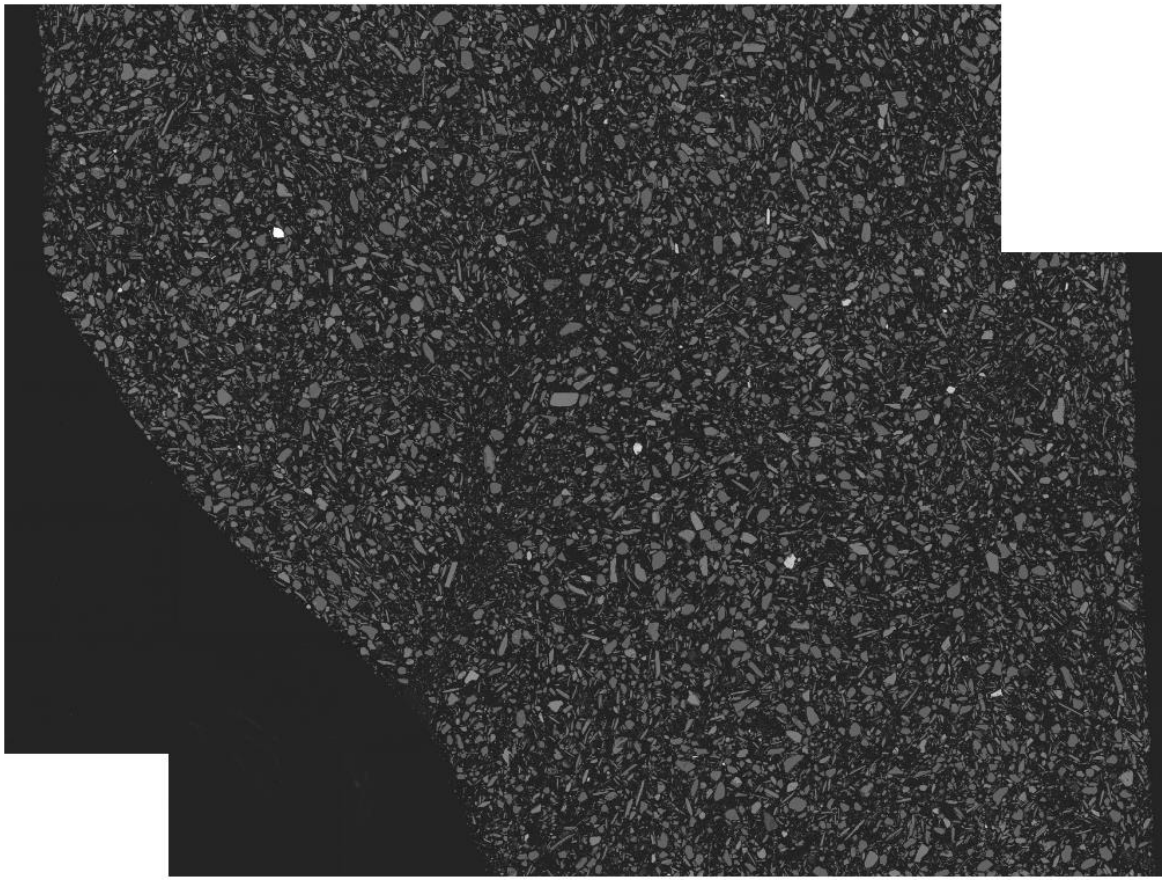
S1: Backscattered-electron image



S2: False-color image

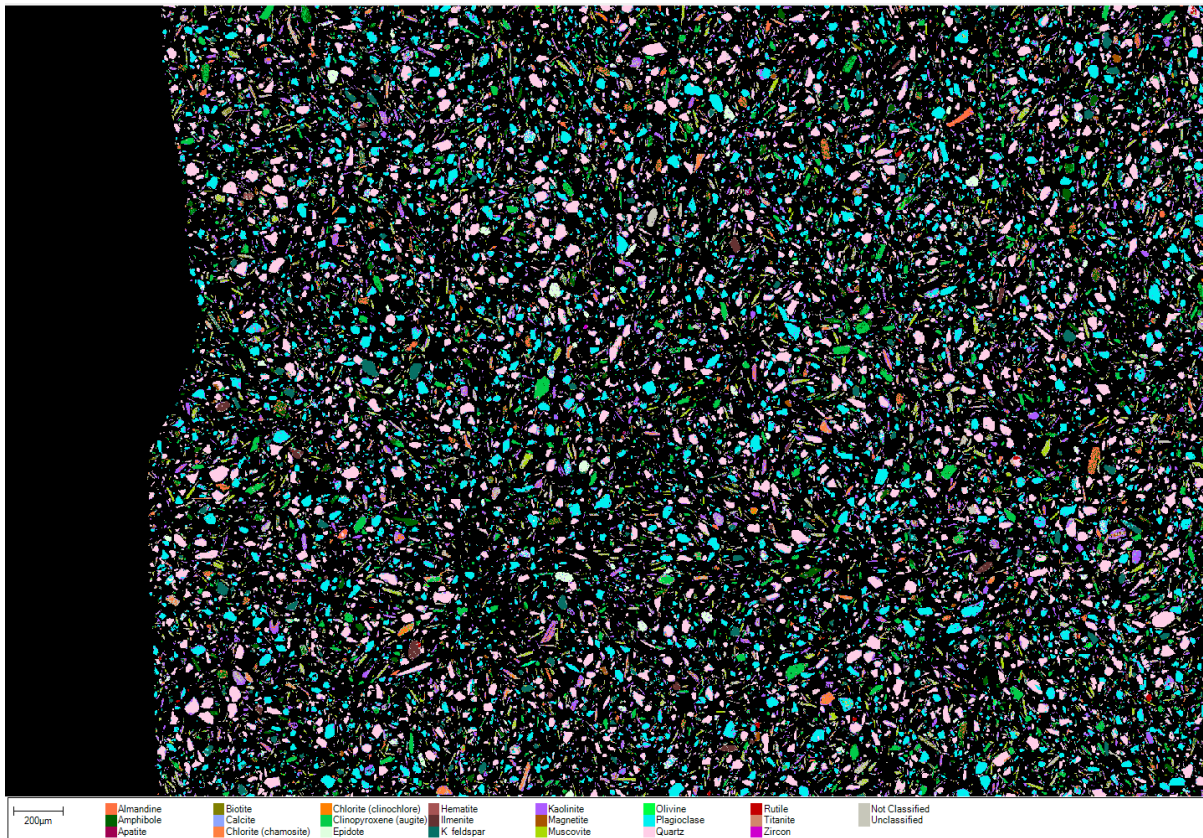


S2: Backscattered-electron image

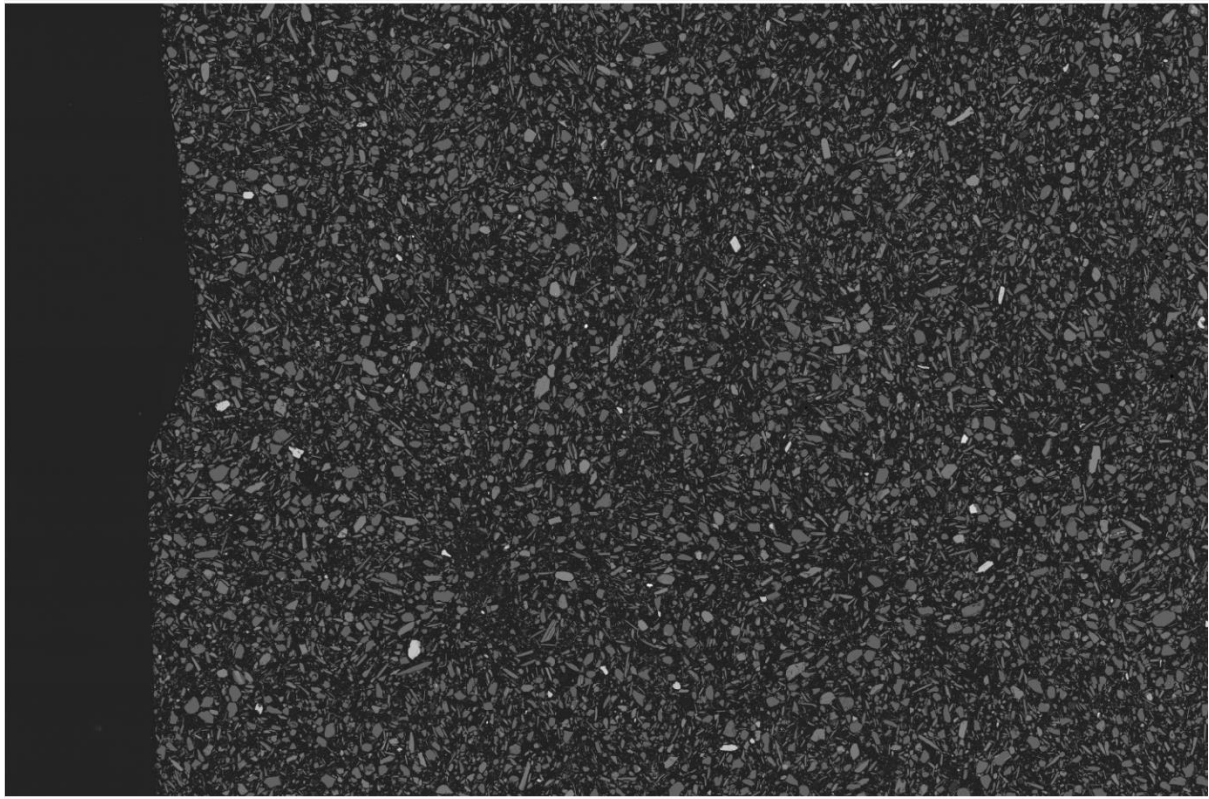


200µm

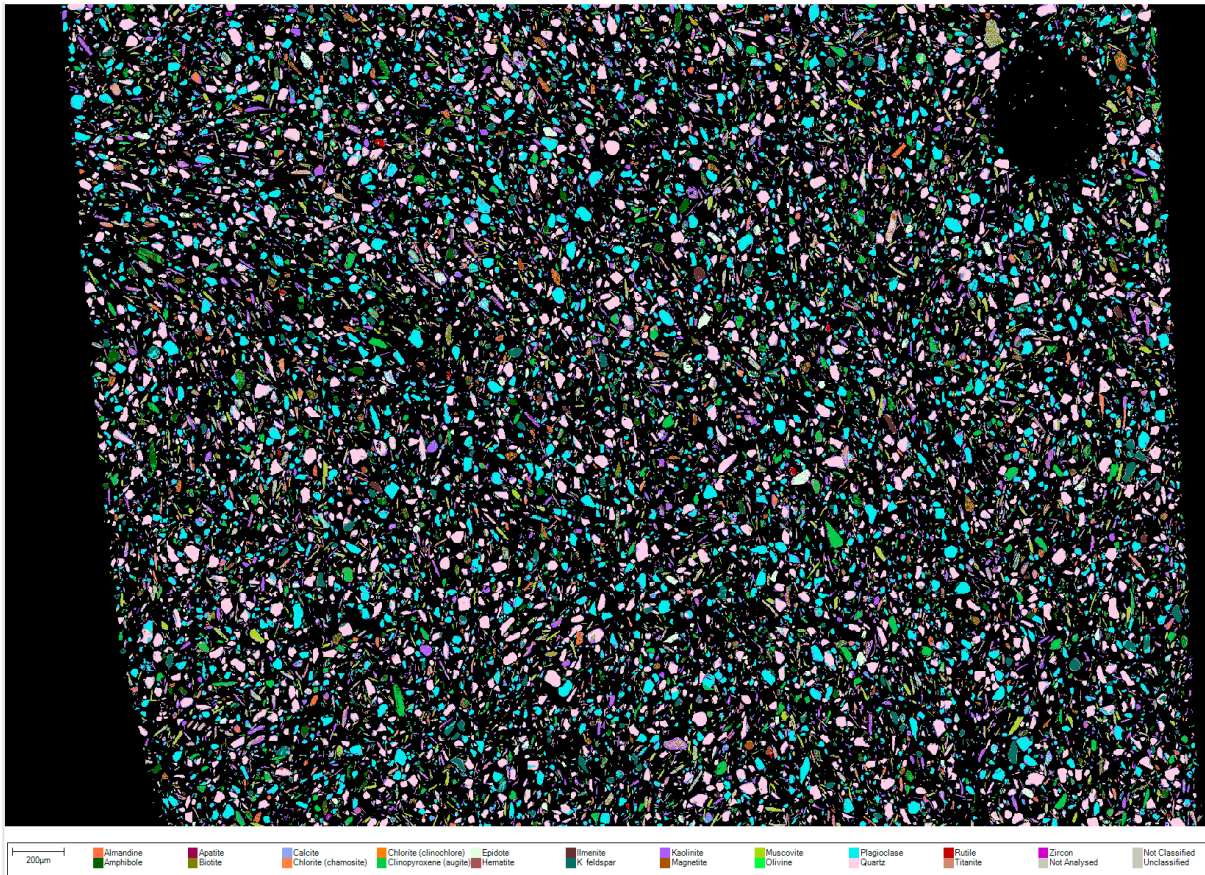
S3: False-color image



S3: Backscattered-electron image



S4: False-color image



S4: Backscattered-electron image

